MINISTRY OF NATIONAL EDUCATION

THE ANNALS OF "DUNAREA DE JOS" UNIVERSITY OF GALATI

Fascicle IX
METALLURGY AND MATERIALS SCIENCE

YEAR XXXIII (XXXVIII)
June 2015, no. 2

ISSN 1453-083X

2015
GALATI UNIVERSITY PRESS

EDITORIAL BOARD

THE ANNALS OF "DUNAREA DE JOS" UNIVERSITY OF GALATI
FASCICLE IX. METALLURGY AND MATERIALS SCIENCE
Nº. 2 - 2015, ISSN 1453 – 083X

Table of Content

THE ANNALS OF "DUNAREA DE JOS" UNIVERSITY OF GALATI
FASCICLE IX. METALLURGY AND MATERIALS SCIENCE
Nº. 2 - 2015, ISSN 1453 – 083X

EFFECTIVE ELECTROMECHANICAL COUPLING FOR THE PARTIALLY ELECTRODED CERAMIC RESONATORS OF DIFFERENT GEOMETRIES

Jiří Erhart* and Tutu Sebastian
Department of Physics and Piezoelectricity Research Laboratory, Technical University of Liberec, Studentská 2, 461 17 Liberec 1, Czech Republic
*corresponding author
e-mail: jiri.erhart@tul.cz

ABSTRACT

Effective electromechanical coupling factor (ECF) was studied on bar, disc and ring ceramic resonators partially covered by electrodes. ECFs were calculated theoretically and verified experimentally. Bar resonators (k_{31}-mode) show maximum value of ECF k_{eff} = 0.26 at the electrode aspect ratio equal to 0.75 with calculated values fitting the experimental data for all aspect ratios. Calculations for bar resonators with embedded electrodes (k_{33}-mode) show similar behavior like for k_{31}-mode, but at higher ECFs. Maximum value of ECF for such a mode reaches k_{eff} = 0.67 for the electrode aspect ratio of 0.75. Partially electroded disc resonators (k_p-mode) are well described analytically by one-dimensional model only for the electrode aspect ratios up to 0.5. Maximum value k_{eff} = 0.58 for disc resonators was measured at the electrode aspect ratio equal to 0.80. Partially electroded ring resonators (k_p-mode) show the same trend as discs without saturation of ECF values. Maximum ECF k_{eff} = 0.34 was measured for ring resonators with full electrode. The presented analytical formulae may serve as a guide for the optimum electrode pattern design for the partially electroded resonators.

KEYWORDS: piezoelectric ceramics, PZT, resonator, vibration modes, electromechanical coupling factor

1. Introduction

Electromechanical coupling factor (ECF) describes the energy transfer between its mechanical and electrical form. Static electromechanical coupling might be different from the dynamic coupling factor specific for certain vibration modes [1]. ECF links together "free" and "clamped" material properties for different resonators shapes. ECFs for different vibration modes are also cross-linked by various relations [2].

ECFs are practically measured using the analysis of impedance spectrum in terms of resonance (f_r) and antiresonance (f_a) frequencies [1, 3] with an effective dynamic coupling factor

$$k_{eff}^2 = \frac{f_a^2 - f_r^2}{f_a^2} \qquad (1)$$

This formula is universal for any vibration mode of resonators, but there are also specific formulae for the different vibration modes of resonators (e.g. k_{31}, k_{33}, k_p, k_t, k_{15} modes) in the shape of bar, thin disc or plate [3]. Resonators for ECF measurement are designed as fully electroded piezoelectric ceramic bodies. Such resonators are not necessarily optimized with respect to ECF value.

It is basically anticipated that the piezoelectric resonator with full electrode has its maximum electromechanical coupling. However, sometimes it is not possible to deposit the full electrode on the piezoelectric resonator faces because of the mechanical clamping or electrical insulation of the resonator. Small facet at the piezoelectric ceramic ring or disc edges is one of the examples of such electrode deposition deficiency. There is also the possibility of ECF enhancement by the electrode pattern optimization.

The experimental visualization of modal shapes was published for fully electroded ceramic disc

resonators for the radial and flexural vibration modes and verified by laser holography [4]. A similar visualization was also performed by the same technique on the partially electroded discs in two geometries [5] – disc with central circular electrode or with annular electrode arrangement. The optimum electromechanical coupling k = 0.605 for the disc planar mode was theoretically calculated for the electrode size ratio r_0 = 0.83a for PIC-151 PZT ceramics (r_0, a are the radii of electrode and disc).

Theoretical calculations on partially electroded disc ceramic resonators were published by Ivina [6]. A ceramic disc was partially electroded inside the central circular area or at the outer annular electrode. The optimum ECF k = 0.51 was calculated for the central circular electrode size ratio r_0 = 0.9a for TsTBS-3 PZT type. The enhancement of ECF for the partially electroded disc (k = 0.51) with respect to the fully electroded one (k = 0.50) was calculated. The ceramic resonator operates more efficiently with optimum electrode size than with the full electrode.

Other theoretical calculations on the partially covered ceramic resonators were published by Rogacheva [7]. She calculated ECFs for several electrode geometries – disc plate with central circular or ring electrode and cylindrical ceramic shell with fully or partially electroded circumference. All numerical data were presented for PZT-5 piezoelectric ceramics under "free" and "clamped" mechanical conditions. ECF reaches maximum k = 0.55 for the electrode size of r_0 = 0.85a for central circular electrode arrangement and k = 0.413 for ring electrode covering the radii range $0.6a \le r_0 \le 0.9a$. The maximum ECF calculated for the cylindrical ceramic shell was k = 0.57 for the electrode covering the shell length L_0 = 0.7L (for the shell aspect ratio 2L = 2a, where L and a are the shell's total length and radius). The enhancement of ECF for the partially electroded resonator with respect to the full electrode was also predicted.

The present paper addresses the issues of partially electroded and longitudinally vibrating bar, radially vibrating disc with central circular electrode and radially vibrating ring resonator with partial annular electrode. ECFs are theoretically calculated and experimentally verified by the resonance / antiresonance frequency measurement [3]. This work confirms experimentally previously published theoretical results on the partially electroded disc resonators. ECFs for bar and ring resonators with partial electrodes are theoretically calculated and experimentally measured. The optimum electrode size and the corresponding ECFs were found. The choice of bar and ring resonators with partial electrodes was motivated by the use of such structures in piezoelectric ceramic transformers design – e.g. ring transformer with axisymmetrically divided electrodes or bar transformer with symmetrical or asymmetrical electrode pattern. Ceramic resonators in the shape of ring made from hard PZTs are also typically used for the ultrasound generation in ultrasonic welding and cleaning technology – e.g. in Langevin transducer design. Partially electroded bar and ring resonators were not reported previously, neither theoretically, nor experimentally. One type of soft PZT (APC850) and one type of hard PZT (APC841) was selected for experiments in order not to limit our results only for one specific PZT type.

2. Theoretical considerations

For the calculation of the resonator's electrical impedance/admittance, we adopted one-dimensional vibration modes for thin bar, thin disc and thin ring. Equation of motion:

$$T_{ij,j} = \rho \ddot{u}_i, \quad i = 1,2,3 \tag{2}$$

and Maxwell's equation for non-conducting medium:

$$D_{i,i} = 0, \tag{3}$$

will be solved for the piezoelectric ceramics medium. Piezoelectric equations of state:

$$S_\alpha = s^E_{\alpha\beta} T_\beta + d_{i\alpha} E_i \tag{4}$$

$$D_i = d_{i\alpha} T_\alpha + \varepsilon^T_{ij} E_j \tag{5}$$

are defined by the crystallographic symmetry of ceramics material. The electrode's material and its thickness are not taken into account. The elastic strain tensor is defined by the derivatives of displacement components:

$$S_{ij} = \frac{1}{2}\left(u_{i,j} + u_{j,i}\right) \tag{6}$$

and the electric field by the electric potential derivative:

$$E_i = -\Phi_{,i} \tag{7}$$

The electrical impedance of the resonator is calculated from the displacement current:

$$I = \frac{\partial}{\partial t}\left(\int_{(S)} D_3 dS \right) \tag{8}$$

where the electric displacement is integrated over the electrode surface. The electrical admittance is a ratio of the displacement current and the input voltage:

$$Y = -\frac{I}{Ue^{j\omega t}} \tag{9}$$

2.1. Partially electroded thin bar – transverse longitudinal mode

Mechanical stress/strain system for the thickness-poled and longitudinally vibrating thin bar is given by only one non-zero stress component ($T_1 \neq 0$) and one electrical field/displacement ($E_3 \neq 0$, $D_3 \neq 0$) – for coordinate system see Fig. 1.

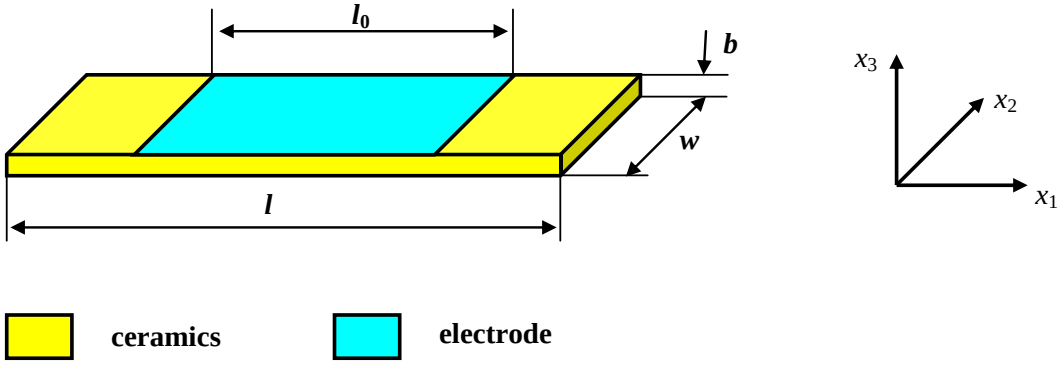

Fig. 1. *Partially electroded bar resonator – thickness poled*

Boundary conditions include mechanically free ends of bar (i.e. $T_1 = 0$) and the continuity of mechanical stress / displacement at the electrode edges. After the calculations described above, we can derive the formula for the electrical admittance:

$$Y = j\omega\left(\varepsilon_{33}^{T}\frac{wl_0}{b}\right)\left\{1-k_{31}^2+k_{31}^2\frac{\sin(\frac{l_0}{l}\eta)\cos((1-\frac{l_0}{l})\eta)}{\frac{l_0}{l}\eta\cos(\eta)}\right\} \tag{10}$$

where

$$\eta = \frac{1}{2}kl, k = 2\pi f\sqrt{\rho s_{11}^E}$$

In a limiting case of the fully electroded resonator (i.e. $l_0 \rightarrow l$), the formula is reduced to the admittance of bar resonator [3].

$$Y = j\omega\left(\varepsilon_{33}^{T}\frac{wl}{b}\right)\left\{1-k_{31}^2+k_{31}^2\frac{\tan(\eta)}{\eta}\right\} \tag{11}$$

The resonance condition for the partially electroded resonator is the same as for the fully electroded one:

$$\eta_r = \frac{\pi}{2}, \frac{3\pi}{2}, \frac{5\pi}{2}, \ldots \tag{12}$$

but the antiresonance condition includes the dimension of the electroded resonator's part in a transcendental equation:

$$1-k_{31}^2+k_{31}^2\frac{\sin(\frac{l_0}{l}\eta_a)\cos((1-\frac{l_0}{l})\eta_a)}{\frac{l_0}{l}\eta_a\cos(\eta_a)} = 0 \tag{13}$$

2.2. Thin bar with embedded electrodes – longitudinal mode

Mechanical stress / strain system for the longitudinally-poled and longitudinally vibrating thin bar is given by only one non-zero stress component ($T_3 \neq 0$) and one electrical field / displacement ($E_3 \neq 0, D_3 \neq 0$) – for coordinate system, see Fig. 2.

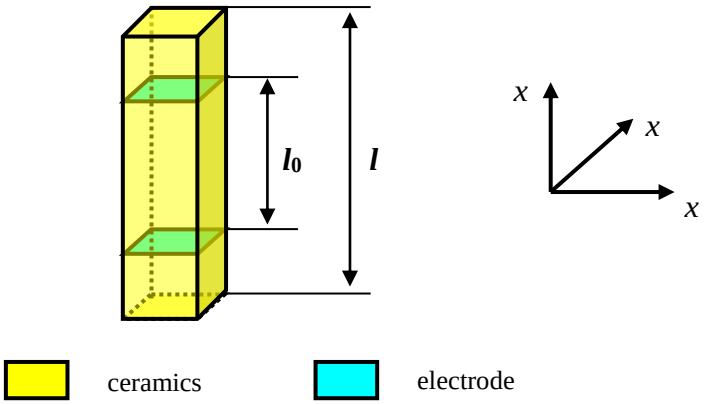

Fig. 2. *Bar resonator with embedded electrodes – longitudinally poled*

Boundary conditions include mechanically free ends of bar (i.e. $T_3 = 0$) and the continuity of mechanical stress / displacement at the electrode edges. After the calculations described above, we can derive the formula for the electrical impedance:

$$Z = \frac{1}{j\omega\left(\varepsilon_{33}^{T}\frac{S}{l_0}\right)\left(1-k_{33}^2\right)}\left\{1-k_{33}^2\frac{\sin(\frac{l_0}{l}\eta)\cos((1-\frac{l_0}{l})\eta)}{\frac{l_0}{l}\eta\cos(\eta)}\right\} \quad (14)$$

where $\eta = \frac{1}{2}kl, k = 2\pi f\sqrt{\rho s_{33}^D}$ and S is the electrode area. In a limiting case of the fully electroded resonator (i.e. $l_0 \to l$), the formula is reduced to the impedance of bar resonator [3].

$$Z = \frac{1}{j\omega\left(\varepsilon_{33}^{T}\frac{S}{l_0}\right)\left(1-k_{33}^2\right)}\left\{1-k_{33}^2\frac{\tan(\eta)}{\eta}\right\} \quad (15)$$

The antiresonance condition is the same as for the fully electroded resonator

$$\eta_a = \frac{\pi}{2}, \frac{3\pi}{2}, \frac{5\pi}{2}, \ldots \quad (16)$$

but the resonance condition depends on the dimension of the electroded part

$$1-k_{33}^2\frac{\sin(\frac{l_0}{l}\eta_r)\cos((1-\frac{l_0}{l})\eta_r)}{\frac{l_0}{l}\eta_r\cos(\eta_r)} = 0 \quad (17)$$

2.3. Partially electroded thin disc – planar mode

Mechanical stress / strain system for the thickness-poled and radially vibrating thin disc is given by non-zero radial and thickness displacement components ($u_r \neq 0, u_z \neq 0$) and one electric field / displacement component ($E_3 \neq 0, D_3 \neq 0$) – for coordinate system, see Fig. 3.

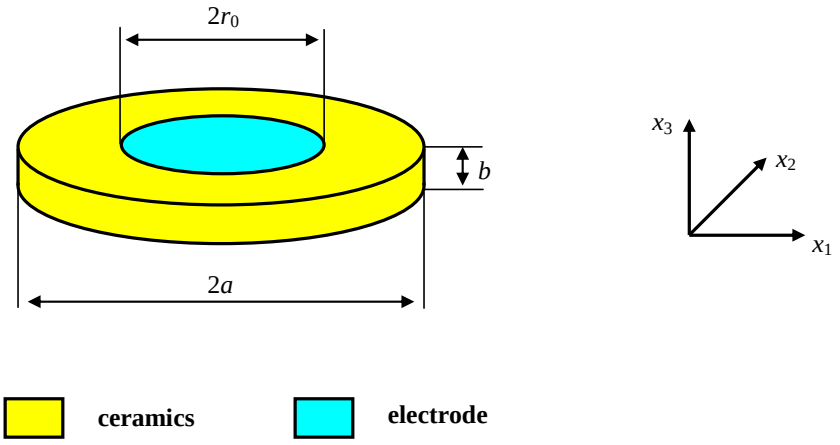

Fig. 3. *Partially electroded disc resonator – thickness poled*

Boundary conditions include mechanically free outer disc circumference (i.e. $T_r = 0$) and the continuity of mechanical stress / displacement at the electrode edges. We use the calculation method published in [8] for homogeneously poled thin ceramic discs. The resonator's admittance could be calculated as:

$$Y = j\omega\left(\varepsilon_{33}^{P}\frac{\pi r_0^2}{b}\right)\left\{1+\frac{k_p^2(1+\sigma^E)}{1-k_p^2}\frac{J_0(\frac{r_0}{a}\eta)}{K_1(\eta)}\frac{K_1(\eta)Y_1(\frac{r_0}{a}\eta)-K_2(\eta)J_1(\frac{r_0}{a}\eta)}{K_1(\frac{r_0}{a}\eta)Y_1(\frac{r_0}{a}\eta)-K_2(\frac{r_0}{a}\eta)J_1(\frac{r_0}{a}\eta)}\right\} \quad (18)$$

where $K_1(\eta) = J_0(\eta)\eta - (1-\sigma^E)J_1(\eta)$;
$K_2(\eta) = Y_0(\eta)\eta - (1-\sigma^E)Y_1(\eta)$;
$\eta = 2\pi f a\sqrt{\rho/c_{11}^P}$; σ^E is Poisson's ratio, $\varepsilon_{33}^P = \varepsilon_{33}^S + \frac{e_{33}^2}{c_{33}^E}$; $c_{11}^P = c_{11}^E - \frac{\left(c_{13}^E\right)^2}{c_{33}^E}$; k_p is planar electromechanical coupling factor and J_0, J_1; Y_0, Y_1 are zero- and first-order Bessel's functions of the first and second kind. In a limiting case of the fully electroded disc (i.e. $r_0 \to a$), admittance is reduced to the known formula for disc resonator [3]:

$$Y = j\omega\left(\varepsilon_{33}^{P}\frac{\pi a^2}{b}\right)\left\{1+\frac{k_p^2(1+\sigma^E)}{1-k_p^2}\frac{J_0(\eta)}{K_1(\eta)}\right\} \quad (19)$$

The resonance condition for the homogeneous disc resonator is identical with the zero value for the denominator in Eq. (18).

$$K_1(\eta_r)\left[K_1(\frac{r_0}{a}\eta_r)Y_1(\frac{r_0}{a}\eta_r)-K_2(\frac{r_0}{a}\eta_r)J_1(\frac{r_0}{a}\eta_r)\right]=0 \quad (20)$$

The antiresonance condition is:

$$1+\frac{k_p^2(1+\sigma^E)}{1-k_p^2}\frac{J_0(\frac{r_0}{a}\eta_a)}{K_1(\eta_a)}\frac{K_1(\eta_a)Y_1(\frac{r_0}{a}\eta_a)-K_2(\eta_a)J_1(\frac{r_0}{a}\eta_a)}{K_1(\frac{r_0}{a}\eta_a)Y_1(\frac{r_0}{a}\eta_a)-K_2(\frac{r_0}{a}\eta_a)J_1(\frac{r_0}{a}\eta_a)}=0 \tag{21}$$

2.4. Partially electroded thin ring – planar mode

A similar calculation method like the one used for thin disc, stress / strain system and boundary conditions (including the free ring's inner diameter circumference) was also adopted for thin partially electroded ring vibrating radially - for geometry, see Fig. 4.

The admittance of such a resonator is ($\eta = 2\pi f a_2\sqrt{\rho/c_{11}^P}$).

$$Y = j\omega\left(\varepsilon_{33}^P\frac{\pi(r_2^2-r_1^2)}{b}\right)\left\{1-\frac{k_p^2(1+\sigma^E)}{1-k_p^2}\times\right.$$

$$\times\left[\frac{K_2(\eta)K_2(\frac{a_1}{a_2}\eta)\left(\frac{r_2}{a_2}\eta J_1(\frac{r_2}{a_2}\eta)-\frac{r_1}{a_2}\eta J_1(\frac{r_1}{a_2}\eta)\right)}{\eta^2(\frac{r_2^2}{a_2^2}-\frac{r_1^2}{a_2^2})\left[K_1(\frac{a_1}{a_2}\eta)K_2(\eta)-K_1(\eta)K_2(\frac{a_1}{a_2}\eta)\right]}-\right.$$

$$\left.-\frac{K_2(\eta)K_1(\frac{a_1}{a_2}\eta)\left(\frac{r_2}{a_2}\eta Y_1(\frac{r_2}{a_2}\eta)-\frac{r_1}{a_2}\eta Y_1(\frac{r_1}{a_2}\eta)\right)}{\eta^2(\frac{r_2^2}{a_2^2}-\frac{r_1^2}{a_2^2})\left[K_1(\frac{a_1}{a_2}\eta)K_2(\eta)-K_1(\eta)K_2(\frac{a_1}{a_2}\eta)\right]}\right]\times$$

$$\times\left[\frac{\eta\frac{r_1}{a_2}\left[K_2(\frac{a_1}{a_2}\eta)J_1(\frac{r_1}{a_2}\eta)-K_1(\frac{a_1}{a_2}\eta)Y_1(\frac{r_1}{a_2}\eta)\right]}{K_2(\frac{a_1}{a_2}\eta)\left[K_1(\frac{r_1}{a_2}\eta)Y_1(\frac{r_1}{a_2}\eta)-K_2(\frac{r_1}{a_2}\eta)J_1(\frac{r_1}{a_2}\eta)\right]}+\right.$$

$$\left.+\frac{\eta\frac{r_2}{a_2}\left[K_1(\eta)Y_1(\frac{r_2}{a_2}\eta)-K_2(\eta)J_1(\frac{r_2}{a_2}\eta)\right]}{K_2(\eta)\left[K_1(\frac{r_2}{a_2}\eta)Y_1(\frac{r_2}{a_2}\eta)-K_2(\frac{r_2}{a_2}\eta)J_1(\frac{r_2}{a_2}\eta)\right]}\right]-$$

$$\left.-\frac{k_p^2(1+\sigma^E)}{1-k_p^2}\frac{\eta\frac{r_1}{a_2}\left(\frac{r_2}{a_2}\eta Y_1(\frac{r_2}{a_2}\eta)-\frac{r_1}{a_2}\eta Y_1(\frac{r_1}{a_2}\eta)\right)\left[J_1(\frac{r_1}{a_2}\eta)K_2(\frac{a_1}{a_2}\eta)-Y_1(\frac{r_1}{a_2}\eta)K_1(\frac{a_1}{a_2}\eta)\right]}{K_2(\frac{a_1}{a_2}\eta)\left[K_1(\frac{r_1}{a_2}\eta)Y_1(\frac{r_1}{a_2}\eta)-K_2(\frac{r_1}{a_2}\eta)J_1(\frac{r_1}{a_2}\eta)\right]}\right. \tag{22}$$

Resonance and antiresonance follow the same conditions ($Y\to\infty$ for resonance and $Y\to 0$ for antiresonance), but the formulae are not listed here because of their long expressions.

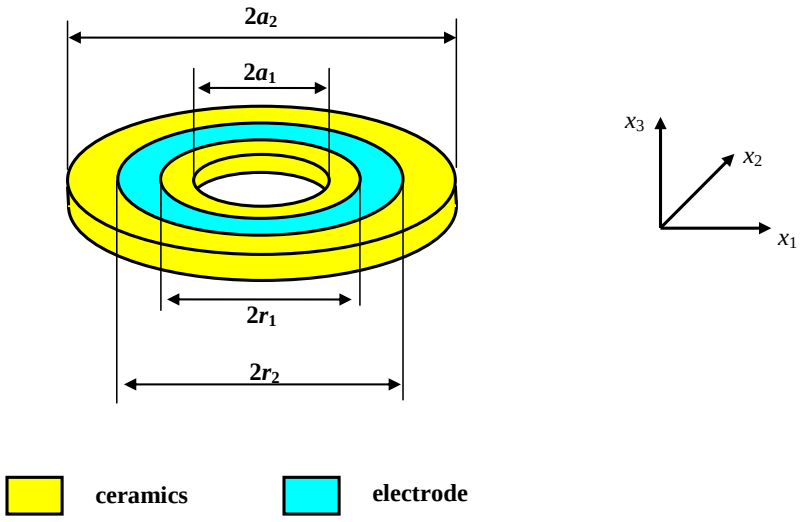

Fig. 4. *Partially electroded ring resonator – thickness poled*

3. Experiment and numerical calculations

Resonance and antiresonance wave numbers η_r and η_a were calculated as solutions of Eqs. (12) and (13) for a thin bar in transverse longitudinal vibration mode, Eqs. (16) and (17) for a thin bar in longitudinal mode, Eqs. (20) and (21) for a thin disc vibrating in radial mode and from Eq. (22) for a thin ring. Resonance and antiresonance frequencies are simply related to the wave numbers for each vibration mode. Therefore ECF's definition - Eq. (1) - could be written as:

$$k_{eff}^2 = \frac{\eta_a^2 - \eta_r^2}{\eta_a^2} \tag{23}$$

For the numerical values of material property coefficients used in calculations, see Table 1.

Table 1. *Material properties of PZT ceramics used in calculations*

Ceramics type	k_{31} [-]	k_{33} [-]	k_p [-]	σ^E [-]
APC841 Hard PZT	0.27	0.63	0.60	0.30
APC850 Soft PZT	-	-	0.63	0.35

Partially electroded resonators were accomplished for bar, disc and ring resonators from soft and hard PZT ceramics (APC International Ltd., Mackeyville, PA, USA). Electrodes were deposited by air-dry Ag-paste (Agar Scientific, Silver paint type G302). Impedance spectra were measured by Agilent 4294A Impedance analyzer.

Samples of partially electroded disc resonators were prepared from soft PZT ceramics, type APC850. Disc dimensions were 20 mm diameter and 1.78 mm thickness and 26.25 mm diameter and 2 mm thickness. A set of samples with electrode aspect ratios ranging from 0.1 to 1.0 was prepared for both dimensions. Samples of partially electroded bar resonators were made from hard PZT, type APC841. Sample dimensions were 49.6 mm long, 6 mm wide and 0.5 mm thick. A set of samples with electrode aspect ratios from 0.1 to 1.0 was prepared. The samples of partially electroded ring resonators were made from hard PZT, type APC841. The ring inner diameter was 20 mm, outer diameter 50 mm and thickness 6 mm. Because there are too many combinations of dimensions, only three sets of samples were prepared. The first set was from samples with outer electrode diameter equal to the ring outer diameter. The second set of samples included samples with electrode inner diameter equal to the ring inner diameter. The samples in the third set had electrodes distributed symmetrically with respect to the center diameter (35 mm diameter) – for details on dimensions, see Table 2.

Table 2. *Dimensions of partially electroded ring resonators (total diameter 20 mm/50 mm/thickness 6 mm)*

Set No.	Inner electrode diameter/outer electrode diameter [mm]				
1	24/50	28/50	32/50	36/50	40/50
2	20/30	20/34	20/38	20/42	20/46
3	32/38	29/41	26/44	23/47	-

4. Results and discussion

ECF for partially electroded bar resonators (k_{31}-mode) shows dependence on the electroded part aspect ratio (i.e. l_0/l) with saturated value starting at the aspect ratio l_0/l = 0.6 – see Fig. 5. Calculated data fits experimental data for all aspect ratios. Maximum ECF k_{eff} = 0.26 was measured for the electrode size aspect ratio equal to l_0/l = 0.75 for k_{31}-mode for the bar resonator.

Calculations for the bar resonator vibrating in k_{33}-mode (Fig. 6) show similar aspect ratio dependence as the bar resonator working in k_{31}-mode, but with higher values of ECF due to the higher electromechanical coupling factor k_{33} of used PZT. Maximum ECF k_{eff} = 0.67 was calculated for the electrode size aspect ratio equal to l_0/l = 0.75 for k_{33}-mode for the bar resonator with embedded electrodes.

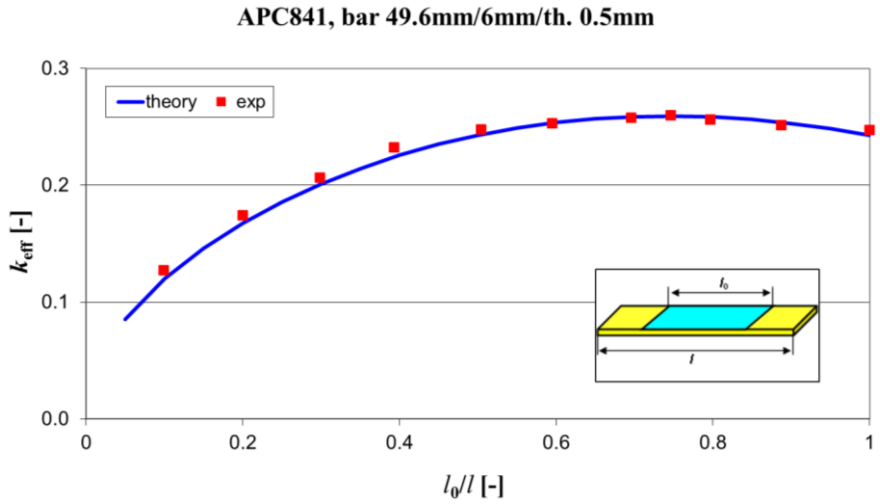

Fig. 5. *Effective coupling factor for partially electroded bar resonators (k_{31}-mode, APC841, 49.6 mm x 6 mm x 0.5 mm)*

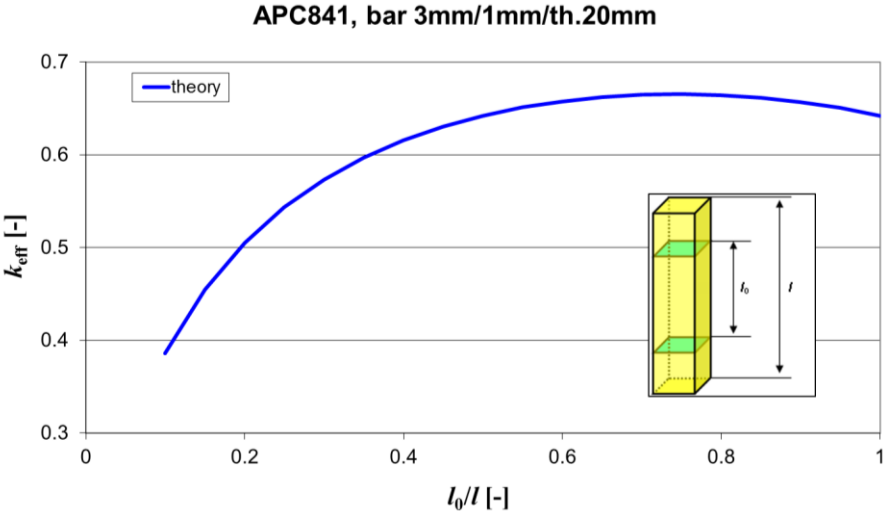

Fig. 6. *Effective coupling factor for the bar resonators with embedded electrodes (k_{33}-mode, APC841, 20 mm x 3 mm x 1 mm)*

ECFs for partially electroded disc resonators (k_p-mode) show saturation at the aspect ratio (i.e. electrode's diameter / total diameter) equal to about r_0/a = 0.7 – see Fig. 7. Calculated data fit the experimental values only for the aspect ratios below r_0/a = 0.5. The approximation employed in calculations is not valid for higher values of aspect ratios, because no electroded outer ring segment can any longer be approximated by the shape of the thin ring. The samples with different disc diameters

exhibit the same behavior in ECF as it is seen in Eq. (18) and in Fig. 7. ECF depends on the values of the electromechanical coupling factor k_p, Poisson's ratio σ^E, but not on the disc diameter like the resonance and antiresonance frequencies themselves. Maximum ECF k_{eff} = 0.58 was measured for the electrode size aspect ratio equal to r_0/a = 0.80 for k_p-mode for the disc resonator. This value agrees well with the previously published [7] theoretical value k_{eff} = 0.55 for the electrode size aspect ratio equal to r_0/a = 0.83 calculated for a different PZT type.

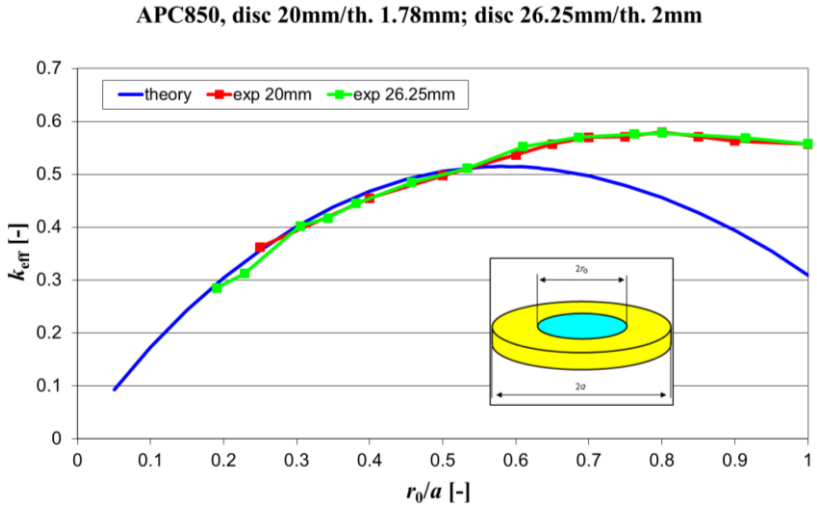

Fig. 7. *Effective coupling factor for partially electroded disc resonators (k_p-mode, APC850, 20 mm diameter / 1.78 mm and 26.25 mm thick / 2 mm thick)*

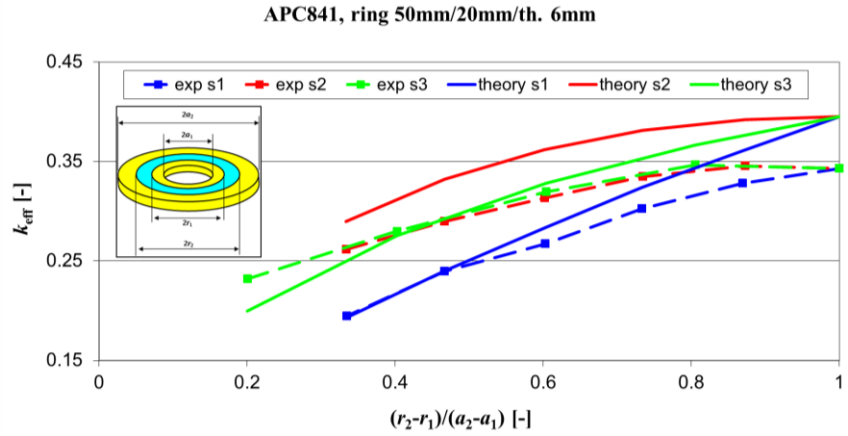

Fig. 8. *Effective coupling factor for partially electroded ring resonators (k_p-mode, APC841, 20 mm/50 mm diameter / 6 mm thickness) as a function of ring electrode relative width*

All three sets of partially electroded rings exhibit the same trend in ECF with the highest value k_{eff} = 0.34 for the ring resonator with full electrode, see Fig. 8. Set No. 1 and 3 fit theoretical calculations up to the electrode width aspect ratio equal to 0.7. Calculations for set No. 2 (inner electrode diameter is equal to disc inner diameter) show higher values than it was measured, on the contrary. Some differences in the calculated values are due to the approximations employed for one-dimensional calculations of ring electrode. Data shows the same trend in the calculated as well as in the measured values of ECF.

5. Conclusions

Effective ECF reaches its top value at an optimum electrode size for all studied resonator cases (bar, disc and ring). Values of effective ECFs were predicted in analytical one-dimensional models for thin bar (k_{31}-mode), thin disc (k_p-mode) and thin ring (k_p-mode) with partial electrodes and thin bar with embedded electrodes (k_{33}-mode). Numerically calculated effective ECFs were measured on the samples of bar, disc and ring resonators with partial electrodes. Maximum effective ECFs were measured:

- k_{eff} = 0.26 for thin bar (k_{31}-mode) for the aspect ratio l_0/l = 0.75
- k_{eff} = 0.58 for thin disc (k_p-mode) for the aspect ratio r_0/a = 0.80
- k_{eff} = 0.34 for thin ring (k_p-mode) for the resonator with full electrode (outer / inner ring diameters are 50 mm/20 mm).

Maximum ECF for bar resonator with embedded electrodes (k_{33}-mode) was calculated as k_{eff} = 0.67 for the electrode aspect ratio l_0/l = 0.75. ECF saturates at the aspect ratio of r_0/a = 0.7 for the thin disc with partial electrode. Ring resonators show the same trend as discs without saturation of ECF. The presented results may serve as a guide for the optimum electrode pattern design for resonators with partial electrodes.

Acknowledgements

This work was supported by ESF operational program "Education for competitiveness" in the Czech Republic within the framework of project "Support of engineering of excellent research and development teams at the Technical University of Liberec" No. CZ.1.07/2.3.00/30.0065.

References

[1]. Chang S. H., Rogacheva N. N., Chou C. C., *Analysis of methods for determining of electromechanical coupling coefficients of piezoelectric elements*, IEEE Transactions on Ultrasonics Ferroelectrics and Frequency Control, 42(4), p. 630-640, 1995.

[2]. Mezheritskiy A. V., *Invariants of electromechanical coupling coefficients in piezoceramics*, IEEE Transactions on Ultrasonics Ferroelectrics and Frequency Control, 50(12), p. 1742-1751, 2003.

[3]. IRE Standards on Piezoelectric Crystals, *Measurement of Piezoelectric Ceramics*, Proceedings of the IRE, 49(7), p. 1161-1169, 1961.

[4]. Huang C. H., Lin Y. C., Ma C. C., *Theoretical Analysis and Experimental Measurement for Resonant Vibration of Piezoceramic Circular Plates*, IEEE Transactions on Ultrasonics Ferroelectrics and Frequency Control, 51(1), p. 12-24, 2004.

[5]. Huang C. H., *Theoretical and experimental vibration analysis for a piezoceramic disk partially covered with electrodes*, The Journal of the Acoustical Society of America, 118(2), p. 751-761, 2005.

[6]. Ivina N. F., *Analysis of the Natural Vibrations of Circular Piezoceramic Plates with Partial Electrodes*, Acoustical Physics 47(6), p. 714-720, 2001.

[7]. Rogacheva N. N., *The dependence of the electromechanical coupling coefficient of piezoelectric elements on the position and size of the electrodes*, Journal of Applield Mathematics and Mechanics, 65(2) p. 317-326, 2001.

[8]. Meitzler A. H., O'Bryan Jr. H. M., Tiersten H. F., *Definition and measurement of radial mode coupling factors in piezoelectric ceramic materials with large variations in Poisson's ratio*, IEEE Transactions on Sonics and Ultrasonics, SU-20(3), p. 233-239, 1973.

THE ANNALS OF "DUNAREA DE JOS" UNIVERSITY OF GALATI
FASCICLE IX. METALLURGY AND MATERIALS SCIENCE
Nº. 2 - 2015, ISSN 1453 – 083X

SELECTIVE RECOVERY BY SOLUBILIZATION OF METALS IONS OF CHROMIUM, IRON AND ZINC FROM ELECTROPLATING SLUDGE TO DEVELOP PIGMENTS FOR CERAMICS INDUSTRY

MĂRCUȘ Maria-Iuliana[a,*], VLAD Maria[b], MÎȚIU Ileana[a], MÎȚIU Mihaela Andreea[a]

[a] National Institute for Research and Development in Environmental Protection – INCDPM, 294, Spl. Independentei, 6th District, Bucharest, Postal Code 060031, Romania

[b] "Dunărea de Jos" University of Galati, Faculty of Engineering, 47 Domnească Street, RO-800008, Galati, Romania

[*] Corresponding author: iuliaholy@yahoo.com

ABSTRACT

Electroplating industries discharge large amounts of heavy metals, including chromium (Cr), iron (Fe) and zinc (Zn) ions, in the wastewater resulted from technological processes, as well as in the sludge from wastewater treatment.

In this paper are reported the results of the scientific activity developed in laboratory to recover Cr(VI,III), Fe(III), and Zn(II) from the galvanic sludge by selective solubilization and to obtain metal salts which can afterwards be used as pigments in ceramics industry.

Chromium recovery from the sludge was performed by alkaline sludge oxidation to obtain salts of Cr(VI). We aimed at obtaining two types of pigments based on chromium: chromium yellow pigments by precipitation of Cr(VI) in the form of lead chromate ($PbCrO_4$) and chromium green pigments by reducing Cr(VI) and its precipitation in the form of Cr(III).

Red pigment based on Fe(III) was obtained by solubilizing the resulting sludge after the recovery of chromium and iron precipitation at a pH corresponding to the complete precipitation.

From the remaining solution by recovering Cr and Fe, Zn was recovered as zinc hydroxide [$Zn(OH)_2$] that can be used as raw material in the ceramics industry.

In the experiments performed at laboratory scale, optimal technological parameters were set for the selective recovery of the tested sludge metal ions.

KEYWORDS: electroplating sludge, chromium, iron, zinc, selective recovery

1. Introduction

Treatment and metal surfaces coating processes require the use of hazardous chemical substances which are further discharged as process waste solutions and washing wastewater. The process waste solutions which are regularly discharged come from the metal surfaces preparing operations (degreasing, pickling, passivating, polishing, etching) and from the discharge of active washing wastewater (copper plating, nickel plating, chrome plating, zinc plating, cadmium plating). The technological solutions are discharged when they cannot fit in the technological work parameters through corrections or when the work technology is changed [1].

Given the high concentrations of metallic ions, the main source of wastewater with such content is represented by the process waste solutions which actually have a share of 90-95 % from the amount of discharged salts together with wastewaters from metal plating workshops.

Waters and concentrated solutions from chemical and electrochemical processing operations of metal surfaces are treated through two technologies [2]:

- treatment technologies to result sludge (metal ions precipitation / solid ion exchange prehension / recycled chemical washing, etc.).
- recovery treatment technologies in order to avoid sludge formation and to recover useful compounds.

Collecting and treating waste water (washing water and wastewater concentrates) with heavy metals content (copper, trivalent chromium, cadmium, nickel, zinc, iron, etc.), cyanide and hexavalent chromium are jointly performed, resulting in a precipitation sludge with complex chemical composition, classified as a hazardous waste / eco-toxic waste. Removing it by landfilling implies environmental risks, because of the risk of rainwater leaching (pH = 5.0 – 5.5) of heavy metals content, which leads to soil and surface pollution and to ground water pollution. These treatment processes were originally designed only for retaining toxic substances from water, but they were later adapted to the possibility to recover metal compounds.

The recovery of industrial waste is one of the main national and international research themes concerning the reuse technologies in various industries, correlated with the environmental impact. The reuse potential represents the essential criterion in the waste management approach. From this point of view, the equivalence between the concept of waste and the concept of secondary raw material is increasing [3, 4].

In the following part is presented a process for the selective recovery of metal ions such as chromium (Cr), iron (Fe), zinc (Zn) from the solid sludge resulted from wastewater treatment from a company with activities in the chemical and electrochemical treatment of metal surfaces, namely: galvanizing of metal surfaces.

2. Experimental results

The scientific experiments at laboratory scale have been performed in order to recover Cr(VI,III), Fe(III), and Zn(II) ions from the galvanic sludge by selective solubilization and to obtain metal salts. The galvanic sludge employed in this research was collected from a local plant, after the waste solutions and washing wastewater treatment. The sludge to be tested was milled in a porcelain jar to obtain particles <1 μm in order to increase the reaction surface and was dried at 105 ºC for 24 h (the water content of the sludge was 68 wt.%). The waste was characterized by atomic absorption spectrometry in order to estimate the chromium, iron and zinc content.

The physico-chemical analyses performed on the galvanic sludge revealed the following chemical composition towards dry substance, expressed in percentage (%). This composition is presented in Table 1:

Table 1. *Physico-chemical composition of the analyzed galvanic sludge*

Ions	% towards dry substance	The total amount of the metals in 150 g of sample (g)
Cr	0.27	0.4050
Fe	9.10	13.6500
Zn	18.10	27.1500
Ni	0.05	0.0750
Cu	0.009	0.0135
Cd	0.004	0.0060

2.1. Chromium recovery

The experiments conducted in the laboratory led to the establishment of a procedure for recovering chromium from the galvanic sludge resulting from the galvanic wastewater treatment. The technology of wastewater neutralization is based on the detoxification of waste by reducing chromium (VI) to chromium (III) and then using a hydroxide to precipitate insoluble chromium (III) hydroxide. Other metal hydroxides are also precipitated in the resulting sludge [5, 6].

The chromium recovery procedure includes the alkaline oxidation of Cr(III) to Cr(VI) and Cr(VI) recovery by precipitation.

The phases of chromium recovery procedure are presented in Fig. 1.

PHASE 1: Solubilization of Cr(III) through alkaline oxidation

Solubilization of Cr(III) has been performed from 150 g of the galvanic sludge sample through alkaline oxidation at pH = 12.0-12.5, with sodium hypochlorite (NaOCl) 12% and sodium hydroxide (NaOH) 30%; reaction temperature = 80 ºC, reaction time = 30 minutes; stirring throughout the reaction time.

$$2Cr(OH)_3 + 3NaOCl + 4NaOH = 2Na_2CrO_4 + 3NaCl + 5H_2O \quad (1)$$

Simultaneously with chromium oxidation, a partial oxidation reaction of Fe(II) to Fe(VI) also occurred, in the form of sodium perferrate (Na_2FeO_4), insoluble compound at this stage which will remain in the sludge cake after solution filtering:

$$Fe(OH)_2 + 2\ NaOCl + 2\ NaOH = Na_2FeO_4 + 2\ NaCl + 2\ H_2O \quad (2)$$

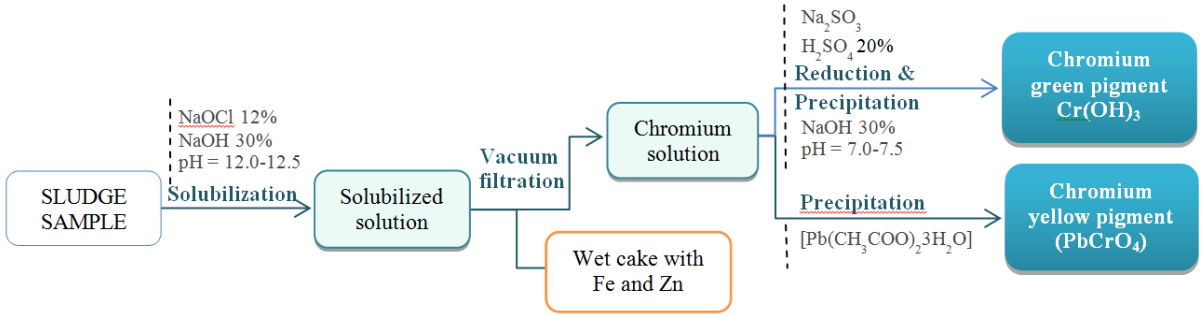

Fig. 1. *The scheme of chromium recovery procedure from galvanic sludge*

PHASE 2: Filtering the chromium solution

Filtering the chromium solution was performed using a vacuum pump, yielding a wet cake containing mainly zinc and iron and a solution of sodium chromate (Na_2CrO_4) which will be subject to processing in order to obtain chrome pigments.

PHASE 3: Washing wet cake from filtration

Washing the wet cake resulting from filtration with vacuum pump was performed for the full recovery of chromium absorbed by the cake.

In the experiments we attempted to obtain two different types of pigments based on chromium:

- chromium yellow pigment by precipitation of hexavalent chromium in the form of lead chromate;
- chromium green pigment by reduction of hexavalent chromium to trivalent chromium and its precipitation in the form of chromium hydroxide.

PHASE 4: Precipitation Cr(VI) with lead acetate [$Pb(CH_3COO)_2 3H_2O$] in the form of lead chromate (PbCrO4) – resulting chromium yellow pigment (Fig. 2).

$$Na_2CrO_4 + Pb(CH_3COO)_2 = PbCrO_4 + 2NaCH_3COO \quad (3)$$

Fig. 2. *Chromium yellow pigment ($PbCrO_4$)*

PHASE 5: Reducing Cr(VI) to Cr(III), in acid medium (H_2SO_4 20%) with sodium sulfite (Na_2HSO_3) and its precipitation with sodium hydroxide (NaOH)30% in the form of chromium hydroxide [$Cr(OH)_3$] - chromium green pigment (Fig. 3).

$$2\ Na_2CrO_4 + 3\ Na_2SO_3 + 5\ H_2O = 2\ Cr(OH)_3 + 3\ Na_2SO4 + 4\ NaOH \quad (4)$$

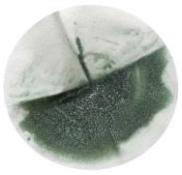

Fig. 3. *Chromium green pigment $Cr(OH)_3$*

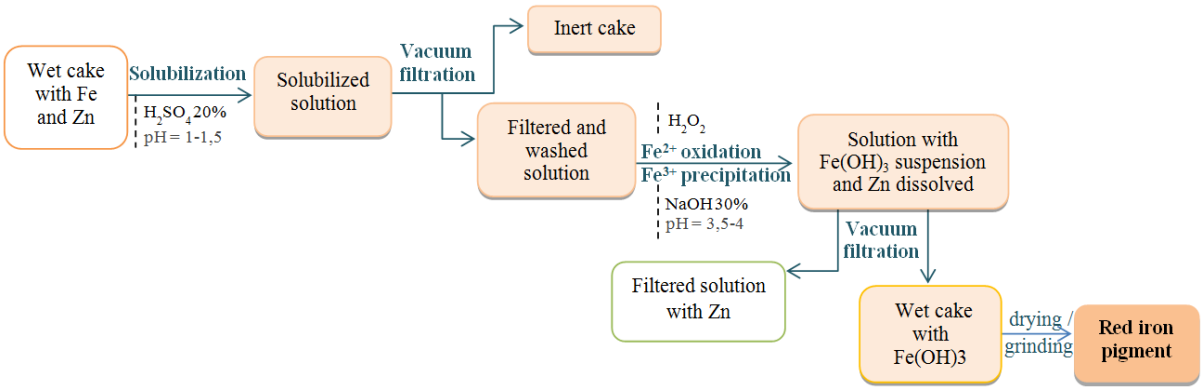

Fig. 4. *The scheme of iron recovery procedure*

2.2. Iron recovery

Iron is present in the cake obtained after chromium recovery, in the form of compound of Fe(II), Fe(III) and Fe(VI). Fe (VI) was obtained in the first phase of a chrome recovery process by partial oxidation of Fe(II) to Fe(VI) in the form of sodium perferrate (Na_2FeO_4).

The phases of iron recovery procedure are presented in Fig. 4.

PHASE 1: Solubilization of the sludge cake remaining after chromium recovery

The solubilization of the sludge cake was performed with sulfuric acid (H_2SO_4) 20% at pH = 1.0–1.5; reaction temperature = 90 ºC; reaction time = 30 minutes; stirring throughout the reaction time.

The iron compounds solubilizing reactions are the following:

$$Na_2FeO_4 + 16\ H_2SO_4 + 3Fe_3O_4 = 5Fe_2(SO_4)_3 + Na_2SO_4 + 16H_2O \quad (5)$$

$$2Fe(OH)_3 + 3H_2SO_4 = Fe_2(SO_4)_3 + 6H_2O \quad (6)$$

$$Fe(OH)_2 + H_2SO_4 = FeSO_4 + 2H_2O \quad (7)$$

Simultaneously with iron solubilization, the solubilization of Zn(II) also occurred, according to the following chemical reaction:

$$Zn(OH)_2 + H_2SO_4 = ZnSO_4 + 2H_2O \quad (8)$$

PHASE 2: Filtering the solution

After the solubilization of the sludge cake, the resulting solution was filtered with a vacuum pump, resulting a solution containing Fe(II), Fe(III) and Zn(II) and the wet cake with small traces of metal ions.

PHASE 3: *Oxidation of Fe(II) to Fe(III)*

The oxidation reaction was performed in two stages: in the first stage with sodium hypochlorite (NaOCl) and sodium hydroxide (NaOH) along with Cr(III) (as mentioned above) and the second oxidation step with hydrogen peroxide (H_2O_2), reaction temperature = 90 ºC, reaction time = 30 minutes; stirring throughout the reaction time.

The chemical reaction was:

$$2FeSO_4 + H_2SO_4 + H_2O_2 = Fe_2(SO_4)_3 + 2H_2O \quad (9)$$

PHASE 4: Complete precipitation of Fe(III)

The ferric sulphate [$Fe_2(SO_4)_3$] formed in the previous steps was precipitated at pH = 3.5- 4 with sodium hydroxide (NaOH) 30%; temperature reaction - ambient, reaction time = 15 minutes, stirring throughout the reaction time, to obtain a suspension of iron hydroxide. The chemical reaction was:

$$Fe_2(SO4)_3 + 6\ NaOH = 3\ Na_2SO_4 + 2\ Fe(OH)_3 \quad (10)$$

PHASE 5: *Filtering the suspension obtained after precipitation of Fe (III) with a vacuum pump and washing the wet cake from filtration for full recovery of red iron pigment (Fig. 5).*

The zinc recovery was performed from the remaining solution after iron recovery.

The phases of zinc recovery procedure are presented in Fig. 6.

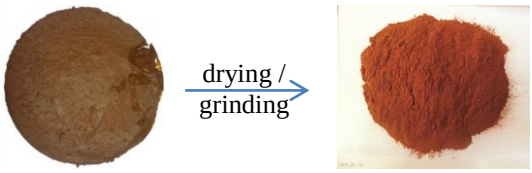

Fig. 5. *Wet cake of iron* *Red iron pigment $Fe(OH)_3$*

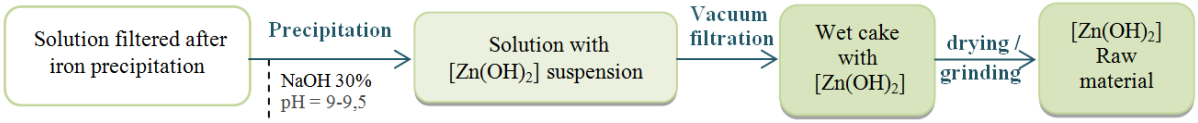

Fig. 6. *Scheme of zinc recovery procedure*

PHASE 1: Precipitation of Zn

The precipitation was performed with sodium hydroxide (NaOH) 30% by raising the pH of 4 to 9-9.5; reaction temperature - ambient, reaction time = 15 minutes.

The pH was raised from 4 to 9-9.5 to ensure the complete precipitation of zinc.

$$ZnSO_4 + 2NaOH = Zn(OH)_2 + Na_2SO_4 \quad (11)$$

PHASE 2: Filtering the solution with a vacuum pump and washing the wet cake from filtration for full recovery of zinc as zinc hydroxide $[Zn(OH)_2]$ (Fig. 7).

Fig. 7. *Zinc hydroxide $[Zn(OH)_2]$*

This scientific activity at laboratory scale led to selective recovery efficiency for the studied metal ions of: 84.20 % for chromium; 99.93 % for iron; 85.74 % for zinc (Table 2).

Table 2. *Metal ions recovery efficiency*

Ions	The initial amount of metals in the sludge sample (g)	The total recovered amount of metals in solution (g)	Recovery efficiency (%)
Cr	0.4050	0.3410	84.20
Fe	13.6500	13.6410	99.93
Zn	27.1500	23.2771	85.74

4. Conclusions

The main conclusions of this experimental research are:

The recovery efficiency for the 3 metals ions is considered quite satisfactory but future research will continue to improve it by establishing optimal technical parameters and to obtain an inert sludge cake behaving as an inert material in terms of recovery of useful compounds which are the topic of this research.

The experiments conducted in the laboratory led to the obtaining of: Chromium yellow pigment ($PbCrO_4$), Chromium green pigment $Cr(OH)_3$, Red iron pigment $Fe(OH)_3$; zinc hydroxide $[Zn(OH)_2]$ as raw material.

Future research will focus on analyzing the possibilities for capitalization of metal ions recovered as pigments in glazes for ceramic products industry.

References

[1]. L Oniciu, E. Grunwald, *Galvanotehnica*, Scientific and Encyclopedic Publishing, Bucharest, 1980.
[2]. Tonni Agustiono Kurniawana, Gilbert Y. S. Chana, Wai-Hung Loa, Sandhya Babelb, *Physico-chemical treatment techniques for wastewater laden with heavy metals*, Chemical Engineering Journal, vol. 118, issues 1-2, p. 83-98, 1 May 2006.
[3]. BREF, *Waste Treatments*, august 2006.
[4]. INCDPM Bucharest, *The hazardous waste neutralization technologies, capitalizing them in vitreous and ceramic materials*, Project 2008-2011, Bucharest.
[5]. I. Bojanowska, *Recovery of Chromium from Sludge Formed after Neutralization of Chromic Wastewater*, Polish J. Environ. Stud., 11(2), 117, 2002.
[6]. I. Bojanowska, *Recovery of Chromium from Galvanic Wastewater Sludge*, Polish J. Environ. Stud., 11(3), 225, 2002.

THE ANNALS OF "DUNAREA DE JOS" UNIVERSITY OF GALATI
FASCICLE IX. METALLURGY AND MATERIALS SCIENCE
Nº. 2 - 2015, ISSN 1453 – 083X

CONDUCTIVE-ATOMIC FORCE MICROSCOPY INVESTIGATION OF THE ELECTRICAL PROPERTIES OF LOW TEMPERATURE DEPOSED ZnO TRANSPARENT THIN FILMS

A. ALEXA[1], A. PIMENTEL[2], T. CALMEIRO[2], A. ISTRATE[3], E. FORTUNATO[2], V. MUȘAT[1]*

[1] Center of Nanostructures and Functional Materials - CNFM, Faculty of Engineering, "Dunarea de Jos" University of Galati, Galati, Romania
[2] CENIMAT/I3N, Departamento de Ciencia dos Materiais, Faculdade de Ciencias e Tecnologia, FCT, Universidade Nova de Lisboa (UNL), and CEMOP/UNINOVA, Caparica, Portugal
[3] National Institute for R & D in Microtechnologies (IMT), Erou Iancu Nicolae Str. 126A, Bucharest 077190, Romania
e-mail: viorica.musat@ugal.ro

ABSTRACT

The paper presents the investigation by conductive-atomic force microscopy (C-AFM) of the variation of the local conductivity and topography of the transparent ZnO thin films deposed onto soda lima glass substrates by spin-coating of pre-prepared ZnO nanoparticles. With conductivity measurements at the nanometer level, the chemical and crystalline structure of the thin films obtained at temperature below 200 °C was investigated by Fourier transform infrared (FTIR) spectroscopy and X-ray diffraction, respectively, as a function of the number of the deposed layers and conditions of their deposition, such as deposition rate and the temperature of post-deposition annealing. The increase of the thermal treatment temperature, from 120 to 180 °C, leads to increased values of all thin films, most notably for the thickest sample with three layers deposed at 500 rpm that shows the highest decrease of thickness, indicating the highest compaction. The samples with three layers post-treated at 180 ºC show grain growth associated with increased roughness.

KEYWORDS: ZnO nanoparticles, transparent thin films, spin-coating, microstructure, conductive atomic force microscopy

1. Introduction

Due to the recent development of transparent and flexible electronics, there is a growing interest in depositing transparent thin-film metal-oxide semiconductors at low temperature that can provide flexibility, lighter weight, and potentially lead to cheaper manufacturing processing.

Zinc oxide, which is an II-VI group semiconductor with a broad energy band (3.37 eV), high thermal and mechanical stability even at room temperature, is a very attractive material for potential applications in electronics, optoelectronics and laser technology [1].

When using polymer flexible substrate, the device processing temperatures should not exceed 80 ºC, 150 ºC, 300 ºC for polyethylene terephthalate (PET), polyethylene naphtalate (PEN) and Polyimide (PI) substrates in order to avoid their degradation [2]. For this low temperatures processing, one potential route is represented by deposition of pre-prepared oxide nanoparticles dispersions.

There are more methods for the preparation of ZnO-based thin films, such as sol-gel, supercritical precipitation, colloidal synthesis, vapor-phase oxidation, thermal vapor transport and condensation, chemical vapor deposition, micro-emulsion, spray pyrolysis, combustion method and organometallic synthesis [3-7].

The efficient use of transparent thin films in flexible electronics applications requires advanced knowledge of their electrical properties at micro/ nano level. Conventionally, the study of electrical proprieties is done by four-point probe method that measures the average value of the electrical resistivity of the thin film at the macroscopic level. In contrast,

conductive-atomic force microscopy (C-AFM) technique allows obtaining a mapping of the local variations in the conductivity of the thin films surface at high spatial resolution of variations in height and current response simultaneously, giving information about the local electronic structure for a local morphology. This method allows to quantitatively investigate the electron transport at the nanometer-scale (nm-scale) [8].

In the present paper, we have used C-AFM to map the local conductivity variations of transparent ZnO thin films deposed onto soda lima glass substrates by spin coating, using an alcohol dispersion of ZnO nanoparticles pre-prepared from solution. The chemical and crystalline structure of the thin films obtained at temperature below 200 ºC was investigated by Fourier transform infrared (FTIR) spectroscopy and X-ray diffraction, respectively, as a function of the number of the deposed layers and conditions of their deposition, i.e. deposition rate and the temperature of post-deposition annealing.

2. Experimental details

2.1. Materials and synthesis of ZnO nanoparticles

Zinc acetate dehydrate (purity >98%), potassium hydroxide and methanol (purity ≥99%) were purchased from Sigma Aldrich and were used without further purification.

For the synthesis of ZnO nanoparticles, two methanol solutions, A (KOH) and B (zinc acetate dehydrate), were prepared by getting dissolved in methanol under reflux at 60 °C. Over the solution A, solution B was added and the mixture was heated under reflux and magnetic stirring to precipitate ZnO NPs. High-speed centrifugation (9000 rpm) was used for the separation of ZnO NPs from the mother solution, and for each centrifugation step, a washing with ethanol was applied. The obtained powder was finally dried in air at 100 °C.

2.2. Thin film preparation

The prepared ZnO NPs were re-dispersed in methanol and deposed on soda lima glass substrates as thin films by spin-coating using Spin-Coater WS-650SZ-8NPP AS, Laurell. Single-layered (labeled with F1 to F4 in Table 1) and three-layered thin films samples (labeled with F5 to F8 in Table 1) were deposed at 500 and 1000 rpm and annealed at 120 and 180 °C.

2.3. Nanoparticles and thin films characterization

The thickness of the deposed thin film was measured with NanoCalc-XR type refractometer.

The crystalline structure of the investigated films was evaluated by X-ray diffraction on grazing incidence geometry using a PANalytical's X'Pert PRO MRD X-ray diffractometer in the 2θ scanning range of 20° - 70°, using a monochromatic CuK_α radiation source (wavelength 1.540598 Å). The average crystallite size (L) of ZnO thin films was calculated based on Debye-Scherrer's equation:

$$B(2\theta) = (K\cdot\lambda)/(L\cdot\cos\theta) \quad (1)$$

where B is the full width at half of the maximum intensity (FWHM) of the peak, λ is the X-ray wavelength, θ is the diffraction angle and K is the Scherrer's constant whose value for spherical particles is 0.89 [10].

The active functional groups inside the films were identified by Fourier Transform Infrared (FT-IR) measurements, in the spectral region of 500–4500 cm^{-1}, using a Nicolet 6700 FTIR spectrometer.

Table 1. *Experimental deposition parameters and thickness of the investigated films*

Sample symbol	No. of layers	Deposition rate (rpm)	Annealing temperature (°C)	Film thickness (nm)
F1	1	500	120	271
F2			180	216
F3		1000	120	173
F4			180	126
F5	3	500	120	894
F6			180	558
F7		1000	120	713
F8			180	561

Simultaneous local current and topography measurements were made on the surface of ZnO thin films by conductive-atomic force microscopy (C-AFM) in ambient conditions, with Asylum Research MFP-3D Standalone atomic force microscope operating in contact mode with a 2.504 μm/s scanning speed; samples scanning was performed with a commercial Pt probe (Nanoworld ContPt) having a current sensitivity of 2 nA/V and 10 mV bias. The samples were contacted using a silver paint applied on the back side and margins of the samples. The image resolution is 256 x 256 and the roughness (RMS) was evaluated with Gwyddion software. Conductive channel measurements were overlaid on the AFM image by color mapping.

3. Results and discussions

3.1. Fourier Transform Infrared investigation

Figure 1 shows the FT-IR spectra of the deposed ZnO thin films with different thickness, consisting of one and three layers. All the spectra contain intense transmittance peaks at 550 cm^{-1} attributed to bending and stretching vibrations of Zn–O bond. The increase of their intensity is related to the increase of film thickness (Table 1). Two intense peaks at 1583 and 1414 cm^{-1} in the ZnO spectrum are assigned to the asymmetric and symmetric stretching modes of COO^- acetate groups, not totally removed by the washing procedure. Also a broad band is presented in the range of 3500-3000 cm^{-1} which can be assigned to the stretching modes of OH groups exposed on the particle surface and to the presence of residual water condensed on the surface of thin films.

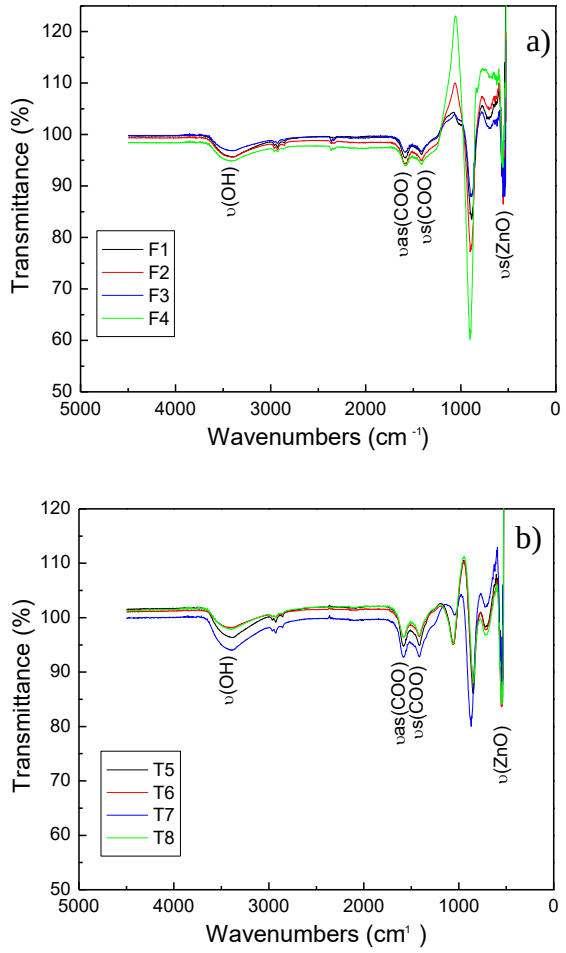

Fig. 1. *The FTIR spectra of thin film samples with one (a) and three layers (b)*

3.2. Microstructural characterization

The XRD pattern of the deposed thin films presented in Figure 2 confirms the polycrystalline wurtzite-type zinc oxide phase. The three main diffraction peaks located at 2θ values of 31.7°, 36.2° and 56.6° are assigned to (100), (110) and (101) crystallographic planes, respectively. The average crystallite size (L) of the obtained thin films, calculated with Debye-Scherrer's for different diffraction peaks, shows different values, as follows: 10-13 nm estimated for (100) and (110) peaks, and 70-120 nm estimated for (101) peak, indicating an anisotropic crystal growth. The three-layered thin films show an increase of intensity of the diffraction peaks with respect to one layer thin films related to the increase of film thickness (Table 1) and crystallinity.

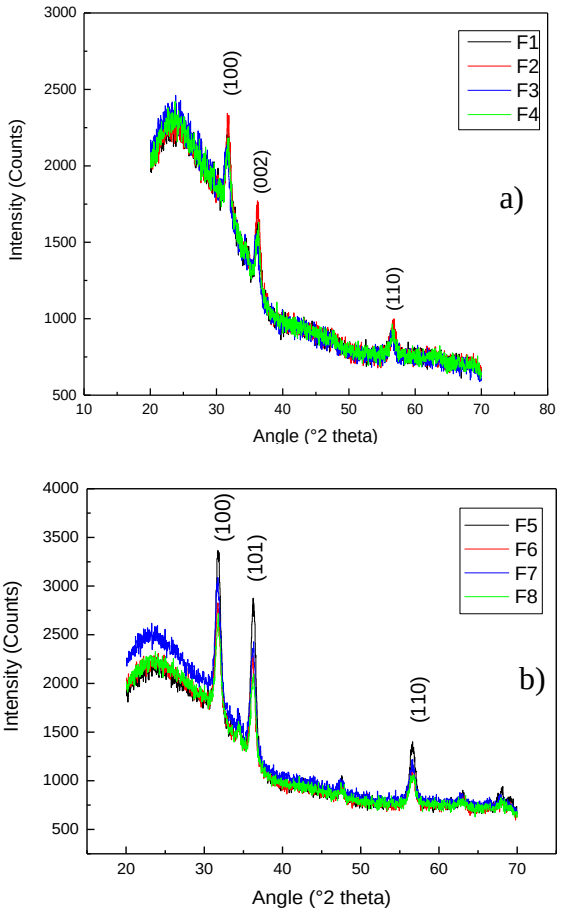

Fig. 2. *X-Ray diffraction patterns of the one layer (a) and three-layer (b) thin films*

3.3. Conductive atomic force microscopy measurements

Figure 3 shows the superposition of current and topography C-AFM mapping of thin film samples, in 2D and 3D presentations. According to the C-AFM topography images, the thin films consist of relatively compact and homogeneous by size and shape roundish grains with diameters between 20 and 60 nm.

Generally, the C-AFM measurements revealed electrically resistive undoped ZnO thin films. In all samples, darker spots between the grains can be observed, indicating no-conductive pore spaces. Based on color tones, different gradients in current can be observed. The highest current gradient, from -11 to 122 pA, was obtained for the most compact sample (F8 in Fig.3).

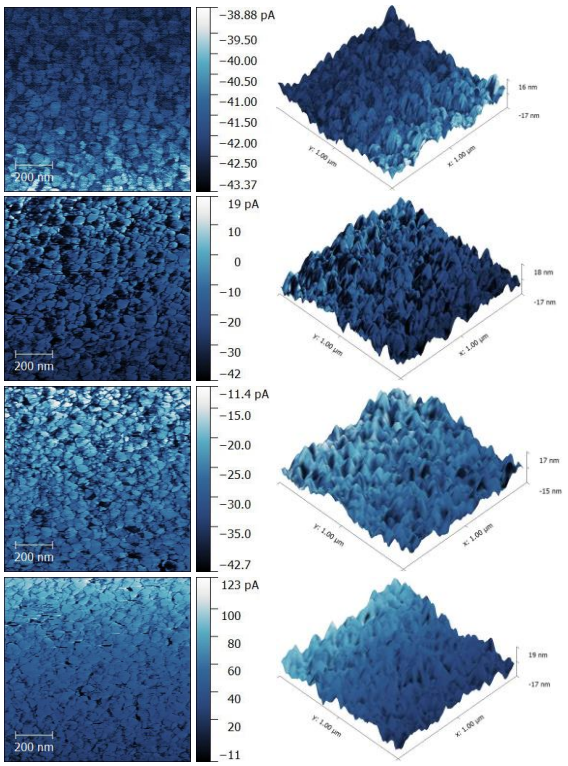

Fig. 3. *C-AFM mapping of three-layer thin film samples, in 2D and 3D presentations*

The influence of the post-deposition temperature on the films thickness, Rms roughness and the highest grain conductivity are quantified in Figure 4. The increase of thermal treatment temperature from 120 °C to 180 °C induced changes in thicknesses, roughness, porosity and conductivity for all the investigated films. Considering the thickness of thin films (Fig 4a), one can observe a shrinkage of all samples, about 20% for samples deposed at 1000 rpm with one (sample F4) and three layers (sample F8). Higher shrinkage of about 27% (sample F2) and 37% (sample F6) can be observed for samples with one and three layers, respectively, deposed at 500 rpm (Fig. 4a).

The increase of the annealing temperature has induced an opposite effect to the surface roughness, depending on the number of layers and deposition rate (Fig 4b). For the films with one layer, the Rms values decrease by 12% and 20% for 1000 and 500 rpm, respectively, while for the samples with three layers the Rms values increased by 9.1 and 8.4% when the deposition rate was 1000 and 500 rpm, respectively (Fig. 4b).

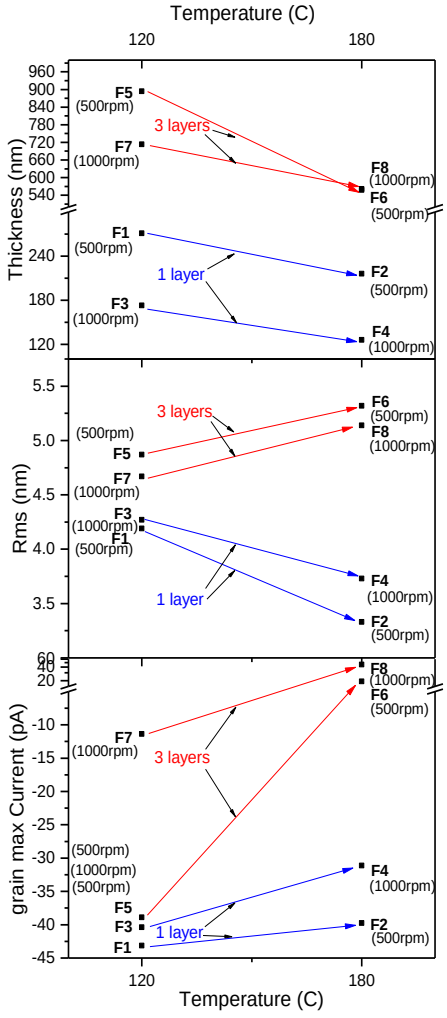

Fig. 4. *Variation of the thin films thickness (a), Rms roughness (b) and maximum peak grain conductivity (c) versus the temperature of the post deposition treatment*

The increase of thermal treatment from 120 °C to 180 °C led to higher conductivity values for all

samples, most notably for the thin film sample with three layers deposed at 500 rpm (Fig. 4c). One can notice an increase of the overall surface current response with the increase of thickness for all samples. The thermal treatment has lowered the value response of grain maximum peak for one-layer samples, which is in accordance with the decreased values of roughness. The best conductivity is achieved by sample F8 as a result of better compaction, lower grain boundary scattering, higher conductivity [11].

4. Conclusions

ZnO thin films were obtained by spin-coating using pre-prepared oxide nanoparticles, at deposition rate of 500 and 1000 rpm and subsequent thermal treatment at 120 and 180 ºC.

The increase of thermal treatment from 120 °C to 180 °C led to increased values of conductivity for all thin films, most notably for the thickest sample with three layers deposed at 500 rpm which showed the highest decrease of thickness, indicating the highest compaction. The samples with three layers post-treated at 180 ºC showed a simultaneous grain growth, associated with an increase of sample roughness.

Acknowledgement

The work of Alexandru Alexa has been funded by the Sectoral Operational Programme Human Resources Development 2007-2013 of the Ministry of European Funds through the Financial Agreement POSDRU/159/1.5/S/132397.

References

[1]. Radzimska A. K., Jesionowski T., *Zinc Oxide - From Synthesis to Application: A Review*, Materials, 7, 2833, 2014.
[2]. Facchetti A., Marks T. J., *Transparent electronics: From synthesis to Applications*, Wiley, 2010, ISBN 978-0-99077-3.
[3]. Pasquarelli R. M., Ginley D. S., O'Hayre R., *Solution processing of transparent conductors: from flask to film*, Chem. Soc. Rev. 2011, 40, p. 5406-5441
[4]. Fortunato E., Barquinha P., Martins R., *Oxide semiconductor thin-film transistors: a review of recent advances*, Advanced materials, 24, p. 2945-86, 2012.
[5]. Fan J. C., Sreekanth K. M., Xie Z., Chang S. L., Rao K. V., *p-Type ZnO materials: Theory, growth, properties and devices*, Progress in Materials Science, 58, 874, 2013.
[6]. Kang Y. H., Jeong S., Min Ko J., Ji-Yo, Lee, Choi Y., Lee C., Cho S. Y., *Two-component solution processing of oxide semiconductors for thin-film transistors via self-combustion reaction*, Journal of Materials Chemistry C, 2, p. 42-47, 2014.
[7]. Schneller T., Waser R., Kosec M., Payne D., *Chemical Solution Deposition of Functional Oxide Thin Films*, Springer, New York, 2013, ISBN 978-3-211-99311-8.
[8]. Vasu K., Ghanashyam Krishna M., K. Padmanabhan A., *Conductive-atomic force microscopy study of local electron transport in nanostructured titanium nitride thin films*, Thin Solid Films, 519, p. 7702-7706, 2011.
[9]. Sun B., Sirringhaus H., *Solution-Processed Zinc Oxide Field-Effect Transistors Based on Self-Assembly of Colloidal Nanorods*, Nano Letters, 2005, Vol. 5, No. 12, p. 2408-2413.
[10]. Costenaro D., Carniato F., Gatti G., Marchesea L., Bisio C., *Preparation of Luminescent ZnO Nanoparticles Modified with Aminopropyltriethoxy Silane for Optoelectronic Applications*, New J. Chem. 2013, 37, 2103.
[11]. Vinodkumar R. *et. al.*, *Structural, spectroscopic and electrical studies of nanostructured porous ZnO thin films prepared by pulsed laser deposition*, Spectrochimica Acta Part A: Molecular and Biomolecular Spectroscopy, 118, p. 724-732, 2014.

THE ANNALS OF "DUNAREA DE JOS" UNIVERSITY OF GALATI
FASCICLE IX. METALLURGY AND MATERIALS SCIENCE
Nº. 2 - 2015, ISSN 1453 – 083X

THE ELECTROMAGNETIC PROPRIETIES OF HYBRID COMPOSITES

I. G. Bîrsan[b], Marina Bunea[a], G. Mihu, A. Cîrciumaru[b,*]
[a] "Dunărea de Jos" University of Galati, Faculty of Mechanical Engineering, 47 Domnească Street, RO-800008, Galati, Romania
[b] "Dunărea de Jos" University of Galati, Border Faculty of Humanities, Economics and Engineering, 47 Domnească Street, RO-800008, Galati, Romania
e-mail: adrian.circiumaru@ugal.ro

ABSTRACT

This research investigates the electromagnetic behaviour of hybrid composites with heterogeneous epoxy matrix. The hybrid composites were formed by the wet lay-up method and were made of three types of simple plain fabrics as sheets. In order to improve the electrical and magnetic properties of hybrid materials and to modify the basic properties of epoxy resin, fillers such as carbon black and ferrite were used. Analysing the electromagnetic properties of the formed hybrid composites, it was observed that the composites with outer layers made of carbon fabric sheets exhibited higher dielectric permittivity and electrical conductivity in comparison with other materials. The magnetic permeability of the studied composites showed negative values within the whole range of frequencies, but the materials with aramid fabric in outer layers exhibited more negative values of magnetic constants.

KEYWORDS: electrical conductivity, magnetic permeability, hybrid composites, filled matrix

1. Introduction

The advancement in fibres reinforced composites leads to the achievement of materials with unusual electromagnetic behaviour. Many studies have shown that the polymeric composites are electrical non-conductive, but their electrical properties can be improved by using fillers such as carbon nanotubes (CNT), carbon black, graphite, graphene, short carbon fibres and their magnetic properties can be enhanced by using barium ferrite (BaFe). It is necessary to know that the use of fillers in the structure of composites may improve the electrical and magnetic properties. Also, they can affect the mechanical properties, and this is why it must be considered the weight fraction of the used fillers, because it should not exceed 30-40% of the matrix, due to its different arrangement directions and its multiple geometric patterns which are formed [1].

Short fibres are used not only to improve the mechanical properties, but also to improve the electrical properties [2]. Carbon nano-fibres (CNFs) can effectively improve the electrical conductivity of CNFs/epoxy nano-composites, which can form the conductive path at a low content, and the threshold of CNFs/epoxy nano-composites ranges between 0.1% and 0.2% weight ratios [3].

Markov *et al.* [4] studied the influence of carbon black and short carbon fibres on electrical and mechanical properties of unidirectional glass fibre reinforced polyethylene. An anisotropic electrical conductivity was determined within the range of percolation threshold. Also, Wong *et al.* [5] investigated the influence of recycled carbon fibres on the development of electromagnetic shielding.

Witchman *et al.* [6] studied the influence of carbon nanotubes, fumed silica and carbon black on the mechanical and electrical properties of glass fibre reinforced epoxy composites. They showed that the electrical conductivity could be included into the FRPs by using only very small amounts (0.3%) of carbon nanotubes without any decreasing of the mechanical properties. The nanoparticles (fumed silica and carbon black) had improved the mechanical properties and had exhibited an adjustable electrical conductivity.

In this paper the electrical and magnetic properties of six fabric reinforced composites with heterogeneous epoxy matrix were analysed. The type of fabric sheets in the outer layers of hybrid

composites affected the electromagnetic parameters. The negative magnetic permeability values of the studied hybrid composites were obtained. The negative magnetic permeability is identified by many scientists in the case of meta-materials, which are artificial materials with simultaneously negative dielectric permittivity and negative magnetic permeability at the same frequency, leading to negative refraction index, or one of these parameters can have a negative value and the other a positive value. When these parameters have different signs, the electromagnetic wave cannot spread [7-10].

2. Materials

For this research, six different hybrid reinforced composite materials with heterogeneous epoxy matrix were formed. The reinforcement was made of three types of fibre fabrics, namely: carbon fibre fabric designated C, aramid fibre fabric designated K and glass fibre fabric designated G. The orientation of layers was different as it may be noticed in Table 1. Each composite was reinforced with 17 layers of the above mentioned fabrics excepting the medial layer that was made of a hybrid fabric.

The hybrid fabric was obtained by replacing each second yarn of aramid fibres on the fill of a mixed simple type fabric with 2:1 (carbon:aramid) yarns on warp and 1:2 (carbon:aramid) yarns on the fill with a glass fibres yarn of 200 tex in which a tinned cooper wire of 0.2 mm diameter had been inserted.

The three types of fabrics were symmetrically distributed relatively to the medial layer but based on their orientation they displayed an anti-symmetrical balanced structure.

The matrix of materials was made of epoxy system EPIPHEN RE 4020 - DE 4020 (Bostik). Epoxy resins exhibit superior mechanical and electrical properties in comparison with other resins [11]. The heterogeneous epoxy matrix was formed by modifying the epoxy system with 10% wr of starch, 10% wr of aramid powder and, 10% wr of carbon black (MF1) and 10% wr starch, 10% wr carbon black and, 10% wr ferrite (MF2). The MF1 filled matrix was used for reinforcement layers 1 to 5 and 13 to 17, while MF2 filled matrix was used for reinforcement layers 6 to 12.

These fillers were used to improve the electromagnetic properties of the studied materials. So, the ferrite was used to enhance the magnetic properties, but the particle size, the filler concentration and the mutual orientation of the ferrite particles in the matrix affect the value of these properties [12]. That is why the potato starch was used, to prevent the sedimentation of the other fillers.

The carbon black was used for improving the electrical properties and aramid powder was used for improving the impact properties that will be discussed in another paper.

All the hybrid composite materials were formed by the wet lay-up method with each sheet of fabric imbued with correspondent pre-polymer mixture and then placed into a mould. The microscopical images of the transversal surfaces of materials are presented in Fig. 1.

Table 1. *The layers configuration of hybrid reinforced composite materials with heterogeneous matrix*

Layers	Materials					
	M1F	**M2F**	**M3F**	**M4F**	**M5F**	**M6F**
01	30_K	15_K	30_K	30_G	45_C	0_C
02	-30_K	30_K	15_K	-30_C	-30_C	-30_C
03	45_C	-15_C	0_C	0_K	15_G	45_C
04	0_C	-30_C	45_G	45_G	30_G	0_K
05	45_C	45_G	-30_G	30_C	-30_C	-30_K
06	0_C	15_C	-15_C	15_K	0_C	45_K
07	15_K	30_K	30_K	-30_K	30_G	30_G
08	30_K	45_K	45_K	30_G	45_G	45_G
09	90_M	90_M	90_M	90_M	90_M	90_M
10	-30_K	45_K	45_K	30_G	45_G	45_G
11	-15_K	-30_K	-30_K	45_K	-30_G	-30_G
12	0_C	-15_C	15_C	-15_K	0_C	45_K
13	45_C	45_G	30_G	-30_C	30_C	30_K
14	0_C	30_C	45_G	45_G	-30_G	0_K
15	45_C	15_C	0_C	0_K	-15_G	45_C
16	30_K	-30_K	-15_K	30_C	30_C	-30_C
17	-30_K	-15_K	-30_K	30_G	45_C	0_C

Carbon fabric: 4×4 plain weave, 160 g/m^2.
Aramid fabric: 6.7×6.7 plain weave, 173 g/m^2.
Glass fabric: 12×12 plain weave, 163 g/m^2.

3. Experimental method

To determine the electromagnetic properties, such as dielectric permittivity, electrical conductivity and magnetic permeability of hybrid composites a digital LCR-meter Protek 9216A was used together with the measurement cell, according to [13]. Both bulk and surface measurements were performed at the five built-in frequencies of LCR-meter in five points on each formed material.

The calculation of dielectric permittivity, electrical conductivity, electrical resistivity and magnetic permeability of hybrid composites was done by means of the formulas given in [14].

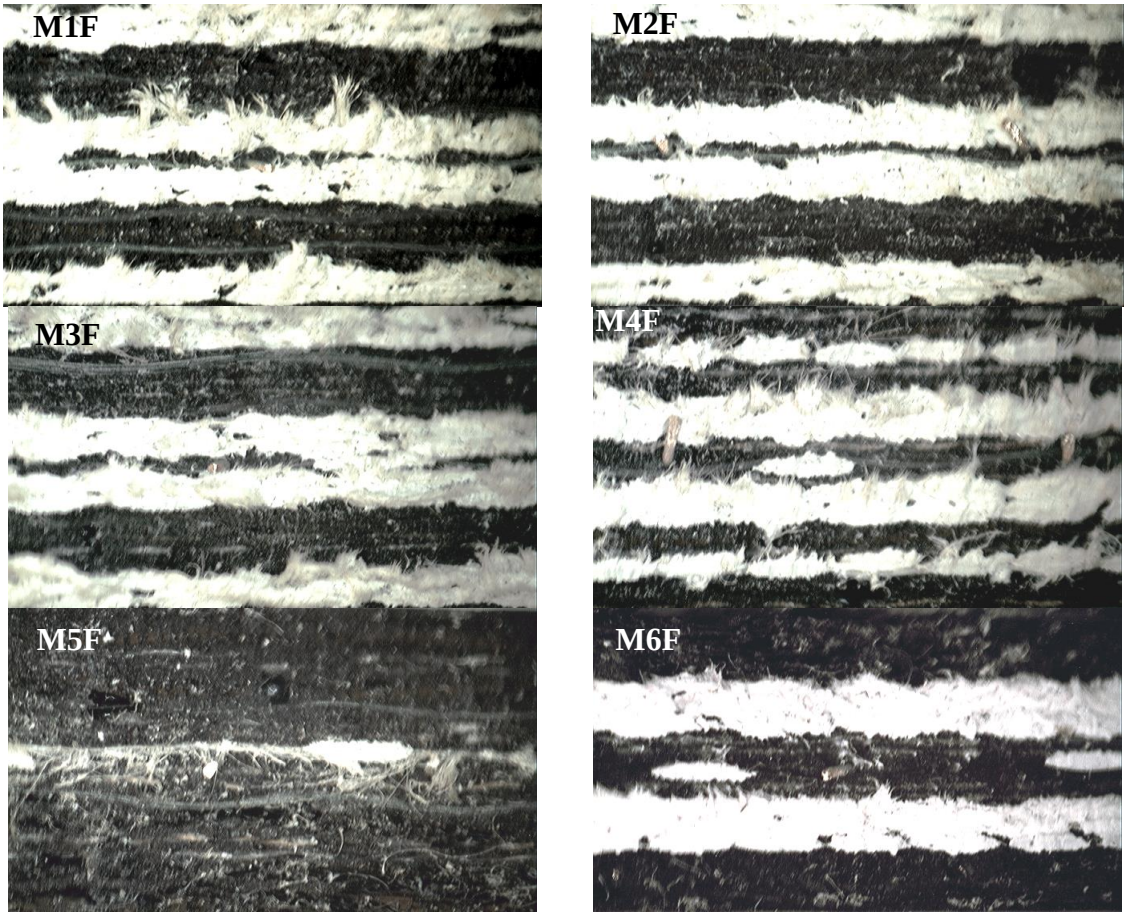

Fig. 1. *The microscopical images of hybrid laminates transversal surfaces*

4. Results and discussion

Generally, the electrical properties of the fibre reinforced composite materials depend on the moisture content, crystalline or amorphous component present, presence of impurities, etc. [15, 16]. In Fig. 2 are plotted the values of surface and bulk dielectric permittivity constants of the materials. The hybrid composite materials with outer layers made of carbon fabric sheets exhibit higher dielectric permittivity values than other hybrid composite materials, whose outer layers are made of aramid and glass fabrics sheets, but these values decrease when increasing frequencies.

The glass fabric reinforced composites and aramid fabric reinforced composites are used as insulators. In this regard, M5F hybrid composite material exhibits the highest value of bulk dielectric permittivity and M6F hybrid composite material exhibits a similar value of bulk dielectric permittivity as those of other hybrid materials, whose values do not vary with frequency.

In Fig. 3 are plotted the values of the electrical conductivity of hybrid composite materials. As it can be seen, the electrical conductivity of materials increased when increasing frequency till the frequency rose to 1 kHz, while the hybrid materials with outer layers made of carbon fabric sheets exhibited higher values of electrical conductivity, but at 10 kHz and 100 kHz these values became almost equal to the values of other studied hybrid materials.

The surface and bulk magnetic permeability constants of all hybrid composites showed negative values on the entire frequency domain (Fig. 4).

All the magnetic values became less negative when increasing frequency. The magnetic permeability of hybrid composites with outer layers made of aramid fabric sheets showed more negative values and the glass fabric outer layers composite exhibited intermediate values of magnetic constants.

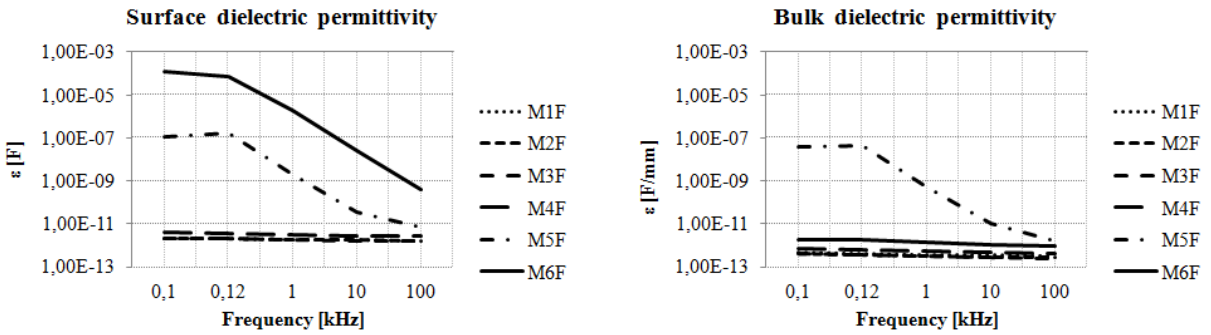

Fig. 2. *The dielectric permittivity of the hybrid composite materials*

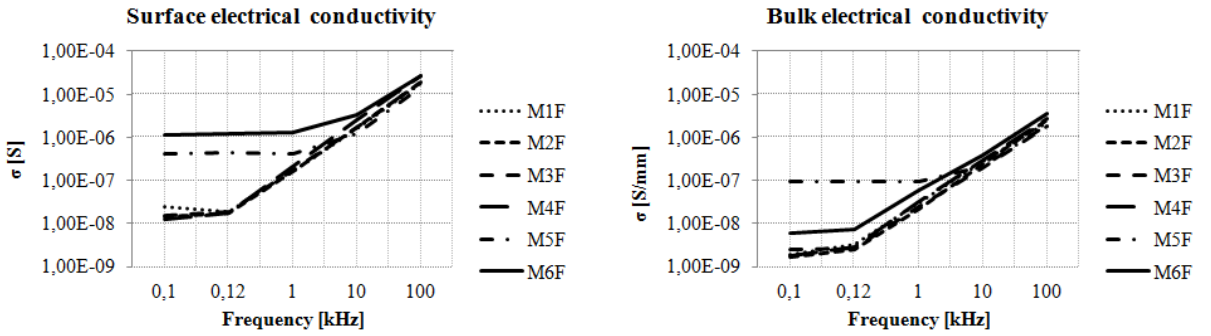

Fig. 3. *The electrical conductivity of the hybrid composite materials*

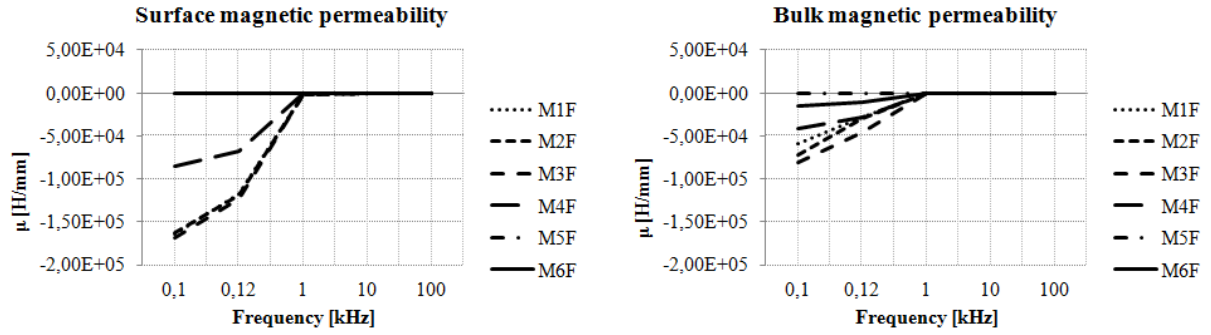

Fig. 4. *The magnetic permeability of the hybrid composite materials*

5. Conclusions

The electrical and magnetic parameters of hybrid composites were measured by standard electrical method applied for plates in electric and electronic engineering and the electrical and magnetic constants were calculated. Analysing the electromagnetic behaviour of the studied hybrid composites, the following conclusions can be drawn:

- The hybrid composites with outer layers made of carbon fabric sheets exhibit the highest dielectric permittivity, which decreases when increasing frequency.
- The highest surface electrical conductivity at 0.1-1 kHz range of frequencies was exhibited by M5F hybrid composite due to its outer layers made of more carbon fabric sheets. The highest bulk electrical conductivity at the same range of frequencies was exhibited by M5F hybrid composite because its structure does not contain aramid fabric sheets. However, at 10 kHz and 100 kHz frequencies, the values of electrical conductivity of these hybrid materials become similar with the values of other hybrid materials studied in this research.
- All the hybrid composites exhibit negative magnetic parameters within the whole range of frequencies.

● The values of magnetic permeability of hybrid composites with outer layers made of aramid fabric sheets were more negative than those of other hybrid composites.

Acknowledgements

The work has been funded by the Sectoral Operational Programme Human Resources Development 2007-2013 of the Ministry of European Funds through the Financial Agreement POSDRU/159/1.5/S/132397.

References

[1]. Xanthos M., *Functional Fillers for Plastics: Second, updated and enlarged edition*, WILEY-VCH Verlag GmbH & Co. KGaA, ISBN: 978-3-527-32361-6, Weinheim, Germany, 2010.
[2]. Van der Vegt A. K., *From polymers to plastics*, DUP Blue Print, The Netherlands, 2002.
[3]. Qilin M., Jihui W., Fuling W., Zhixiong H., Xiaolin Y., Tao W., *Conductive Behaviors of Carbon Nanofibers Reinforced Epoxy Composites*, Journal of Wuhan University of Technology-Mater. Sci. Ed., Vol. 23, No. 1, p. 139-142, 2008.
[4]. Markov Al., Fiedler B., Schulte K., *Electrical conductivity of carbon black / fibers filled glass-fibre-reinforced thermoplastic composites*, Composites: Part A 37, p. 1390-1395, 2006.
[5]. Wong K. H., Pickering S. J., Rudd C. D., *Recycled carbon fibre reinforced polymer composite for electromagnetic interference shielding*, Composites: Part A 41, p. 693-702, 2010.
[6]. Wichmann M. H. G., Sumfleth J., Gojny Fl. H., Quaresimin M., Fiedler B., Schulte K., *Glass-fibre-reinforced composites with enhanced mechanical and electrical properties – Benefits and limitations of a nanoparticle modified matrix*, Engineering Fracture Mechanics 73, p. 2346-2359, 2006.
[7]. Solymar L., Shamonina E., *Waves in Metamaterials*, Oxford University Press, ISBN 978-0-19-921533-1, 2009.
[8]. Ramakrishna S. A., *Physics of negative refractive index materials*, IOP Publishing Ltd, Rep. Prog. Phys. 68, p. 449-521, 2005.
[9]. Liu Y., Zhang X., *Metamaterials: a new frontier of science and technology*, Chem. Soc. Rev., 40, p. 2494-2507, 2011.
[10]. Wartak M. S., Tsakmakidis K. L., Hess O., *Introduction to Metamaterials*, Physics in Canada, Vol. 67, No. 1, p. 30-34, Jan.-Mar. 2011.
[11]. Ellis B., *Chemistry and Technology of Epoxy Resin*, 1st edition, ISBN 0-7514-0092-5, Chapman & Hall, 1993.
[12]. Valko L., Bucek P., Dosoudil R., Usakova M., *Magnetic properties of ferrite-polymer composites*, Journal of Electrical Engineering, Vol. 54, No. 3-4, p. 100-103, 2003.
[13]. Misra D. K., *Permittivity measurement*, Webster, J. G. (ed.), Measurements, Instrumentations, and Sensors, CRC Press, 46, 1999.
[14]. Cîrciumaru A., *Proiectarea, formarea și caracterizarea materialelor compozite cu matrice polimerică*, Editura Europlus, Galați, ISBN 978-606-628-060-0, 2013.
[15]. Abd Alradha R. M., *Electrical Resistivity Study for Unsaturated Polyester Reinforcement Glass Fiber*, International Journal of Current Engineering and Technology Vol. 4, No. 2, p. 890-892, 2004.
[16]. Patania D., Singh D., *A review on electrical properties of fiber reinforced polymer composites*, International Journal of Theoretical & Applied Sciences, 1 (2), p. 34-37, 2009.

THE ANNALS OF "DUNAREA DE JOS" UNIVERSITY OF GALATI
FASCICLE IX. METALLURGY AND MATERIALS SCIENCE
Nº. 2 - 2015, ISSN 1453 – 083X

DETERMINATION OF GLASS TRANSITION TEMPERATURE FOR POLYESTER / GRAPHENE OXIDE AND POLYESTER / GRAPHITE COMPOSITE BY TMA AND DSC

M. Bastiurea[1], M. S. Bastiurea[1], G. Andrei[1], M. Murarescu[2], D. Dumitru[2]
"Dunarea de Jos" University of Galati, Romania
[1] Faculty of Engineering
[2] Faculty of Sciences and Environment
e-mail: marian_bastiurea@yahoo.com

ABSTRACT

The influences of oxide grapheme and grapheme in thermosetting polymer composites are complex and they very much depend on the chemical bonds formed between the additives and the polymer matrix. This study has used polyester as polymeric matrix and oxide grapheme and graphite as additives. Determination of glass transition temperature (Tg) is important for practical uses of polyester composites due to the changes of characteristics triggered by transition, thus the polymer passes from elastic to plastic state. In order to determine the Tg we used TMA, DSC, DMA tests. The differences in determined Tg values for the same composite are due to different measurements as resulted from each test.

KEYWORDS: polyester, graphene oxide, graphite, Tg, TMA, DSC, DMA

1. Introduction

The glass transition temperature (Tg), of amorphous polyester is one of the most important parameters for industrial applications. At temperatures above Tg, polyester behaves rubbery, below the Tg, polyester is described as a glass state. The rubbery state of polyester may be described as the situations in which the entanglements restricted the motion of polyester chains, will be resolved and polyester will behave like viscous fluid. Polyester is one of the most used rigid polymer raisins; it is mainly used as matrix for composites used in almost all industries due to excellent mechanical properties, improved processability, good thermal, electrical, chemical and dimensional stabilities. Polymer matrix composites with grapheme oxide or graphite will improve mechanic and thermal characteristics of polyester [1-5]. Graphite is an allotropic form of carbon, which is naturally abundant. In graphite, carbon atoms are covalently bonded in hexagonal manner, forming individual graphene sheets, and these sheets are bound together by Van der Waals forces. Graphite has been used in many industrial applications such as lubricant and additives in composite. It has received attention lately due to its superior in-plane properties. There are two types of graphene structures mainly used as additives in composites namely, the graphene oxide and reduced graphenes. Graphene oxide consist of oxygen based groups such as carbonyl, hydroxile or oxygen, these being bonded to the graphenes [6] in order to make graphene oxide more functional, as well as their better dispersion into the polymers, more methods have been discovered/found. [7-9]. The difficulty in treating the glass transition is caused by almost undetectable changes in the structure despite of qualitative changes in characteristic and extremely large change in the time scale [10]. For that reason, it used to determine Tg, different test and physics parameters. The values of Tg depends on functional groups of the polymer, as carbonyl, carboxyl [11].

2. Methods and materials

2.1. Thermo-mechanical analysis (TMA)

Thermomechanical analysis (TMA) is a method used in order to determine the size changes of the material, according to the temperature. This change can be used to determine the coefficient of linear thermal expansion and temperature of glass transition. For testing we used TMA/SDTA 840 device from METTLER TOLEDO. The samples were measured before testing. A 0.02 N force has been applied on the

sample, which was necessary in order to keep the sample still during heating. The thickness of the sample was 4 mm. There have been tested five samples for each concentration. The TMA test only determines the beginning the glass transition temperature, which takes place during a temperature interval. The test was made according to ASTM E831 standard.

2.2. Differential Scanning Calorimetry (DSC)

Differential Scanning Calorimetry (DSC) is a method used in order to determine heat quantity needed by the tested material in order to change its temperature. Measurements are made according to a reference material. Thus, the specific heat and the glass transition temperature of the material can be determined. Tester DSC1 Mettler Toledo was used for testing.

The tube mass was measured by weighing them on the analytic scales *Mettler Toledo AB204—S/FACT* 0.1mg precision. The testing process consists of the following steps: 3 min maintaining at 30 ºC, heat speed 10 ºC/min up to 190 ºC, maintaining for 3 min at 190 ºC, cold speed 10 ºC/min up to 30 ºC, maintaining for 3 min at 30 ºC. For each concentration there have been tested five samples. DSC test determines both the temperature beginning of the glass transition on the curve temperature or "midpoint". In order to compare them, only the the beginning of the glass transition temperature will be used. The tests have been made according to ASTM E 1269 standard.

2.3. Materials

The analysis has been made on non-saturated polyester raisin samples added at five concentrations: 0.02 wt.%; 0.04 wt.%; 0.06 wt.%; 0.08 wt.%; 0.10 wt.% by using two additives: graphene oxide and graphite. In a 500 ml beaker was placed graphite (Graphite Crystalline PMM 11/99.9 KOH-I-NOOR GRAFI s.r.o Netolice, CZ). Then it was added perchloric acid 70%, (Merck) and solutions was mixed in a magnetic stirring for 30 minutes (2500 rpm). After that the mixture was cooled in ice bath. When solution reached 25 ºC potassium permanganate (achieved from Fluka) was added. This reaction is highly exothermic, and for that the permanganate was incorporated in four steps. The temperature of solution during the process increased from 25 ºC to 35 ºC. In order to maintain the temperature below 35 ºC, the beaker was introduced in ice bath. All reaction time was 20 hours. In this cooled solution was introduced the hydrogen peroxide 30% in ten steps, during 4h. When reaction is completed (CO_2 emission ceased), the final suspension was spinned at 19,000 rpm. The clear phase was removed, the solid phase was washed in distilled water in 5 stages; the amount of distilled water was 2500 ml. Aqueous reached the pH value of 6.5 (identical with distilled water one). Aqueous was mixed twice using absolute ethanol (volume of 700 ml) and was spinned. The residue obtained was introduced into a crystallizer vessel as a thin film and dried in an oven at 115 ºC for 12 h.

First step to achieved polyester/graphite and polyester/graphene oxide nanocomposite respectively, it was to introduce the proper quantities of graphite, graphene oxide into polyester resin, achieving finally a total amount of 100 g of nanocomposite. Following the concentrations fixed for the experiment, it was weighed at the analytical balance % grams of graphite and graphene oxide respectively and it was placed in a mortar. A dry grinding stage was set for 60 minutes. After that it was introduced 5-6 g of polyester resin and followed a "wet grinding" stage for another 60 minutes. The polyester composite was obtained by a "washing" procedure, using small quantities of resin until the final amount of 100 g. Polyester composite was introduced in a 300 ml stirred tank and it was stirred for 2h using a magnetic stirrer (2500 rpm). After this step, the dispersion of the particles into the polyester resin by sonication was split in two stages of 15 minutes. In order to maintain the temperature under control during the reaction process at 45 ºC, the mixture was placed in an ice bath. The composite was then degassed under vacuum (4-5 torr) for 4 minute. In next step, the catalyst (2% PMEK) was introduced under continuously stirring. This step was followed by a mechanical homogenization for another 12 minute. The composite was poured into rubber molds. The solidification time was 77 minutes. After two hours the nanocomposite was extracted from the mold and placed in the oven to complete the reaction at 70 ºC for 7 h.

3. Results

3.1. Glass transition temperature determined by TMA

Determination of Tg by using TMA method is made on the samples heating curve as can be seen in Figure 1.

Figure 1 shows the composite variation of samples dimension versus the temperature for the polyester 0.02 wt.% graphene oxide composite. It has been noticed an increase of Tg for all the concentrations tested. The biggest values have been obtained for polyester+0.1 wt.% graphene oxide composite and polyester+0.1 wt.% graphite. The

values obtained are showed in Table 1. For all the concentrations studied the maximum values have been obtained for polyester/graphene oxide composites.

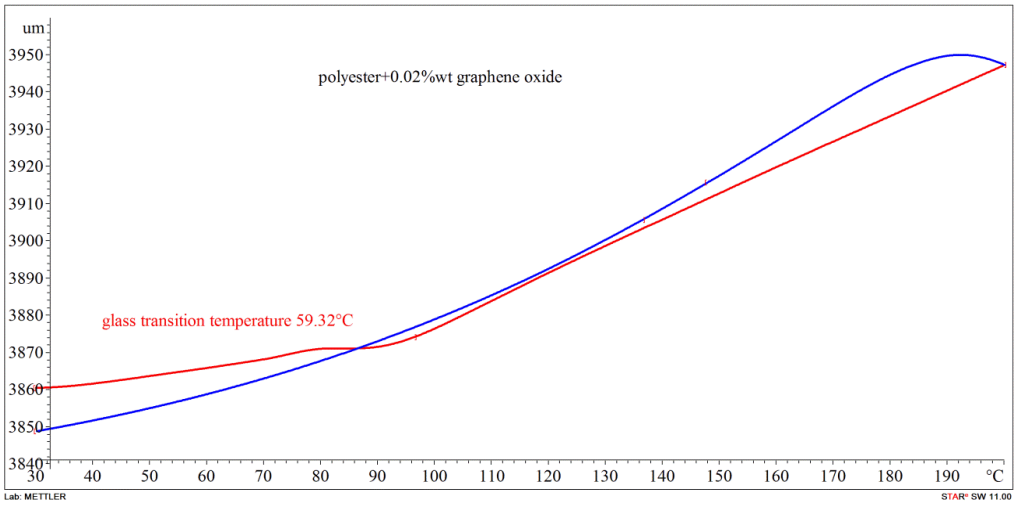

Fig. 1. *Change length vs temperature for polyester+0.02 wt.% graphene oxide*

3.2. Glass transitions temperature determined by DSC

The test DSC can determine Tg both on the heating and the cooling stage. In order to compare the values obtained by this test with the values obtained by the TMA tests, only the value determined on the heating stage of heat flow or specific heat will be used. The best Tg values have been obtained for polyester+0.1 wt.% graphene oxide composites and polyester+0.1 wt.% graphite composites. For all the concentrations studied, the maximum values have been obtained in polyester/graphene oxide composites. Fig. 2 shows the thermal curve flux according to the temperature for the polyester+0.02 wt.% graphene oxide composites on which the glass transition temperature has been determined both in the heating and cooling process. The differences between Tg determined on heating stage and cooling stage could be determined by the generates gases such as CO, CO_2, H_2O in heating stage [12, 13]. Table 1 shows us a small difference between Tg determined by DSC and TMA test.

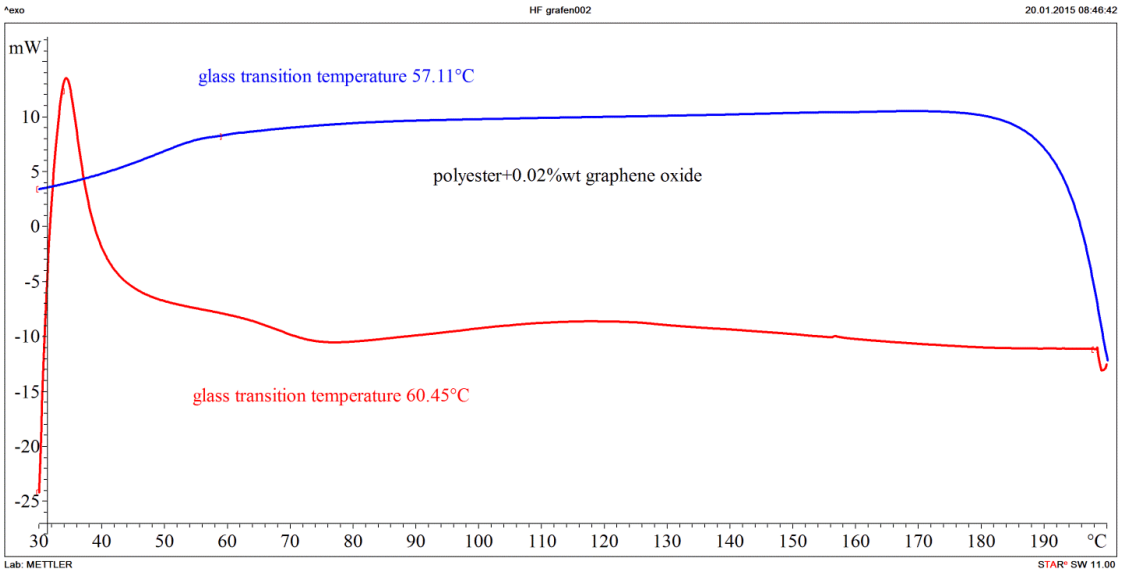

Fig. 2. *Tg for polyester+0.02 wt.% graphene oxide determined by DSC*

Table 1. *Glass transition temperature determined by DSC and TMA tests*

	Tg	
	DSC	TMA
	[^{0}C]	[^{0}C]
polyester	55.27	54.14
polyester+0.02%wt graphene oxide	60.45	59.32
polyester+0.04%wt graphene oxide	63.45	61.86
polyester+0.06%wt graphene oxide	65.98	63.25
polyester+0.08%wt graphene oxide	68.41	65
polyester+0.1%wt graphene oxide	68.98	65.8
polyester+0.02%wt graphite	58.02	56.92
polyester+0.04%wt graphite	59.95	57.9
polyester+0.06%wt graphite	61.83	59.26
polyester+0.08%wt graphite	63.05	60.45
polyester+0.1%wt graphite	65.06	63.45

Each test uses different physics parameters to determine glass transition temperature. In DSC test it used heat flow or specific heat curves and in TMA test it used change length curve. In the literature, have been reports differences of values up to 13 ºC. In both test the glass transition temperatures determined are on-set temperatures for glass transition, glass transitions extended over a range of temperature.

4. Conclusions

For all the composites studied, there has been observed a rise in glass transition temperature according to the rise of the additives concentration. The biggest increase in temperature has been observed for polyester/graphene oxide composites. This can be the result of both the nature and the number of the chemical bonds formed between the graphene oxide and the polyester matrix. In polyester/graphite composites only Van der Waals bonds appear while in polyester/graphen oxide composites there also appear hydrogen bonds which are much stronger than Van der Waals bonds. These are formed between esther groups from the polyester matrix with carbonyl and carboxyl groups which are formed during the process of obtaining the graphene oxide. The number of hydrogen bonds is smaller than Van der Waals bonds but much stronger than that. For the same concentration of additives, the number of chemical bonds formed between grapheme layer and the polyester matrix is much bigger than for polyester/graphite composites due to the graphite exfoliations into graphene layers, which have a specific surface much bigger comparing it with that of graphite they come/derive from. Graphene oxide involves molecular movement of the polyester chains during heating, thus the process of glass transition will start at a higher temperature comparing it with that of pure polyester. The differences obtained for the same concentrations, is due to different physical parameters used in DMA and TMA test.

Acknowledgement

The work has been funded by the Sectorial Operational Programme Human Resources Development 2007-2013 of the Ministry of European Funds through the Financial Agreement POSDRU/159/1.5/S/132397 ExcelDOC.

References

[1]. M. A. Rafiee, J. Rafiee, I. Srivastava, Z. Wang, H. Song, Z.-Z. Yu, N. Koratkar, *Fracture and fatigue in graphene nanocomposites*, Small Vol. 6(2), p. 179-183, 2010.

[2]. Y. F, M. A. Rafiee, J. Rafiee, Z. Z. Yu, N. Koratkar, *Dramatic increase in fatigue life in hierarchical graphene composites*, ACS Applied Materials Interfaces, Vol. 2(10), p. 2738-2743, 2010.

[3]. L. He, S. C. Tjong, *Low percolation threshold of graphene/polymer composites prepared by solvothermal reduction of graphene oxide in the polymer solution*, Nanoscale Research Letters, Vol. 8(1), p.132-139, 2013.

[4]. M. Monti, M. Rallini, D. Puglia, L. Peponi, L. Torre, J. M. Kenny, *Morphology and electrical properties of graphene–epoxy nanocomposites obtained by different solvent assisted processing methods*, Composites, Part A, Vol. 46, p.166-172, 2013.

[5]. S. Chandrasekaran, G. Faiella, L. A. S. A. Prado, F. Tölle, R. Mülhaupt, K. Schulte, *Thermally reduced graphene oxide acting as a trap for multiwall carbon nanotubes in bi-filler epoxy composites*, Composites, Part A, Vol. 49, p. 51-57, 2013.

[6]. D. R. Bortz, E. G. Heras, I. Martin-Gullon, *Impressive fatigue life and fracture toughness improvements in graphene oxide/epoxy composites*, Macromolecules, Vol. 45(1), p. 238-245, 2012.

[7]. M. Fang, Z. Zhang, J. Li, H. Zhang, H. Lu, Y. Yang, *Constructing hierarchically structured interphases for strong and tough epoxy nanocomposites by amineric graphene surfaces*, Journal of Material Chemistry, Vol. 20(43), p. 9635-43, 2010.

[8]. C. Bao, Y. Guo, L. Song, Y. Kan, X. Qian, Y. Hu, *In situ preparation of functionalized graphene oxide/epoxy nanocomposites with effective reinforcements*, Journal of Material Chemistry, Vol. 21(35), p. 13290–13298, 2011.

[9]. M. Cano, U. Khan, T. Sainsbury, A. O'Neill, Z. Wang, I. T. McGovern, K. M. Wolfgang, *Improving the mechanical properties of graphene oxide based materials by covalent attachment of polymer chains*, Carbon, Vol. 52, p. 363-371, 2013.

[10]. M. I. Ojovan, *Configurons: Thermodynamics parameters and symmetry changes at glass transition*, Entropy, Vol. 10, p 334-364, 2008.

[11]. M. Erber, A. Khalyavina, K.-J. Eichhorn, B. I. Voit Leibniz, *Variations in the glass transition temperature of polyester with special architectures confined in thin film*, Polymer, Vol. 51, p. 129-135, 2010.

[12]. Y. Wan, L. Gong, L. Tang, L. Wu, J. Jiang, *Mechanical properties of epoxy composites filled with silane-functionalized graphene oxide*, Composites A, Vol. 64, p. 79-89, 2014.

[13]. Bindu S. T. K., A. B. Nair, B. T. Abraham, P. M. S. Beegum, E. T. Thachil, *Mechanical properties of epoxy composites filled with silane-functionalized graphene oxide*, Polymer Vol. 55, p. 3614-3627, 2014.

THE ANNALS OF "DUNAREA DE JOS" UNIVERSITY OF GALATI
FASCICLE IX. METALLURGY AND MATERIALS SCIENCE
Nº. 2 - 2015, ISSN 1453 – 083X

APPLICATIONS BASED ON VARIABLE FREQUENCY ROTATING MAGNETIC FIELD. ELECTROMECHANICAL AGITATOR WITH DUAL DIRECTION

Ovidiu-Magdin Țanța[a,b,*], Mihaela Poienar[a], Ilie Nițan[a], Mihai Cenușă[a], Adrian-Neculai Romanescu[a]

[a] "Ștefan cel Mare" University of Suceava, Faculty of Electrical Engineering and Computer Science, 13 Universității Street, 720229, Suceava, Romania
[b] E.ON Distribuție România, 21 Piața Trandafirilor Street 540049, Târgu Mureș, România
*Corresponding author
e-mail: ovidiu.tanta@eon-romania.ro

ABSTRACT

This paper presents a series of experimental results obtained by studying the specific effects and phenomena of the rotating magnetic field. During the research, an interesting phenomenon, specific to the variable frequency rotating magnetic field, was noticed. Thus, a ferromagnetic metal ball placed in the rotating magnetic field, rotates in the field direction until it reaches a critical speed. If the speed of the magnetic field continues to increase, the ball reverses its rotation direction, even if the magnetic field direction remains the same. This has led to the development of stands and experimental installations including the dual direction electromechanical agitator described in this paper.

KEYWORDS: rotating magnetic field, fluid agitator, ferromagnetic balls

1. Introduction

The research on the behavior of magnetic liquids and ferromagnetic objects placed in rotating magnetic fields was based on the study of Kagan's effect. According to the magnetic liquid experiments carried out by R. Moscowitz and R. E. Rosensweig in 1967, it was shown that in a constantly rotating magnetic field, the magnetic liquid drive is given by the dipolar torque applied to each particle from the suspension composition. Later, in 1973, Kagan studied the phenomenon of ferrofluid spinning when it is exposed to the rotating magnetic field action. This reflects the magnetic liquid behavior which develops a rotative motion opposite to the magnetic field, in the context where electrically conductive liquids are spinning in the same direction as the field. Moreover, it was observed that all cylindrical dielectric bodies immersed in ferrofluid rotate in reverse direction as the rotating magnetic field [4].

Continuing the research in this area, the EMAD (Research Centre in Electrical Engines, Apparatus and Driving) researchers started a series of experiments based on the characteristic phenomena and the magnetic field applications.

2. Variable frequency rotating magnetic fields specific phenomena

In 2001, in a series of experiments, Professor Dorel Cernomazu accounts for the action of a steel magneto-active particle spread in water. The solution described had been submitted to a rotating magnetic field generated by the stator of a three-phase asynchronous motor. Initially, the spread analyzed tended to revolve in the same direction as the rotating magnetic field, whereupon, suddenly, it has started a reverse rotary flow [1].

In subsequent experiments, we used a ball from ferromagnetic material placed in a rotary magnetic field with rotational frequency varying between 0 and 6000 rot/min. It was noticed that the ferromagnetic ball, under the rotating magnetic field action, is spinning initially in the same direction as the field, and subsequently, by increasing rotational frequency, the ball direction is reversing. The reversal moment depends on the ball position related to the rotary magnetic field, ball dimensions and composition, the medium where it is placed and the field rotational speed. The experimental stand is shown in Figure 1.

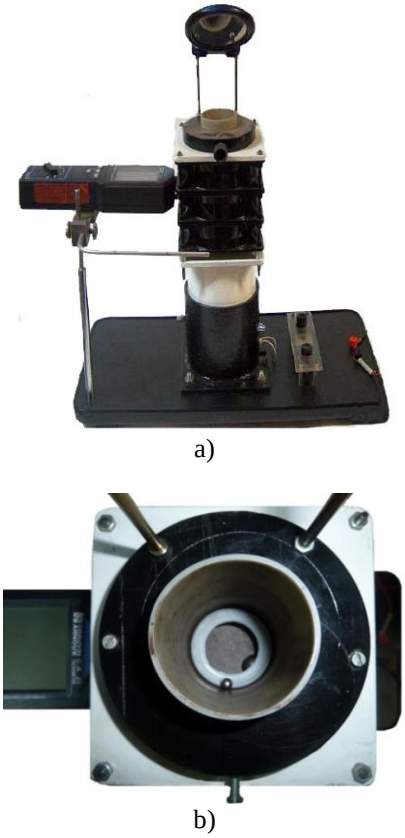

a)

b)

Fig. 1. *Stand for generation of variable frequency rotating magnetic field: a) side view; b) top view – insulating vessel detail*

The reproduction of the stand presented in the patent application [3], and the experiments described in the thesis [4], presented a number of interesting physical phenomena.

The device for variable frequency rotating magnetic field generation is actuated by a motor M2, supplied by an autotransformer AT, through an isolating transformer. Continuous adjustment of M2 motor supply voltage is achieved through the fact that the autotransformer potentiometer is actuated by a DC motor M1, supplied by a source AC/DC as it is shown in Figure 2.

During the first experiments, the ball placed in the rotating magnetic field had a different behavior. The results were influenced by many factors:

- the rotation speed of the shaft which drives the permanent magnets;
- the physical (size, weight) and magnetic properties of the ball;
- the position of the container and the position of the ball in the magnetic field lines;
- the viscosity of the environment in which the ball is placed (air, water, oil, glycerin).

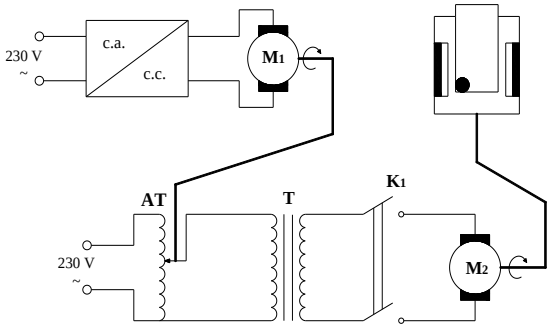

Fig. 2. *Feeding electrical diagram of the stand*

To obtain conclusive results, the variables influencing the test results were reduced and several sets of measurements were made with the following constants:

The ball used	Fe – 97.5%; Cr – 1.6% diameter: 11.1 mm weight: 5.6 g
The environment where the ball is placed	air
Growth rate of speed for motor M_2	constant
Ball placement	in the center of the permanent magnets

In order to verify the obtained results, three sets of measurements were performed for five different motor (M_1) supply voltages, thus identifying four critical points of the rotating magnetic field speed:

v_1 – the speed of the first reversal in direction of rotation - to the left;

v_2 – the maximum speed;

v_3 – the speed at which the ball remains in balance (at decreasing speed);

v_4 – the speed of the second reversal in direction of rotation (at decreasing speed) – to the right.

To illustrate the behavior of the ferromagnetic ball in time, we drew the graph shown in Figure 3, for the first group of values, for 14-volt supply voltage of the engine M_1.

U_{M1} = 14 V_{cc}		
Group I	Group II	Group III
v_1 = 596 [RPM]	v_1 = 614 [RPM]	v_1 = 622 [RPM]
v_2 = 3380 [RPM]	v_2 = 3392 [RPM]	v_2 = 3387 [RPM]
v_3 = 339 [RPM]	v_3 = 341 [RPM]	v_3 = 323 [RPM]
v_4 = 206 [RPM]	v_4 = 204 [RPM]	v_4 = 217 [RPM]

Analyzing the chart above, one can notice, in the diagram, five areas in which the ferromagnetic ball has different behaviors:

At increasing speed

0 – v_1 the ferromagnetic ball rotates clockwise (right), and when the speed reaches 595 RPM, it suddenly changes its direction of rotation to the left;

v_1 – v_2 the ball continues to rotate to the left up to the maximum speed of 3380 RPM;

At lowering speed

v_2 – v_3 the direction of rotation is kept to the left until it reaches a speed of 339 RPM;

v_3 – v_4 in this range, the ferromagnetic ball remains in balance;

v_4 – 0 at the speed of 206 RPM the second reversal occurs in the direction of rotation (to the right), the direction of motion was kept up to the speed of 0 RPM.

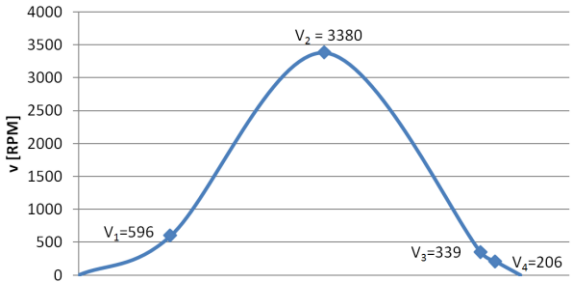

Fig. 3. *The rotational speed of the ball in time*

Based on the results obtained with one ball, with different diameters, materials and weights, placed in agents with different viscosities, a double-acting electromechanical stirrer was conceived, developed and tested. This stirrer is described in the following chapter.

3. Double-acting electromechanical stirrer

The double-acting electrochemical stirrer offers a number of advantages over the appliance described above, in that two stirring systems made of two ferromagnetic balls, with different diameters, isolated, placed under the same rotating magnetic field action, move along different tracks with different movement directions. In this manner an increased stirring effect was obtained, which reduces the time adequate for stirring and increases the device efficiency.

The double-acting electrochemical stirrer is made of an electrically insulating vessel 1 fitted in an electrically insulating support 2, in which a rotating assembly is placed. The rotating assembly consists of a ferromagnetic vessel as a glass 3, which presents on its inner surface two permanent magnets 4, fixed in diametrically opposite positions. The ferromagnetic vessel is driven in rotary flow by means of an arbor 5, of a DC motor 6 supplied from an auto-transformer with sliding contact. Two electrically insulating ferromagnetic balls 7 and 8 are placed inside the electrically insulating vessel 1. One of the balls is placed at the bottom of the vessel, and the other one on an annular chamber 9 made from an insulating material, bonded on the inner side of the vessel, under the fluid level.

The ferromagnetic balls 7 and 8, of different sizes, placed in different areas of the same variable frequency rotating magnetic field, are moving differently: one clockwise and the other one counterclockwise, within the vessel containing dielectric fluid. The balls direction of rotation depends on the relative position within the magnetic field and on the critical frequency at which the magnetic synchronous torque breaks for one of the balls [1].

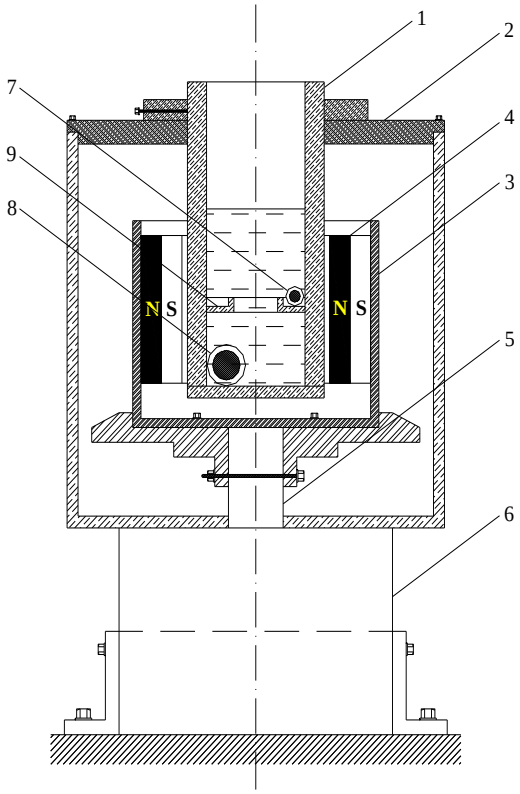

Fig. 4. *Double-acting electro-mechanical stirrer* [1]*: 1 - insulating vessel; 2 - insulating support; 3 - ferromagnetic support; 4 - permanent magnets; 5 - axle; 6 - DC motor; 7, 8 - ferromagnetic balls; 9 - annular chamfer*

4. Conclusions

The phenomenon studied, namely changing the ball direction of rotation when increasing the frequency, was named the CEUS effect by the researchers from the Electrotechnical Department of the University of Suceava.

The CEUS effect was the basis for the practical creation of fluids stirrers designed in a first variant with a single ferromagnetic ball with reversible direction of rotation when increasing the rotating magnetic field frequency.

An improved version of the stirrer is the one presented in the paper, characterized by the fact that the stirring effect is carried out by two balls placed in different planes, under the action of the same rotating magnetic field, which rotates in opposite directions.

The studied CEUS effect can be applied to achieve an electric motor with reversible direction of rotation at the change of frequency.

Another research direction detached from experiments is the study of a possible breaking torque generated by the leak flow over the ball bearing.

References

[1]. Graur A., Milici M. R., Milici L. D., Raţă M., Ţanţa O. M., Niţan I., Romaniuc I., Negru M. B., Cernomazu D., *Agitator electromecanic cu acţiune dublă*, Cerere de Brevet de Invenție nr. A/00330 din 29.04.2013, OSIM București.

[2]. Luca E., Călugăru Gh., Bădescu R., Cotae C., Bădescu V., *Ferofluidele şi aplicaţiile lor în industrie*, Bucureşti, Editura Tehnică, 1978.

[3]. Negru M. B., Cernomazu D., Mandici L., Minescu D., Ungureanu C., Savu E., Prodan C., *Agitator pentru fluide dielectrice.* Cerere de brevet de invenţie nr. a 2002 00412 A2. În B.O.P.I. nr. 2/2004, OSIM Bucureşti, pag. 19.

[4]. Negru M. B., *Contribuţii privind extinderea aplicaţiilor ferofluidelor şi a pulberilor feromagnetice în electrotehnică*. Teză de doctorat. Suceava: Universitatea „Ştefan cel Mare", Facultatea de Inginerie Electrică şi Ştiinţa Calculatoarelor, 2012.

THE ANNALS OF "DUNAREA DE JOS" UNIVERSITY OF GALATI
FASCICLE IX. METALLURGY AND MATERIALS SCIENCE
Nº. 2 - 2015, ISSN 1453 – 083X

ELECTRICAL PROPERTIES CHARACTERIZATION OF VINYL ESTER RESIN FILLED WITH CARBON NANOTUBES

Georgel Chirita[1], Gabriel Andrei[1], Iulian Gabriel Birsan[1], Dima Dumitru[2], Alina Cantaragiu[1]

[1] Faculty of Engineering, „Dunarea de Jos" University of Galati, Romania
[2] Faculty of Science and Environment, Department of Chemistry, Physics and Environment, „Dunarea de Jos" University of Galati, Romania
e-mail: george.chirita@ugal.ro

ABSTRACT

In this paper the authors have done a characterization of the electrical properties of vinyl ester based nanocomposites containing different percentages of carbon nanomaterials

The carbon fillers used in this study were single wall carbon nanotubes (SWCNTs) and multi-wall carbon nanotubes (MWCNTs). Three weight percentages (0.10, 0.15 and 0.20) of each type of carbon nanotubes used as filler were added into the thermoset polymer matrix of vinyl-ester, resulting six nanocomposite materials.

The electrical properties were measured with TeraOhm 5 kV tester for all six composite materials along with neat vinyl ester resin. The experimental results show that, by the addition of multi-wall carbon nanotubes filler to the vinyl-ester matrix, the electrical properties of the nanocomposite material thus obtained were significantly improved. The electrical percolation threshold concentration for multi-wall carbon nanotubes based vinyl ester nanocomposite was 0.20 wt.%.

KEYWORDS: electrical properties, vinyl-ester resin, conductivity, single wall carbon nanotubes, multi-wall carbon nanotubes

1. Introduction

Due to their superior overall thermal, electrical and mechanical properties, carbon nanotubes filled polymer composites have been of great interest for industrial and research community in the last years [1, 2]. Most polymers are characterized as insulators regarding the electrical properties. This became a challenge for the members of the research community who are studying the way of improving the electrical properties of polymers by adding different materials as reinforcement [3, 4].

Carbon nanotubes are among the most common fillers used in polymer composites that already proved their ability to enhance electrical conductivity, by several orders of magnitude at low percolation threshold [5-7]. Even with very low concentrations, carbon nanotubes are able to form conductive networks mainly due to their capability of high conductivity [8-10].

The main factors that are influencing the electrical conductivity are closely related to the type of polymer matrix. The enhancement of electrical conductivity of the polymer matrix can be achieved by the proper choice of the type of filler and its amount, along with a good dispersion of the filler in the matrix [9, 11].

2. Experimental research

Vinyl ester resin, type Polimal VE-11 M, was used as polymer matrix. Two types of carbon nanotubes: single wall carbon nanotubes (SWCNTs) and multi-wall carbon nanotubes (MWCNTs) provided by Cheap Tubes Inc. Company have been added to vinyl ester thermoset polymer. The main properties of the carbon nanotubes used in this study are presented in Table 1.

For each type of nanocomposite, three weight percentages of nanomaterials (0.10 wt.%, 0.15 wt.% and 0.20 wt.%) were used, obtaining six nanocomposite materials. The procedure of obtaining the nanocomposite materials using the vinyl ester resin as matrix and carbon nanotubes as

reinforcement was mechanical stirring. After the addition of carbon nanotubes into polymer matrix, the homogenization of the mixture has been performed by magnetic stirring at 600 rpm for one hour. After the mixture has been degassed using a vacuum pump, the methyl ethyl ketone peroxide has been added as catalyst, to start the polymerization process. The mixture was then homogenized at 600 rpm for 5 minutes and degassed again. The materials thus obtained have been molded and placed into an oven for 8 hours at 80 ºC to complete the polymerization process.

Table 1. *Properties of carbon nanotubes*

Carbon nanotubes type	Purity [daN/mm^2]	Density [daN/mm^2]	Outer diameter [nm]	Inner diameter [nm]	Length [µm]	Specific surface [m^2/g]
SWCNTs	>90	2.1	1-2	0.8-1.6	5-30	407
MWCNTs	>95	2.1	8-15	3-5	10-50	233

Three specimens with round cross-section shape with diameter of 5 mm and length of 150 mm have been obtained by this method for all of the composite materials studied. All the nanocomposite materials along with the neat vinyl ester resin were tested with TeraOhm 5 kV tester (Fig. 1). In Figure 2 there is a picture of the position of the tester electrodes during the measurement.

Fig. 1. *TeraOhm 5 kV tester*

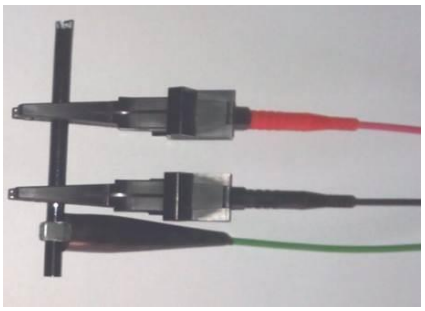

Fig. 2. *The position of electrodes during tests*

3. Results and discussion

The electrical conductivity results for the materials tested in this study are synthesized in the following graphs. The graphs show the calculated mean values of conductivity for the vinyl ester / CNTs composites.

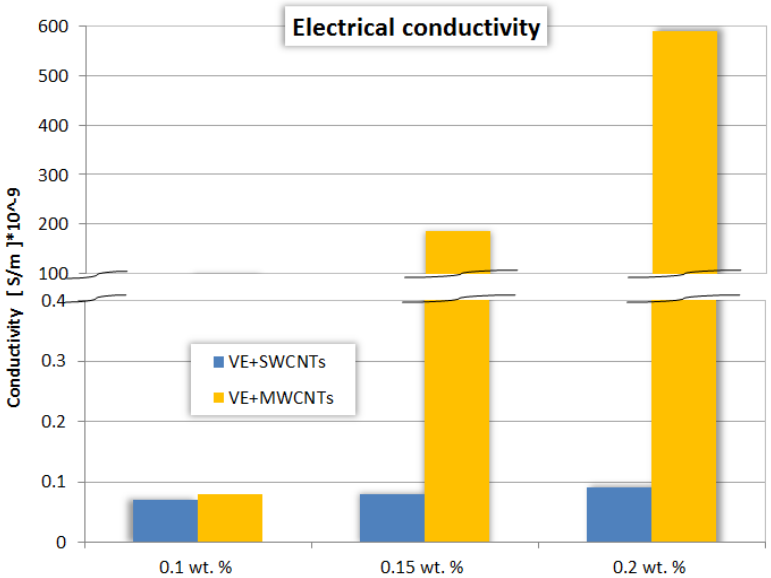

Fig. 3. *Electrical conductivity of vinyl ester/CNTs composites*

In Figure 3 the results of electrical conductivity for the two types of carbon filler based vinyl ester nanocomposite are represented together. For the 0.10 weight percentage of filler content, the conductivity is almost the same for the single and multi-wall carbon nanotubes / vinyl ester composite. In the case of 0.15 wt.% filler content, the value of the conductivity increases by about 200% for the multi-wall nanocomposite compared to the single wall / vinyl ester composite. The difference is of several orders of magnitude for 0.20 wt.% filler content.

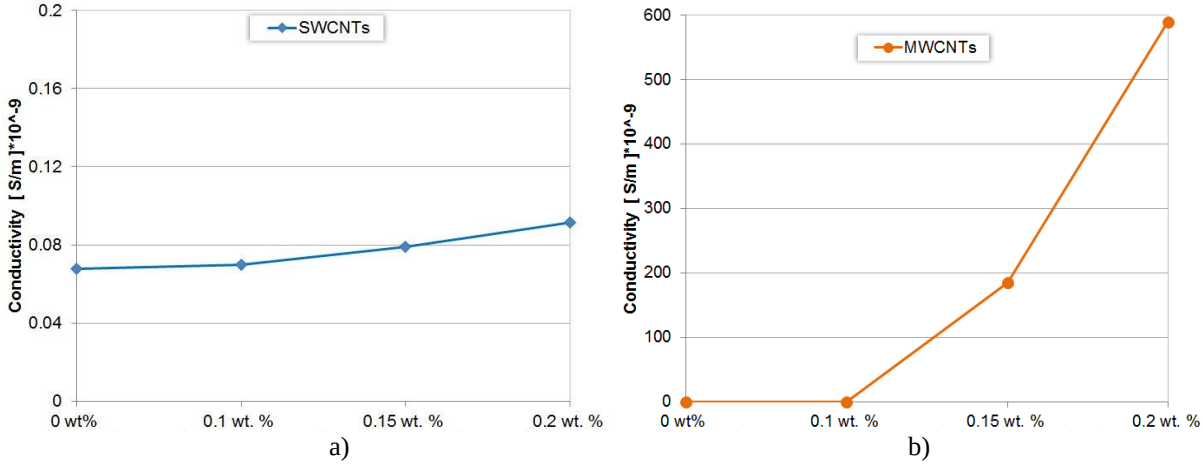

Fig. 4. *The tendency of electrical conductivity of nanocomposite of vinyl ester filled with different weight percentage (0 wt.%, 0.10 wt.%, 0.15 wt.% and 0.20 wt.%) of: a) single wall carbon nanotubes and b) multi-wall carbon nanotubes*

The filler content influence over the electrical properties for vinyl ester polymer matrix is represented in Figure 4. There is almost no difference between the 0.10 wt. % SWCNTs filler content nanocomposite and the neat vinyl ester (0 wt.% filler) electrical conductivity results. The addition of 0.15wt% and 0.20 wt.% of single wall carbon nanotube increases the electrical conductivity by approximately 14% and 27 % respectively. The increasing of electrical conductivity for addition of SWCNTs up to 0.20 wt.% content brings almost no changes in the insulating characteristics of the vinyl ester polymer matrix. In the case of multi-wall carbon nanotubes, an increase of 18% in electrical conductivity has been achieved for 0.10 wt.% of content, compared to 0 wt.% of filler. The enhancement of several orders of magnitude of electrical conductivity has been obtained for the above 0.15% weight percentage level content of multi-wall carbon nanotubes / vinyl ester composite.

4. Conclusions

Carbon nanotubes have already proved their capability as fillers in multiple multifunctional nanocomposites. In terms of electrical properties, an important factor is the percolation threshold linked closely by the dispersion of the nanoparticle in vinyl ester matrix.

According to the experimental results, multi-wall carbon nanotubes can be successfully used as fillers along with vinyl ester polymer as matrix. The observation of an improvement of electrical conductivity by several orders of magnitude at very low percolation threshold could be observed mainly on multi-wall carbon nanotubes for more than 0.15 wt.%. For single wall carbon nanotubes fillers, the results show a slight increase by 0.15 wt.% and 0.20 wt.%, leading to the conclusion that the percolation threshold for this case was not achieved. The electrical percolation threshold concentration was obtained for MWCNTs/vinyl ester for 0.20 wt. % content of carbon nanotubes.

Acknowledgement

The work of Georgel Chirita was supported by Project SOP HRD /159/1.5/S/138963 – PERFORM.

The work of Alina Cantaragiu has been funded by the Sectoral Operational Programme Human Resources Development 2007-2013 of the Ministry of European Funds through the Financial Agreement POSDRU/159/1.5/S/132397.

References

[1]. Gojny K. S., Wuchmann F. H. H. G., Fiedler B., *Influence of different carbon nanotubes on the mechanical properties of epoxy matrix composites*, Composites Science and Technology, p. 256-270, 2005.

[2]. Wernik J. M., Meguid S. A., *Recent Developments in Multifunctional Nanocomposites Using Carbon Nanotubes*, Appl. Mech. Rev., vol. 63, no. 5, 2010.
[3]. Choudhary V., Gupta A., *Polymer / Carbon Nanotube Nanocomposites*, 2001.
[4]. Paul D. R., Robeson L. M., *Polymer nanotechnology: Nanocomposites*, Polymer (Guildf), vol. 49, no. 15, p. 3187-3204, 2008.
[5]. Battisti A., Skordos A. A., Partridge I. K., *Percolation threshold of carbon nanotubes filled unsaturated polyesters*, Compos. Sci. Technol., vol. 70, no. 4, p. 633-637, Apr. 2010.
[6]. Spitalsky Z., Tasis D., Papagelis K., Galiotis C., *Carbon nanotube-polymer composites: Chemistry, processing, mechanical and electrical properties*, Prog. Polym. Sci., vol. 35, no. 3, p. 357-401, 2010.
[7]. Murarescu A. C. M., Dumitru D., Andrei G., *Influence of mwcnt dispersion on electric properties of nanocomposites with polyester matrix*, Ann. DAAM 2011, Proceeding 122 Int. DAAM Symp., vol. 22, no. 1, p. 925-926.
[8]. Tjong S. C., *Electrical and dielectric behavior of carbon nanotube-filled polymer composites*, Woodhead Publishing Limited, 2010.
[9]. Thostenson E. T., Ziaee S., Chou T. W., *Processing and electrical properties of carbon nanotube/vinyl ester nanocomposites*, Compos. Sci. Technol., vol. 69, no. 6, p. 801-804, 2009.
[10]. Ayatollahi M. R., Shadlou S., Shokrieh M. M., Chitsazzadeh M., *Effect of multi-walled carbon nanotube aspect ratio on mechanical and electrical properties of epoxy-based nanocomposites*, Polym. Test., vol. 30, no. 5, p. 548-556, 2011.
[11]. Yurdakul H., Seyhan A. T., Turan S., Tanoğlu M., Bauhofer W., Schulte K., *Electric field effects on CNTs/vinyl ester suspensions and the resulting electrical and thermal composite properties*, Compos. Sci. Technol., vol. 70, no. 14, p. 2102-2110, Nov. 2010.

THE ANNALS OF "DUNAREA DE JOS" UNIVERSITY OF GALATI
FASCICLE IX. METALLURGY AND MATERIALS SCIENCE
Nº. 2 - 2015, ISSN 1453 – 083X

THE USE OF ULTRASOUND IN THE TREATMENT PROCESS OF WASTEWATER. A REVIEW

Nicoleta MATEI*, Dan SCARPETE
"Dunarea de Jos" University of Galati, Romania
*Corresponding author
e-mail: nicoleta.ciobotaru@ugal.ro

ABSTRACT

In this paper, different types of ultrasound devices for the treatment process of wastewater are presented. The use of ultrasound in treatment processes is a method of perspective, an alternative to conventional methods. This technique is based on the cavitation phenomenon that occurs in liquids at ultrasonic irradiation and it is used to enhance or ensure the processes of heat and mass transfer. Some of the main advantages of using ultrasound, namely low consumption of additional material or energy, are presented in this paper. The categories of the ultrasonic transmitters distinguished on the basis of the principle underlying the generation of acoustic waves are described.

KEYWORDS: ultrasound, ultrasonic frequency, cavitation, wastewater treatment

1. Introduction

Ultrasound has proved to be effective in many processes common in the chemical industry, to improve dewatering and drying materials, to enhance filtration, to assist heat transfer, to degas liquids, to accelerate extraction processes, to degrade chemical contaminants in water and to enhance processes where diffusion takes place [1]. The reason why ultrasound power can produce chemical and physical effects is the phenomenon of acoustic cavitation [2]. In most liquids, cavitation is initiated by the excitation of preexisting microbubbles or other inhomogeneities in the fluid such as suspended particles or gas bubble nuclei [3]. Acoustic cavitation involves the formation and subsequent collapse of micro-bubbles from the acoustical wave induced compression / rarefaction [4].

The main driving mechanism in the degradation of pollutants using cavitation is the generation and subsequent attack of the free radicals though some of the reactions have been explained more suitably on the basis of hot-spot theory (localized generation of extreme conditions of temperature and pressure) [5].

Upon collapsing, each of the bubble would act as a hotspot, generating an unusual mechanism for high-energy chemical reactions to increase the temperature and pressure up to 5000 K and 500 atm, respectively, and cooling rate as fast as 10^9 K/s (Figure 1) [7, 8]. There are three potential reaction zones in sonochemistry [9, 10] i.e. inside the cavitation bubble, interfacial liquid region between cavitation bubbles and bulk liquid, and in the bulk solution.

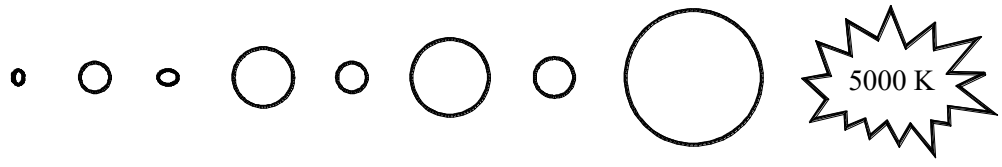

Fig. 1. *Cavitation bubble formation, growth and collapse* [6]

A representation of the pilot-scale pieces of equipment based on acoustic cavitations is shown in Figure 2 [11]. According to Gogate *et al.* (2004), the pieces of equipment with higher dissipation area give larger energy efficiency at similar levels of the supplied input energy. Also, the use of the equipment based on multiple frequencies (multiple transducers) has been reported to be more beneficial as compared to the equipment based on a single frequency [11].

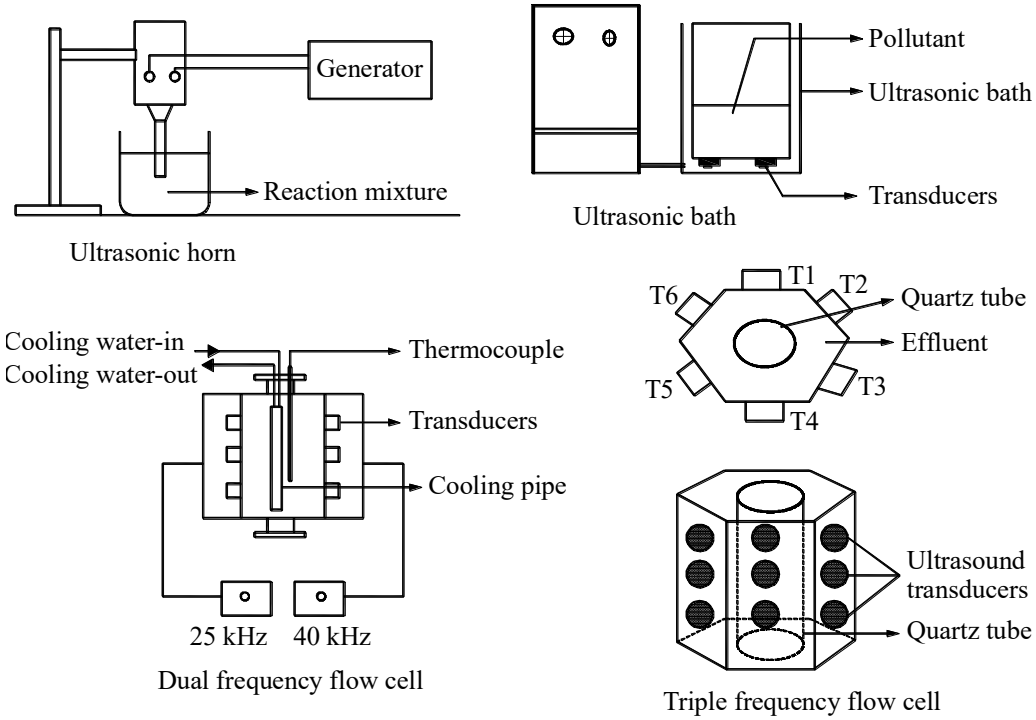

Fig. 2. *Schematic representation of the pieces of equipment based on acoustic cavitations* [11]

Nowadays, there are numerous constructive types of acoustic emitters, used in the treatment process of wastewater. The most often used emitters are the electromechanical ultrasound generators, relying on piezoelectricity [12-15] and magnetostriction phenomena [16-19]. There are also several applications of sonic mechanical generators [20-26]. Therefore, in this brief review some experimental achievements pertaining to the use of different ultrasonic generators for the treatment process of wastewater are presented.

2. Wastewater treatment by piezoelectric generators

The basis for the present-day generation of ultrasound was established as far back as 1880 with the discovery of the piezoelectric effect by the Curies [27, 28].

Certain materials will generate an electric charge when subjected to a mechanical stress, and change their dimensions when an electric field is applied across the materials. These are known respectively as the direct and the inverse piezoelectric effect [29]. The effect is observed in a variety of materials, such as quartz, dry bone, polyvinylindene fluoride [30].

The ultrasonic transducers based on the inverse piezoelectric effect rely on some materials response to the application of an electrical potential across opposite faces, with a small change in dimensions [28]. The operation of the piezoelectric generator is based on the usual property of a quartz crystal to deform in the electric field.

The transducer, typically an assembly comprised of a series of aluminum blocks or discs and electrically active piezoelectric elements in a "sandwich" configuration, acts as a mechanical transformer and "rings" much like a bell at its resonant frequency when suitably excited by the driving piezoelectric element [31]. The schematic representation of this type of transducer is shown in Figure 3, where: 1 - screw or pin settings (gripping) to transmitter; 2, 5 - blocks of metal (eg. aluminum, iron, brass); 3, 4 - piezoelectric ceramic plates (cylindrical, annular).

Considering that sonochemistry occurs in the close vicinity of the ultrasonic transducer, where the acoustic cavitation activity is relatively high [33], most applications of ultrasound are performed at

laboratory scale [34] by the use of ultrasonic transducers based on the inverse piezoelectric effect. From the reverse piezoelectric effect, the conversion of electrical to mechanical energy is carried out by the ultrasonic transducer, enabling the formation, growth and collapse of transitory cavitation bubbles in the sonified liquid [8, 35]. Important physical properties of a piezoelectric ceramic used as a driver for high amplitude oscillations are (1) a high Curie temperature, (2) a low dissipation factor, and (3) a high ''d'' constant. Low losses result in less heating of the ceramic, thus prolonging its lifetime of operation. The ''d'' constant is the ratio of the mechanical strain produced from an applied electromagnetic field [36].

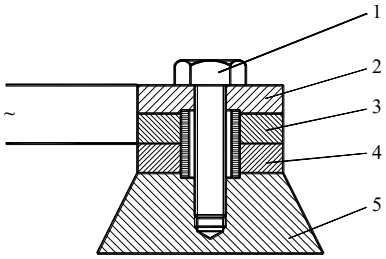

Fig. 3. *Construction of sandwich type piezoelectric ceramic transducer* [32]

The spreading area of the cavitational influence (the zone of developed cavitation) is limited by the damping of spread vibrations in viscous liquids or the change of wave resistance in cavitating liquid (practically up to the wave resistance in gas media). It limits the output of ultrasonic vibration energy from irradiator [14].

Some of the numerous experimental achievements using piezoelectric transducers are shown below. It should be noted that the majority of the work using this type of transducers is at a laboratory scale. Wenjun *et al.* [4] proposed a facility with ultrasonic transducer based on the piezoelectric effect. Experiments have allowed the removal of ammonia nitrogen and of two other organic pollutants (hydrazine and urea) from the simulated ammonia wastewater, up to 90%. The treatment conditions varied depending on the treatment type (intermittent or continuous), the pH variation and the treatment time. Matouq *et al.* used a piezoelectric transducer to remove pesticides from simulated wastewater. The experiment succeeded in removing the contaminant in a 70% ratio [37]. In paper [38], ultrasonic irradiation was carried out with a high-intensity ultrasonic probe system to remove chlorpyrifos and diazinon from the aqueous solution. The two pesticides were removed for up to 55%. Young K. studied the decomposition of monochlorphenols in paper [39] by sonication of 550 W output power and 20 kHz frequency. After 6 hours of reaction time, more than 80% of monochlorophenols were decomposed for experiments conducted in aqueous solution of pH 3 [39]. There should also be noted the promising results obtained for the formic acid degradation process using ultrasound proposed by [40]. The optimal operating volume was set at 300 ml, at different initial concentrations and using additional mechanical agitation, with a 40 W constant supplied power and 590 kHz constant frequency of irradiation.

3. Wastewater treatment by magnetostrictive generators

The operation of the magnetostrictive generator is based on the fact that some ferromagnetic substances change size at magnetization. If these substances are disposed in an alternating magnetic field, they will start to oscillate, in which case they can become sources of ultrasound. Like the piezoelectric generator, oscillating plates sizes need to be chosen so that their own frequency coincides with the frequency of the excitation (electric or magnetic frequency field), since they work in resonant mode. Magnetostriction occurs in most ferromagnetic materials, but among them the rare-earth alloy Terfenol–D ($Tb_{0.3}Dy_{0.7}Fe_{1.9}$) presents, at room temperature, the best compromise between a large magnetostrain and a low magnetic field [41]. Figure 4 shows the cross section of a prototypical Terfenol-D magnetostrictive transducer, in which the generated strains and forces are sufficiently large to prove advantageous in transducer design [42].

For magnetostrictive materials, due to the magnetomechanical effect, the change in magnetization along the stress direction can be produced by the stress, leading to the conversion of the mechanical energy into electrical energy [17, 43].

Magnetostrictive transducers are inherently more rugged [44] and better suited for industrial use [19].

The highest reasonable frequency achievable in a magnetostrictive transducer is around 30 kHz [45]. Magnetostrictive systems rely on the double conversion of electrical to magnetic energy and then from magnetic to mechanical to produce the sound wave. Magnetic systems are usually less than 50% efficient due to the energy lost in the heating of the coils and the effects of magnetic hysteresis. Additionally, the generators, even if well-tuned, are generally no more than 70% efficient [46].

Thoma *et al.* used a magnetostrictive system to degrade both benzene and toluene in a continuous stirred tank reactor [19]. They obtained good decontamination results by the use of 22-liter reaction vessel consisting of opposing diaphragm plates operating at 16 kHz and 20 kHz [19].

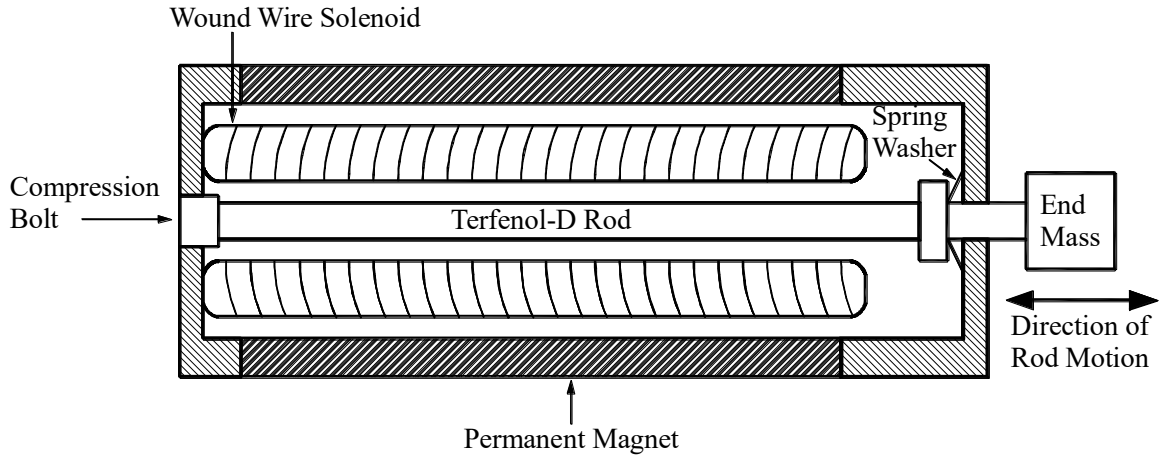

Fig. 4. *Cross section of a prototypical Terfenol-D magnetostrictive transducer* [42]

4. Wastewater treatment by mechanical generators

Mechanical transducers can be both gas driven and liquid driven [6]. The mechanical air-jet generator was proposed by Hartmann in order to treat liquids both by means of ultrasonic and bubbling [47]. The air-jet generators are mechanical devices with no moving parts that generate ultrasonic pressure waves with low frequency (10÷30 kHz), based on the nonstationary phenomena [48] occurring in the flow of high-speed jets of gas. The technological process of aeration / bubbling serves to enhance the diffusion of oxygen into the water. Figure 5 shows one of the many construction schemes of this type of generators, where: 1 - nozzle; 2 - resonator; 3 - stem; 4 - the jet first cavitational nucleus; 5 - acoustic oscillations of the generator; φ_a - nozzle edge angle; ψ_R - resonator edge angle.

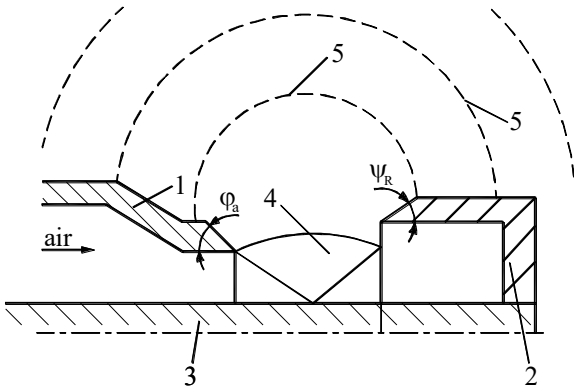

Fig. 5. *Oscillations occurrence in the sonic generator* [49]

The sonic gasodynamic generator proved to be a solution in water purification technology arising from aquaculture [50, 51], and also in some applications of liquids from food industry [52, 53].

In paper [54] the used axial sonic air-jet revealed a complete turbidity reduction from wastewater, after 40 seconds of treatment, with 40 NTU initial concentration. Paper [55] shows the reduction of ammonia concentration from industrial ammonia water, using the air-jet generator calculated by the method [56].

Conclusions

Sonochemical degradation seems to be a promising technology for the degradation of several organic compounds.

The present study shows the operational possibilities of the two types of existing ultrasonic transducers, namely mechanical and electromechanical (piezoelectric and magnetostrictive) transducers.

Piezoelectric transducers utilize the piezoelectric property of a material to convert electrical energy directly into mechanical energy. Magnetostrictive transducers utilize the magnetostrictive property of a material to convert the energy in a magnetic field into mechanical energy. Mechanical transducers utilize mainly the air as working agent to produce both low frequency ultrasound and bubbling.

All constructed types of ultrasonic transducers have promising results, but due to the large range of frequencies and power supply, the piezoelectric ones are the most commonly used.

It should be noted that the ultrasonic technology, regardless of the type of transducer, is generally used at laboratory scale, the magnetostrictive transducer being the best suited for industrial use.

Acknowledgements

The work has been funded by the Sectoral Operational Programme Human Resources Development 2007-2013 of the Ministry of European Funds through the Financial Agreement POSDRU/159/1.5/S/132397.

References

[1]. Gerardo L. *et al.*, *Increasing stability and transport efficiency of supported liquid membranes through a novel ultrasound-assisted preparation method. Its application to cobalt(II) removal*, Ultrasonics Sonochemistry, 20, 2013 p. 650-654.
[2]. Naddeo V. *et al.*, *Wastewater disinfection by combination of ultrasound and ultraviolet irradiation*, Journal of Hazardous Materials, 168, 2009, p. 925-929.
[3]. H. Hung *et al.*, *Kinetics and mechanism of the sonolytic degradation of chlorinated hydrocarbons: frequency effects*, J. Phys. Chem., A. 103(15), 1999, p. 2734-2739.
[4]. L. Wenjun *et al.*, *Removal of Organic Matter and Ammonia Nitrogen in Azodicarbonamide Wastewater by a Combination of Power Ultrasound Radiation and Hydrogen Peroxide*, Chinese Journal of Chem., 20, 2012, p. 754-759.
[5]. Parag R. Gogate, *Treatment of wastewater streams containing phenolic compounds using hybrid techniques based on cavitation: A review of the current status and the way forward*, Ultrasonics Sonochemistry, 15, 2008, p. 1–15.
[6]. P. Chowdhury *et al.*, *Sonochemical degradation of chlorinated organic compounds, phenolic compounds and organic dyes–A review*, Science of total environ., 407, 2009, p. 2474-2492.
[7]. Suslick K.S., *Sonochemistry*, Science, 247, 1990, p. 1438-1445.
[8]. Wu T. et al., *Advances in Ultrasound Technology for Environmental Remediation*, ISBN 978-94-007-5532-1, 2013.
[9]. Y. G. Adewuyi, *Sonochemistry: environmental science and engineering applications*, Ind. Eng. Chem. Res., 40(22), 2001, p. 4681-4715.
[10]. Pang Y. L. *et al.*, *Review on sonochemical methods in the presence of catalysts and chemical additives for treatment of organic pollutants in wastewater*, Desalination, 277, 2011, p. 1-14.
[11]. P. R. Gogate *et al.*, *A review of imperative technologies for wastewater treatment I: oxidation technologies at ambient conditions*, Advances in Environmental Research, 8, 2004, p. 501-551.
[12]. Songlin Wang *et al.*, *Removal of organic matter and ammonia nitrogen from landfill leachate by ultrasound*, Ultrasonics Sonochemistry, 15, 2008, p. 933-937.
[13]. Matouq M. A.-D., Al-Anber Z. A., *The application of high frequency ultrasound waves to remove ammonia from simulated industrial wastewater*, Ultrasonics Sonochemistry, 14, 2007, p. 393-397.
[14]. Vladimir N. Khmelev *et al.*, *Development and Application of Piezoelectric Transducer with the Enlarged Radiation Surface for Wastewater Treatment*, 10th International Conference And Seminar Edm'2009, Section Iv, July 1-6, Erlagol.
[15]. Nygren M. W., *Finite Element Modeling of Piezoelectric Ultrasonic Transducers*, Master of Science in Electronics, 2011.
[16]. Cavill S. A. *et al.*, *Electrical control of magnetic reversal processes in magnetostrictive structures*, Applied Physics Letters, 102, 2013.
[17]. Zhang H., *Power generation transducer from magnetostrictive materials*, Applied Physics Letters, 98, 2011.
[18]. Albach T. S. *et al.*, *Sound Generation Using a Magnetostrictive Microactuator*, Journal of Applied Physics, 109, 2011.
[19]. G. Thoma, M. Gleason, *Sonochemical Treatment of Benzene/Toluene Contaminated Wastewater*, Environmental Progress, 17, 1998, p. 154-160.
[20]. Hartmann J. *et al.*, *New Investigation on the Air Jet Generator for Acoustic Waves*, Kongelige Danske Videnskabernes Selskab Matematisk-Fysiske Meddelelser, 7, 1926.
[21]. Hartmann J. *et al.*, *A New Acoustic Generator. The Air-Jet-Generator*, Journal of Scientific Instruments, 4, 1927, p. 101-111.
[22]. Hartmann J., *Construction, Performance, and Design of the Acoustic Air-Jet Generator*, Journal of Scientific Instruments, 16, 1939, p. 140-149.
[23]. Hartmann J. *et al.*, *Synchronization of Air-Jet Generators with an Appendix on the Stem Generator*, Kongelige Danske Videnskabernes Selskab Matematisk-Fysiske Meddelelser, 26, 1951.
[24]. Balan G. *et al.*, *The sonic technologies*, Quatrieme Edition Du Colloque Francophone en Energie, Environnement, Economie et Thermo-dynamique COFRET'08, Nantes, France, 2008, p. 20-29.
[25]. Stefan A., *The research of the physico-chemical parameters of water treated with sonic technology*, Journal of science and arts, Târgoviște, 12, 2010, p. 79-82.
[26]. Matei N., *Sonic treatment effect on industrial ammonia water decontamination*, The Annals of "Dunarea de Jos" University of Galati, ISSN 1221-4558, 2013, p. 62-67.
[27]. Gelate P, Hodnett M, Zeqiri B., *Supporting infrastructure and early measurements*, National Physical Laboratory Report. Teddington. Middlesex, UK, 2000, p. 2-11.
[28]. ***, *Application of Ultrasonic Technology for Water and Wastewater Treatment*.
[29]. R. S. C. Cobbold, *Foundations of biomedical ultrasound*, Oxford University Press, 2006.
[30]. Nygren M., *Finite Element Modeling of Piezoelectric Ultrasonic Transducers*, Master of Science in Electronics, Norwegian University of Science and Technology, 2011.
[31]. F. J. Fuchs *et al.*, *Application of Multiple Frequency Ultrasonics*, Blackstone ultrasonics, 716, 2005, p. 665-2340.
[32]. Fabijanski P. *et al.*, *Modeling and Identification of Parameters the Piezoelectric Transducers in Ultrasonic Systems*, Advances in Ceramics - Electric and Magnetic Ceramics, Bioceramics, Ceramics and Environment, ISBN 978-953-307-350-7, InTech, 2011.
[33]. Gogate P. R. *et al.*, *Mapping of sonochemical reactors: review, analysis, and experimental verification*, AIChE J. 48, 2002, p. 1542-1560.
[34]. Sostaric J. Z. *et al.*, *Advancement of high power ultrasound technology for the destruction of surface active waterborne contaminants*, Ultrasonics Sonochemistry, 17, 2010, p. 1021-1026.
[35]. Rochebrochard S. *et al.*, *Sonochemical efficiency dependence on liquid height and frequency in an improved sonochemical reactor*, Ultrasonics Sonochemistry, 19, 2012, p. 280-285.
[36]. ***, *Design and calibration of a single-transducer variable-frequency sonication system*.
[37]. Matouq M. A. *et al.*, *Degradation of dissolved diazinon pesticide in water using the high frequency of ultrasound wave*, Ultrasonics Sonochemistry, 15, 2008, p. 869-874.
[38]. Zhang Y. *et al.*, *The degradation of chlorpyrifos and diazinon in aqueous solution by ultrasonic irradiation: Effect of parameters and degradation pathway*, Chemosphere, 82, 2011, p. 1109-1115.
[39]. Young K. *et al.*, *Decomposition of monochlorophenols by sonolysis in aqueous solution*, Journal of Environmental Engineering and Management, Vol. 16, No. 4, 2006, p. 259-265.
[40]. Gogate P. R. *et al.*, *Destruction of formic acid using high frequency cup horn reactor*, Water research, 40, 2006, p. 1697-1705.
[41]. Claeyssen F. *et al.*, *Actuators, transducers and motors based on giant magnetostrictive materials*, Journal of Alloys and Compouns, 258, 1997, p. 61-73.

[42]. Dapino M. *et al.*, *A structural-magnetic strain model for magnetostrictive transducers*, J of Magnetics, Vol. 36, Issue 3, p. 545-556, ISSN 0018-9464.
[43]. Cullity B.D. *et al.*, *Introduction to Magnetic Materials*, Wiley, New Jersey, 2009, p. 258.
[44]. Petrier C. *et al.*, *Characteristics of Pentachlorophenate Degradation in Aqueous Solution by Means of Ultrasound*, Environ. Sci. Technol., 26(8), 1992, p. 1639-1642.
[45]. Pedeflous F., *Ultrasonic Transducers: Piezoelectric vs. Magnetostrictive*, http://blog.omegasonics.com/archives, 2014.
[46]. ***, *Magnetostrictive Versus Piezoelectric Transducers For Power Ultrasonic Applications*, www.ctgclean.com.
[47]. Serban A., *Utilizarea generatoarelor sonice gazodinamice în procesele tehnologice de epurare a apelor uzate*, Ed. Zigotto, Galati, ISBN 978-606-8303-57-4, 2009.
[48]. Magheţi I., Savu M., *Teoria şi practica vibraţiilor mecanice*, Ed. Didactică şi Pedagogică, Bucureşti, ISBN 978-973-30-1969-9, 2007.
[49]. Bălan G., *Principii de elaborare a sistemelor tehnice cu injectoare sonice*, Teza de doctor Habilitat, U.T.M., Chişinău, 2001.
[50]. Bălan G. *et al.*, *Acoustical research of the sonic air-jet radial generator*, Analele Universităţii Maritime, Anul IX, Vol. 11, p. 293-298, ISSN 1582-3601, Constanţa, 2008.
[51]. Graur I. *et al.*, *Sonic activation of water derived from aquaculture and microbiological effect*, Poss. Conf. Int. „Modern technologies in the food industry - 2012", Chisinau, 2012.
[52]. Graur I. *et al.*, *Effects of Air-Jet Stem Generator and UP400S Treatment on Vitamin C, Colour and pH of Grapefruit Juice*, International Journal of Engineering Science and Innovative Technology (IJESIT), Vol. 2, Issue 5, 2013, p. 180-184.
[53]. Bălan V., Balan G., *The sonic technology in the beer industry*, The Annual Symposium of the Institute of Solid Mechanics SISOM 2012 and Session of the Commission of Acoustics, ISSN: 0035-4074, Bucharest, 2012.
[55]. Stefan A. *et al.*, *The physical and chemical indicators at the ultrasound treatment of water with poly aluminium chloride*, Annals of Dunarea de Jos University of Galati, Fascicle II, ISSN 2067-2071, 2011, p. 164-170.
[55]. Matei N., *Sonic treatment effect on industrial ammonia water decontamination*, Annals of Dunarea de Jos University of Galati, Fascicle IV, ISSN 1221-4558, 2013, p. 62-67.
[56]. Bălan G. *et al.*, *The sonic technologies*, Quatrieme Edition Du Colloque Francophone en Energie, Environnement, Economie et Thermo-dynamique COFRET'08, Nantes, France, 2008, p. 20-29.

THE ANNALS OF "DUNAREA DE JOS" UNIVERSITY OF GALATI
FASCICLE IX. METALLURGY AND MATERIALS SCIENCE
Nº. 2 - 2015, ISSN 1453 – 083X

SOLUTIONS FOR DIAGNOSING FAULTS IN AN ASYNCHRONOUS MOTOR STATOR THROUGH A FERROFLUID INSTALLATION

Ovidiu-Magdin Țanța[a,b,*], Adrian-Neculai Romanescu[a], Mihai Cenușă[a], Ilie Nițan[a], Mihaela Poienar[a]

[a] "Ștefan cel Mare" University of Suceava, Faculty of Electrical Engineering and Computer Science, 13 Universității Street, 720229, Suceava, Romania
[b] E.ON Distribuție România, 21 Piaţa Trandafirilor Street, 540049, Târgu Mureș, Romania
*Corresponding author
e-mail: ovidiu.tanta@eon-romania.ro

ABSTRACT

Due to their reliability, robustness and multitude of variants of motors, electric machines are commonly used in industrial drives. Although they are relatively simple pieces of equipment, asynchronous motors can sometimes malfunction because of various reasons. Whether it is a problem in the supply network (lack of a phase, wrong phase sequence, different phase voltages, etc.) or an internal fault in the stator winding (interrupted winding, reversing the winding so that it begins with the end, shortened coils, etc.) motors diagnosis was a constant concern among specialists. Although a number of classic solutions are known, generally pertaining to the type of defect assumed, this paper proposes a completely new approach applicable to all types of anomalies that may occur in the functioning of these engines.

KEYWORDS: ferrofluid, rotating magnetic field, asynchronous motor

1. Introduction

The magnetic fields study and the opportunities to highlight the load line were constant concerns for the EMAD research team from "Ștefan cel Mare" University of Suceava. During the experiments, a series of images were obtained by exposing the content of a cylindrical container to a continuous magnetic field action. These images were named "CEUS figures" (Electrotechnical Department of the University of Suceava), the acronym being suggested by academician Emanuel Diaconescu in a scientific session.

Using CEUS figures, a series of devices were made in order to diagnose the defects that may appear at the machines. Because of the multitude of causes that lead to machine malfunction, we have tried to identify some types of defects. For example, the defects in the driven magnetic circuits have as immediate effect strong local heating, which leads to the premature aging of insulation. However, the most frequent defects are located in the stator winding, and they could be: strong heating, stiff starting, anomalous noise, absorbed currents unequal on phases, inappropriate rotational frequency and insufficient power.

2. Apparatus for asynchronous motors defects diagnosis

The experimental model used to obtain the CEUS figures consists, mainly, of the stator of a three-phase asynchronous motor whose rotor has been replaced by a sample container made of an insulating material, partially filled with ferrofluid. To highlight the ferrofluid movement and to capture the CEUS figures, the fluid surface was interspersed with bronze ultrafine powder that had indicator role.

The unfolded arrangement of the stator winding of the experimental apparatus is shown below in Figure 1 and Figure 2.

The CEUS figures having the form shown in Figure 2 were obtained by applying the continuous magnetic field produced by the stator of the asynchronous motor over the ferrofluid from the insulating cylindrical container.

To correlate the images with the direction of the field lines, we used a pointer located in the center of the stator, which deviated or rotated in the direction of the rotating magnetic fields when the stand was supplied.

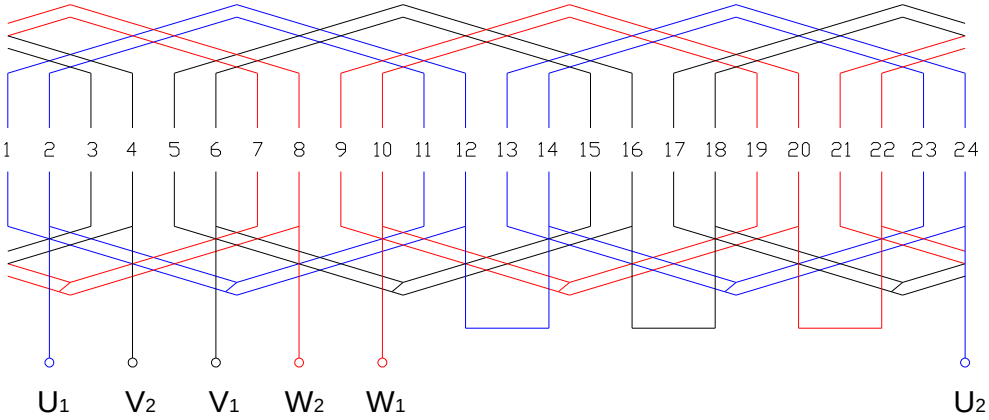

Fig. 1. *Stator winding schema used in the arrangement*

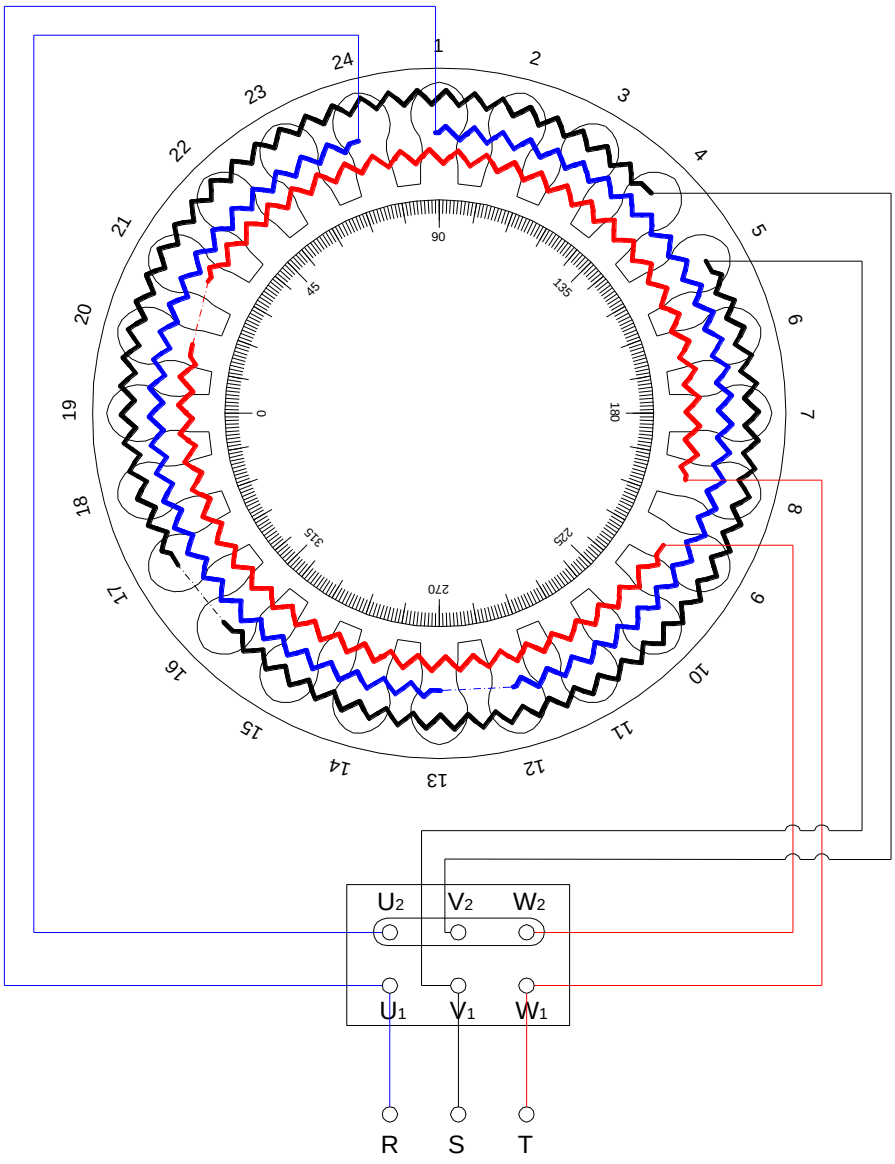

Fig. 2. *The windings disposal on the three phases into the ferrofluid container*

The entire experimental study consists of 31 distinct abnormal operating situations of the asynchronous motor for: defects in the supply network, flawed terminal connection or stator windings internal defects. Due to limited space, this paper presents only a small part of the results, respectively the typical images of the following situations:

- engine supplied in delta connection with a phase missing in the electric-power-supply-network;
- engine supplied in Y connection with a phase missing in the electric-power-supply-network;
- engine supplied in delta connection with an interrupted winding in the stator coil;
- engine supplied in Y connection whose winding whereat was reversed, beginning with the end;
- engine supplied in "V" connection.

3. The diagnosis of asynchronous motors malfunctioning

The CEUS figures for various abnormal motion types of the asynchronous motor are shown in the images presented below:

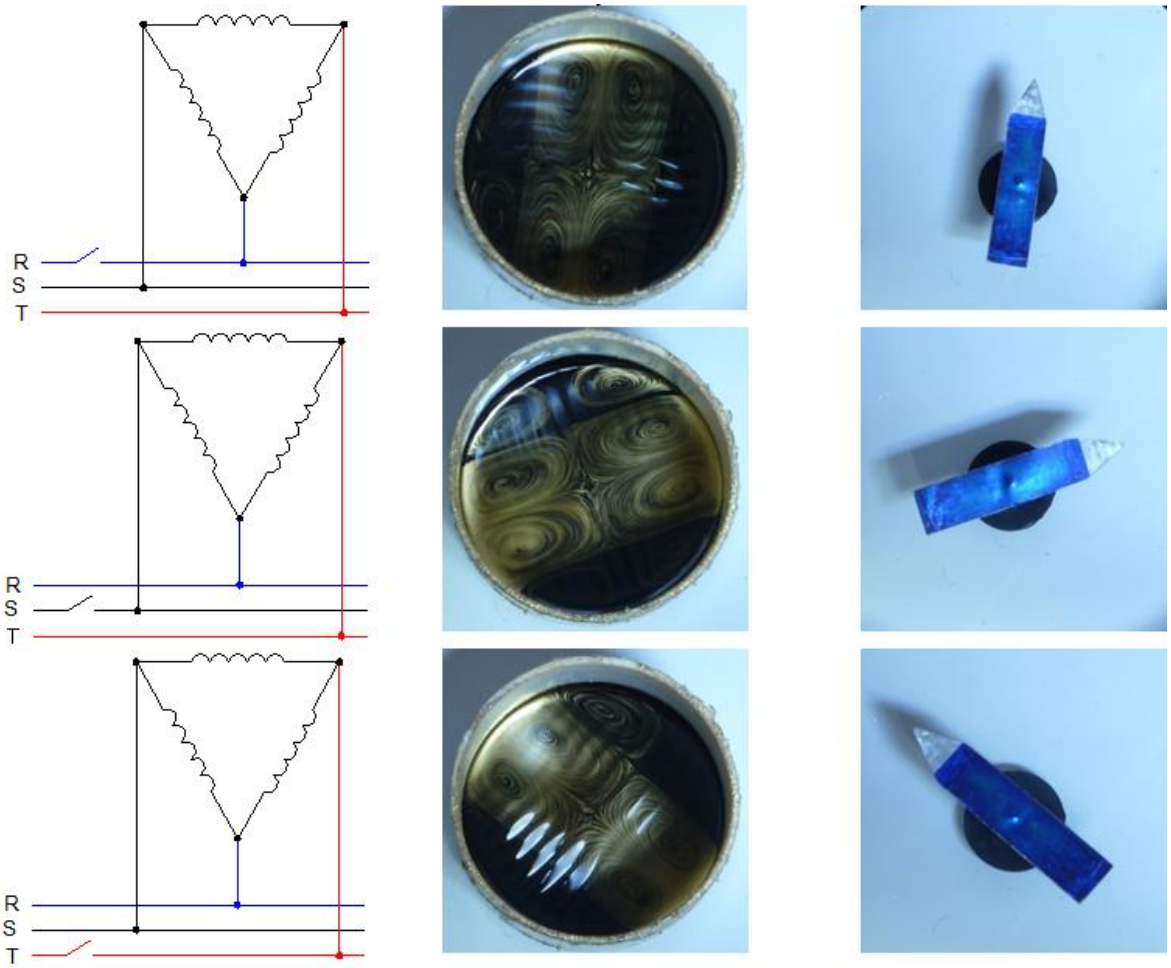

Fig. 3. *Engine supplied in delta connection with a phase missing in the electric-power-supply-network*

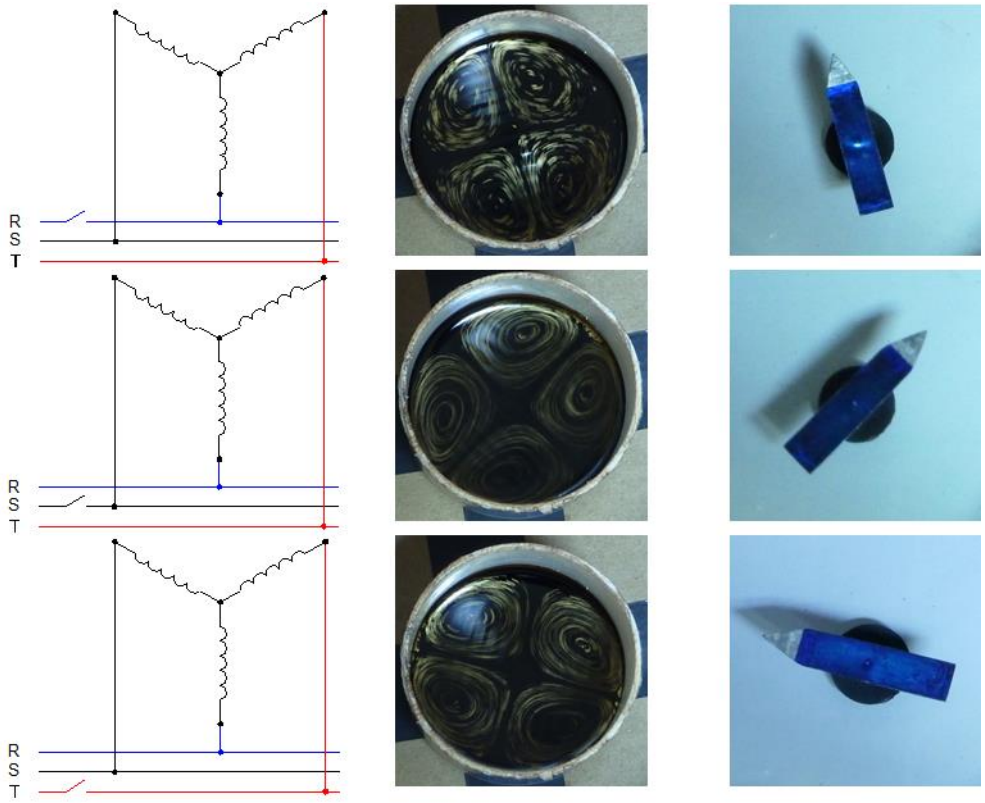

Fig. 4. *Engine supplied in Y connection with a phase missing in the electric-power-supply-network*

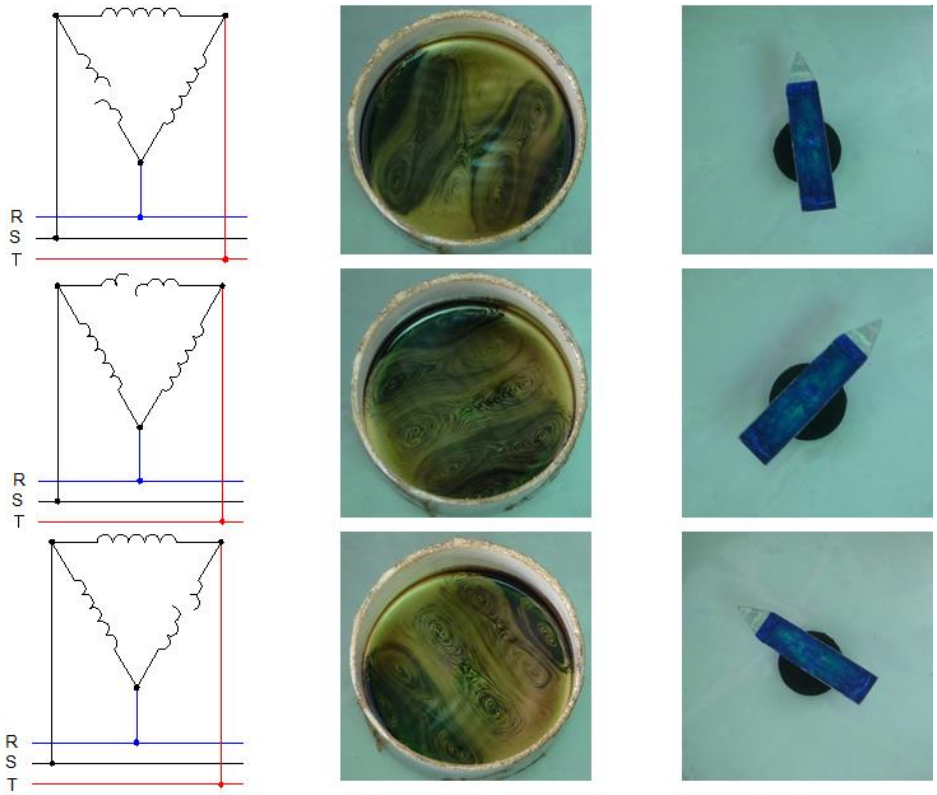

Fig. 5. *Engine supplied in delta connection with an interrupted winding in the stator coil*

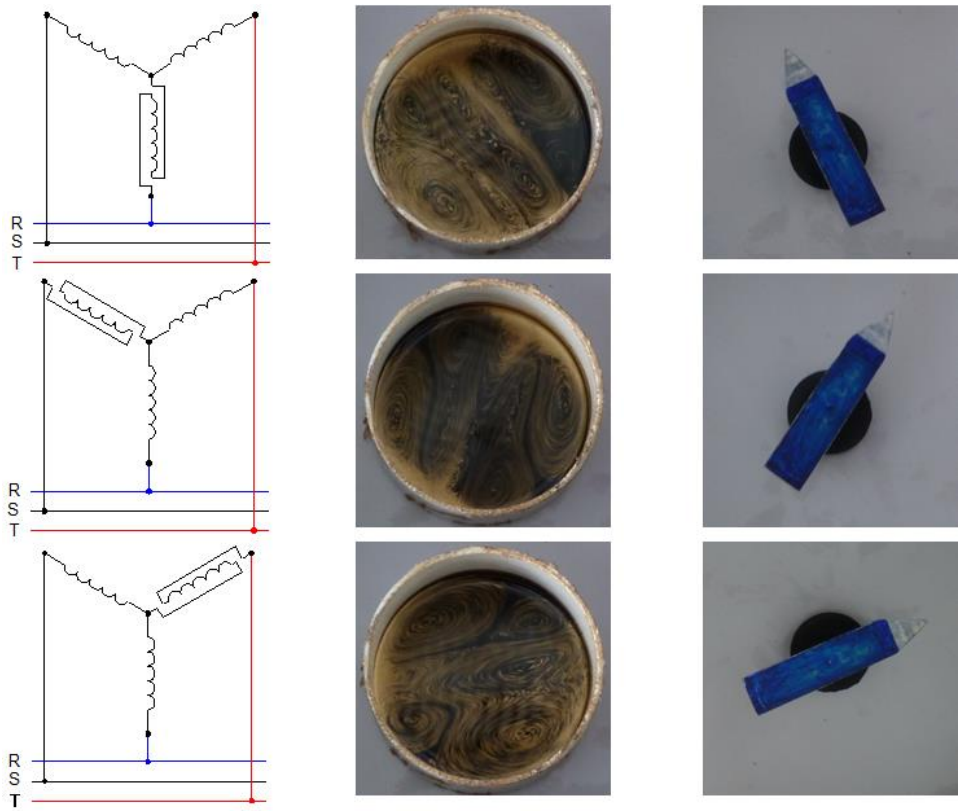

Fig. 6. *Engine supplied in Y connection whose winding was reversed, beginning with the end*

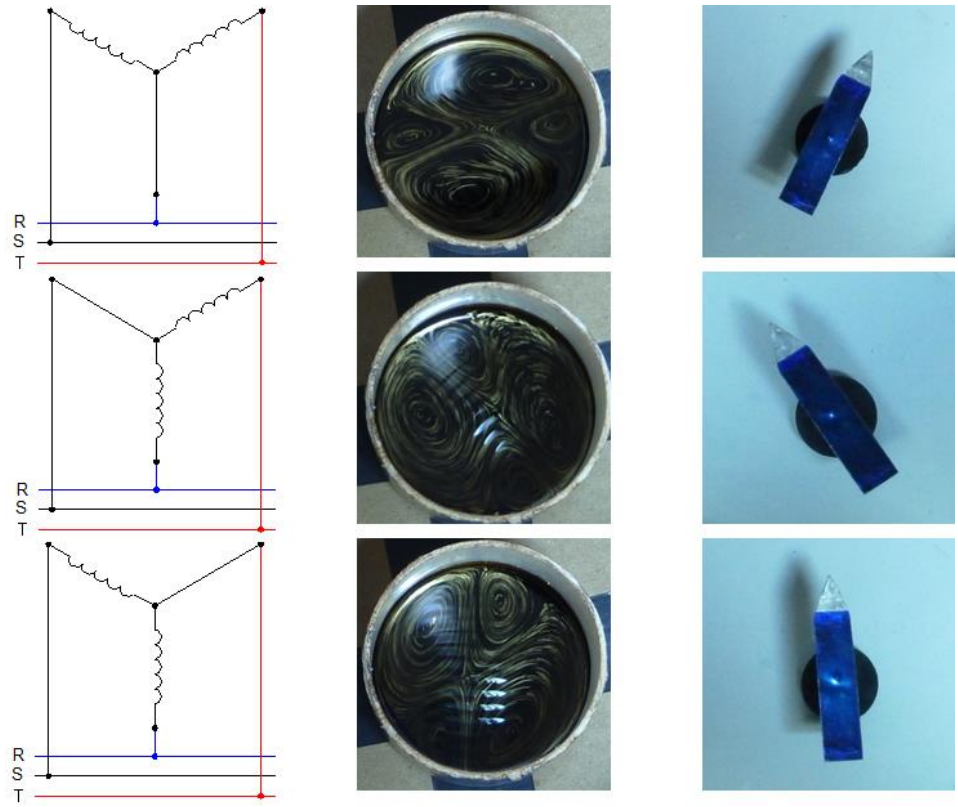

Fig. 7. *Engine supplied in "V" connection*

4. Conclusion

- The rotating magnetic field sense of rotation produced by the analyzed stator is given by the phase sequence. The ferrofluid sense of rotation is reversed compared to the rotating magnetic field.
- During the research a method has been developed to highlight the movement, by sprinkling the ferrofluid surface with a powder that has indicator role.
- To obtain the ferrofluid motion pictures at low rotational speed, a high performance camera with a high exposure time was used.
- The CEUS figures obtained are true stamps that can provide information for malfunction diagnosis of an asynchronous motor stator. Whether it is a problem in the supply network, a flawed terminal connection or stator windings internal defects, the images may point to a certain type of defect.

References

[1]. Bălă C., Fetița A., Lefter V., *Cartea bobinatorului de mașini electrice*, București: Editura Tehnică, 1967.
[2]. Bogatu V., *Probe și verificări ale mașinilor electrice*, București: Editura Tehnică, 1968.
[3]. Buzduga C., *Contribuții la extinderea aplicațiilor ferofluidelor și pulberilor feromagnetice în electrotehnică*, Teză de doctorat. Suceava: Universitatea „Ștefan cel Mare", Facultatea de Inginerie Electrică și Știința Calculatoarelor, 2012.
[4]. Luca E., Călugăru Gh., Bădescu R., Cotae C., Bădescu V., *Ferofluidele și aplicațiile lor în industrie*, București: Editura Tehnică, 1978.
[5]. Negru M. B., *Contribuții privind extinderea aplicațiilor ferofluidelor și a pulberilor feromagnetice în electrotehnică*, Teză de doctorat. Suceava: Universitatea „Ștefan cel Mare", Facultatea de Inginerie Electrică și Știința Calculatoarelor, 2012.
[6]. Răduți C., Nicolescu E., *Mașini electrice rotative fabricate în România*, București: Editura Tehnică, 1981.
[7]. Vrînceanu Gh., Schnell Fl., *Stabilirea defectelor în instalațiile electrice de joasă tensiune*, București: Editura Tehnică, 1976.

THE ANNALS OF "DUNAREA DE JOS" UNIVERSITY OF GALATI
FASCICLE IX. METALLURGY AND MATERIALS SCIENCE
Nº. 2 - 2015, ISSN 1453 – 083X

THE STRUCTURAL DESIGN IMPROVEMENT OF A TWIN-HULL SHIP

Adrian Presura, Ionel Chirica, Elena-Felicia Beznea
"Dunarea de Jos" University of Galati, Faculty of Engineering, 47 Domneasca Street, , 800008, Galati, Romania
e-mail: a.presura@shipdesigngroup.eu, ionel.chirica@ugal.ro, elena.beznea@ugal.co

ABSTRACT

The paper is focused on the strength analysis of the structure of twin-hull ships, particularly a passenger catamaran. Catamarans have some advantages against conventional monohulls: larger deck area and cargo volume, better transverse stability and, in general, improved behavior in waves. But due to the need of large open spaces, for passenger / car ferry ships and having as major restriction the structure weight, one of the problems which arise during the designing of the catamaran structure is the determination of the effectiveness of deck structure. The Finite Element Method was used for examining the behavior of different deck structure designs in order to determine the solution which meets better designing criteria regarding allowable stress and deformations and total weight. The results of this analysis show that, making a proper structural analysis and using lightweight materials, important gains for ship owners and for environment protection can be achieved.

KEYWORDS: catamarans, deck structures, FEM analysis, lightweight materials

1. Introduction

This study is based on a new concept of inland navigation catamaran for 150 passengers, having 28.5 m length, 7.8 m beam, 1 m maximum hull draft and a maximum speed of 25 km/h. Considering the small draft and relatively high speed, the total light ship weight must remain as low as possible so the material used for construction of hulls, main deck and superstructure deck is aluminium or glass reinforced plastics (GRP).

The craft has a closed salon for passengers on the main deck and an open salon on the upper deck, which adds significant load on the upper deck structure.

In addition, this particular design meets the owner's request for availability of different deck arrangements without any hull structure modifications.

Consequently, the number of pillars or other similar supporting structures was reduced to minimum or even none, in order to ensure maximum flexibility in deck arrangements, thus increasing the span of primary supporting members.

In this research, were analyzed different structure solutions for the upper deck, in order to meet, as far as practicable, the above designing restriction and other criteria, presented later.

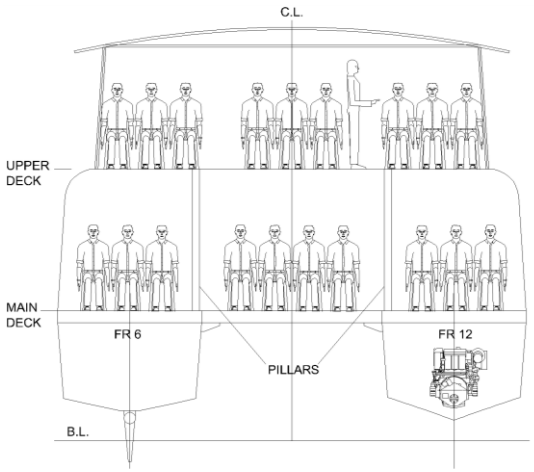

Fig. 1. *Ship transverse section*

2. Designing criteria and restrictions

In order to make a qualitative assessment of different structure designs, several designing criteria and also some objective restrictions were considered.

Designing criteria:

i) **Permissible stress** was considered for Aluminium Alloy 6005A-T6 as follows:

- primary stiffeners

σ_{locam}	τ_{locam}	σ_{VM}
76[N/mm^2]	54[N/mm^2]	86[N/mm^2]

- ordinay stiffeners

σ_{locam}	τ_{locam}
70[N/mm^2]	49[N/mm^2]

σ_{locam} – local permissible bending stress
τ_{locam} – local permissible shear stress
σ_{VM} – allowable equivalent stress

In order to reduce the weight, one aim was to avoid the oversizing of structure elements. Therefore, the geometric characteristics of primary and ordinary stiffeners were varied so to achieve stresses as close as possible to the permissible values, considering nevertheless a safety margin of 80% from the above mentioned values.

ii) The maximum allowable **deflection of the deck structure = 8 mm** was considered L/500, where L was taken as spacing between the transverse primary supporting members (maximum distance of 4 m). This limit of deflection is related to the on board people's well-being and is usually met in civil construction regulations.

iii) The maximum **deflection of windows framing = 5 mm** was considered not to exceed 1/175 of the glass smaller edge length (windows dimensions 2 m x 1 m), according to the United States building regulations (IBC 2006 Section 2403.3) as to ensure the integrity of the windows.

Designing restrictions:

i) The **weight** of the structure was optimized, as a general desideratum in ship building and especially for this catamaran with relatively small displacement (abt. 60 t) and shallow draft (abt. 1 m). In this regard, taking as example 1 t of weight reduction, several advantages can be gained for the project:

- more passengers on board 1 t = 10 average people with their luggage;
- more fuel oil and/or other stores on board, meaning greater flexibility in operation;
- less hull resistance because of draft reduction.

ii) **Ventilation ducts** required for the 150 people salon need a minimum height of 0.1 m clearance in order to ensure a good distribution of air and a reduced level of noise. In consequence, the upper deck stiffeners had either to allow such large cutouts for the passage of ventilation or to have minimum overall height so as to permit the installation of the ventilation duct underneath (Figure 2).

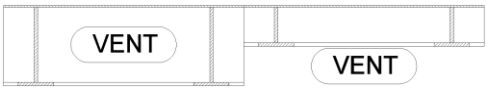

Fig. 2. *Installation of ventilation ducts*

iii) **Structure arrangement** was another restriction, considering the owner's request to have minimum / none intermediate supporting members, at the level of main and upper decks. In this way it will be possible to rearrange the spaces, for example from a hidrobus / economy type for 100/150 passengers to a pleasure / business type for 60 passengers (Figure 3).

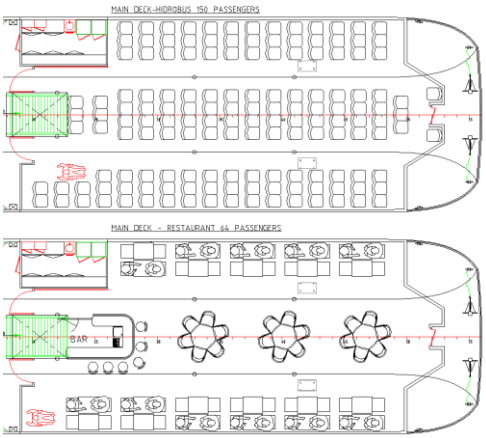

Fig. 3. *Deck arrangement*

3. Assumptions and methods

In the structural analysis developed further, the following simplifying assumption was considered: the main deck (strength deck) of the catamaran is rigid and the transverse bulkheads enclosing the aft and fore ends of the upper deck structure are also rigid.

Boundary condition (Figure 4):

- fixed displacement and fixed rotation constraints at the level of the main deck (Ux, Uy, Uz, Rx, Ry, Rz);
- fixed displacement and fixed rotation constraints at transverse sections limiting de model in longitudinal direction (Ux, Uy, Uz, Rx, Rz).

Design loads:

- lateral pressure on the sides of the superstructure p_s = 2.3 kN/m^2, according to "NR217-Rules for Inland Navigation Vessels – PartB – Ch. 6, Sec 4";

- pressure due to the load carried on deck p_d = 5 kN/m^2, according to "NR217-Rules for Inland Navigation Vessels – PartB – Ch. 6, Sec 4";
- weight of structure above the upper deck abt. 1 kN force at every supporting pillar.

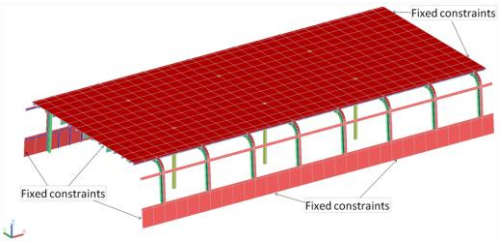

Fig. 4. *Boundary conditions*

The structural analysis was performed with Finite Element Method, using SHELL 3T elements, average size 0.05 m, COSMOS software and beam elements, NAUTICUS 3D-Beam software.

4. Analysis of different structure designs

The research started from a typical structure design, having primary supporting members disposed transversely at every 2 m and ordinary stiffeners spaced transversely and longitudinally at every 0.5 m. Based on "BV Rules for the Classification of Inland Navigation Vessels" some minimum net thicknesses were calculated for deck plating, web plating of ordinary and primary stiffeners.

Furthermore, this typical structure was optimized, considering the equal strength principle, aiming at lightening those elements with low stress and/or deflection.

Finally, a transverse arch structure was investigated aiming at reducing even more the total weight of the structure.

4.1. Typical structure

In Figure 5 below are shown the elements that form the structure:

- shell plates of 5 mm;
- primary supporting members web of 220 x 8 mm and flange of 100 x 8 mm;
- ordinary stiffeners web of 100 x 6 mm and flange of 100 x 8 mm;
- side bulkheads ordinary stiffeners face plate 70 x 6 mm;
- pillars of ϕ 130 x 10 mm.

The results showed the following situation:

- the maximum von Mises stress of 38 N/mm^2 (well below the limit of 86 N/mm^2) was reached in primary supporting members as shown in Figure 6;
- deck deflection of 4 mm, in the areas shown in Figure 7.

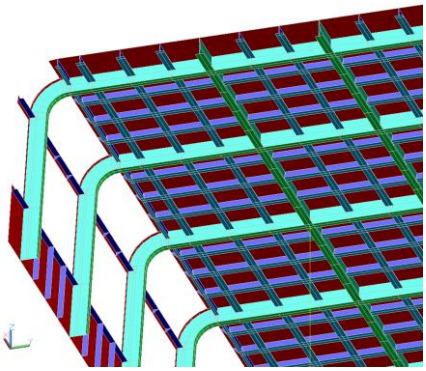

Fig. 5. *Typical structure details*

Total weight	Max. von Mises stress	Max. displacement
[t]	[N/mm^2]	[mm]
4.187	37.7	4.2

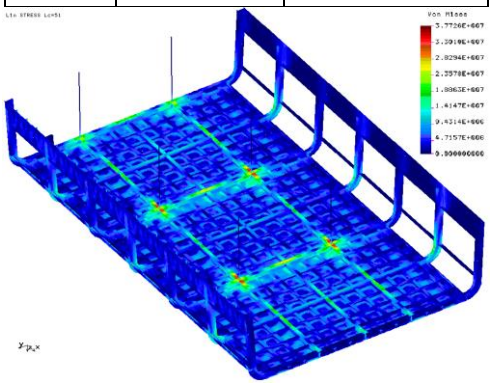

Fig. 6. *Typical structure - von Mises stress*

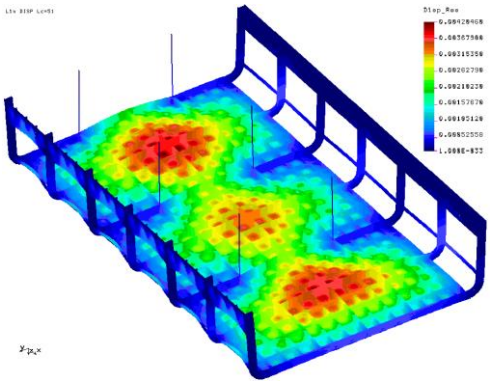

Fig. 7. *Typical structure - displacement*

4.2. Optimized typical structure

Based on the above results, some improvements are possible:

i) reducing and even eliminating the ordinary stiffener flanges of 100 x 8 mm, due to low stress level. The weight reduction was about 0.6 t (14% from the initial weight).

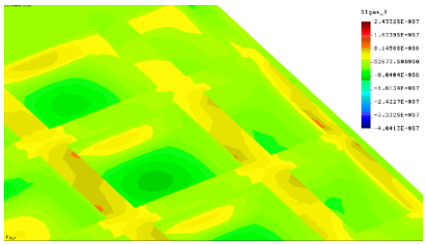

Fig. 8. *Typical structure – ordinary stiffener flange stress*

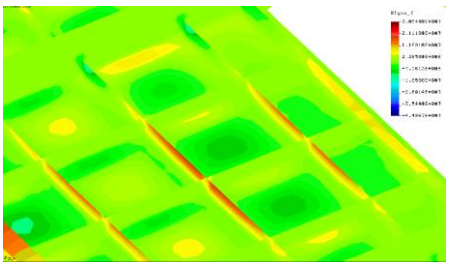

Fig. 9. *Optimized typical structure – ordinary stiffener flange stress*

ii) reducing the section area of vertical primary supporting members, due to the low stress level. The weight reduction obtained was about 0.175 t (4% from the initial weight).

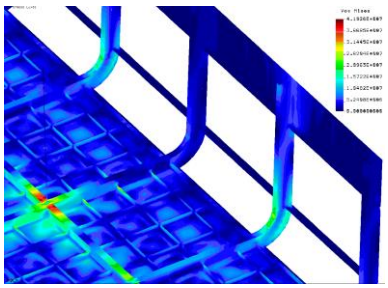

Fig. 10. *Typical structure – von Misses stress in primary vertical members*

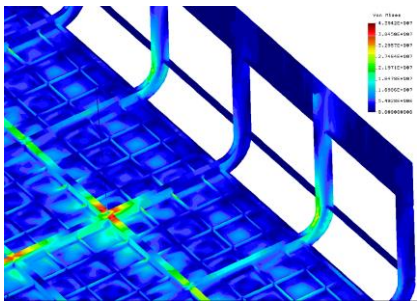

Fig. 11. *Optimized typical structure – von Misses stress in primary vertical members*

Total weight	Max. von Mises stress	Max. displacement
[t]	[N/mm^2]	[mm]
3.412	≈40	≈4

Conclusion: The total weight of the initial structure was reduced by 18%.

4.3. Transverse arch structure

Aiming at reducing the number of pillars and at the same time at keeping deck deflection below limits, a beam model was used to evaluate the efficiency of a transverse arch frame solution.

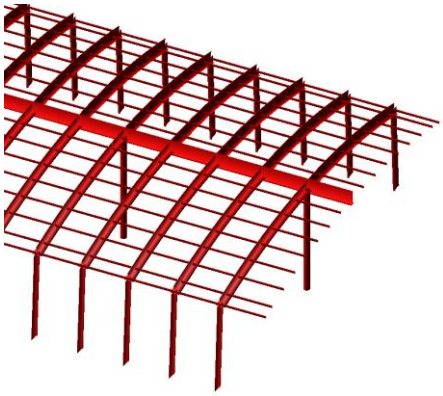

Fig. 12. *3D Beam model – arch structure*

In Figure 12 below are shown the elements that form the structure:

- arch transverse beam web of 200 x 10 mm;
- central longitudinal stiffeners web of 300 x 8 mm and flange of 100 x 8 mm;
- longitudinal ordinary stiffeners flat plate of 50 x 5 mm;
- side stiffeners web of 200 x 6 mm and flange of 50 x 5 mm;
- only one line of pillars of ϕ 130 x 10 mm.

The results showed the following situation:

Total weight	Max. von Mises stress	Max. displacement
[t]	[N/mm^2]	[mm]
3.820	45	5.6

Conclusion: The total weight increased by 12% than the optimized typical structure presented above but the deflection was similar.

By comparison, the same structure, but having straight transverse stiffeners, showed significantly higher deflection:

- the maximum von Mises stress of 69 N/mm^2;
- the maximum deck deflection of 8.2 mm.

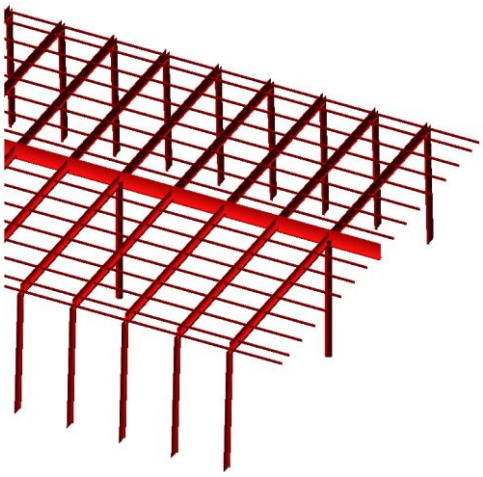

Fig. 13. *3D Beam model – straight transverse structure*

5. Conclusions

This research underlined two aspects:

i) the weight of a ship structure can be considerably decreased, from the initial design based on "Rules" dimensioning, using a FEM calculation;

ii) a classical structure solution, such as arch design, can be integrated in a ship structure in order to reduce the number of intermediate supporting members.

Acknowledgement

The present research has been supported by Ship Design Group Galati.

References

[1]. ***, *NR217 - Rules for Inland Navigation Vessels*, November Edition 2014.
[2]. ***, *2008 New York City Building Code*, (IBC 2006 Section 2403.3).
[3]. ***, COSMOS software.
[4]. ***, 3D-Beam software.

THE ANNALS OF "DUNAREA DE JOS" UNIVERSITY OF GALATI
FASCICLE IX. METALLURGY AND MATERIALS SCIENCE
Nº. 2 - 2015, ISSN 1453 – 083X

CONTRIBUTIONS REGARDING THE DEVELOPMENT OF NEW TYPES OF SOLAR ACTUATORS

Adrian-Neculai Romanescu, Ovidiu-Magdin Țanța, Mihai Cenușă, Ilie Nițan, Mihaela Poienar*
"Ștefan cel Mare" University of Suceava, Faculty of Electrical Engineering and Computer Science,
13 Universității Street, 720229, Suceava, Romania
*Corresponding author
e-mail: mihaela_poienar@yahoo.com

ABSTRACT

The paper presents the authors' contributions to the development of solar actuators with bimetallic band and Bourdon tube in the EMAD Research Centre of "Ștefan cel Mare" University of Suceava. The solutions and the experimental devices are described with their peculiarities and advantages. The paper ends with main conclusions about the testing of the actuators and their practical implementation.

KEYWORDS: bimetallic band, Bourdon tube, actuator

1. General considerations

Within the EMAD Research Center of the USV, a number of solutions have been developed since 1996 in heliothermic actuators and motors area made based on solid heating medium [3].

The solutions relate to rotary actuators and motors as well as linear actuators with limited movement.

This study presents the primary constructive solutions with their peculiarities and the general conclusion regarding the experimentation and practical implementation.

By solid heating medium is obtained a thermo-bimetal or a shape memory material after the action of temperature.

In technical applications, thermo-bimetals are widely used because at temperature variation they can produce:

- movement due to deformation;
- force due to internal stresses that occur if external forces prevent strain production.

Both of these effects can be achieved with thermo-bimetals of different forms, such as: hogging thin bands, U shaped work where the angular aperture varies, twisting contrivance or helical spiral, discs whose bend varies, as it is shown in Figure 1.

Overall technical applications were used for the combined effect of force and motion production by a heated thermo-bimetal. The two effects are applied in sequence or simultaneously. For example, a bimetallic band embedded at one termination can operate as a pawl. By heating and moving the band hogs at the free point, proportional to the temperature, until the pawl comes in contact with it, the movement ceases in practice. By raising the temperature further, internal stresses occur which increase proportionally to temperature until they achieve the value necessary to operate the pawl. Then the bimetallic piece can close or disclose a contact [3].

a)

b)

c)

Fig. 1. *Thermo-bimetallic modules a) bimetallic arc modeled after a cylindrical helical path; b) bimetallic arc modeled after a conical helical path; c) bimetallic arc curved – preformed in "U" shape* [3]

In this way, numerous constructions used in electrotechnics operate to actuate a process when limit temperature is reached, such as: overload protection relay and temperature controller (thermostat for warming pads or chambers, flatting mills with regulators, warmers, baking machines, etc.).

Another one is the operation of a helical band in the form of an arc, made of thermo-bimetal, that must overcome the elastic force of a spring. The thermo-bimetal member, through heating, deforms and acts with a force over the spring, compressing it. Increasing the resistance force of the spring, as it is compressed, proportionally to the extent of deformation, prevents the thermo-bimetal movement. The thermo-bimetal will continuously shift on an increasingly smaller distance, as the spring elastic force does not increase proportionally to the temperature variation.

2. Heliothermic mixed actuator with parabolic concentrator

One of the solutions achieved in the EMAD Research Center is the heliothermic mixed actuator consisting of a mechanical converter with thermo-bimetallic band associated with a thermo-mechanical converter with paraffin, both placed in the solar concentrator focusing point as it is presented in Figures 2 and 3.

The solution is made of a bimetallic band 1, modeled after a spiral arc with several coils, embedded in a paraffin based thermo-conductor agent 2, contained in a flat cylindrical container 3, sealed and placed through a cannular fastening piece 4 in the parabolic concentrator focusing point 5, fixed in turn by an adjusting bolster with toggle joint 6 on a supporting surface 7. The bimetallic band 1 is anchored to the inner wall of the container 3, and the inner end of the axle with pap which is supported in a sliding bearing sealed through an insertion. The axle stub is connected through a mechanical thimble 8 to a flexible axle, positioned within the tubular support 4, which actuates the associated mechanism.

To compensate the volume variations of the agent 2 at the transition from the solid to the liquid phase, under the solar radiation action, it is used an assembly consisting of two Bourdon tubes 10 and 10' positioned coaxially and coplanar. Through the collecting channels 11 and 11', the Bourdon tubes are clamped to the cylindrical surface of the container 3 and are connected at the same time to the thermo-conductor agent 2.

The molten paraffin discharged to the 10 and 10' Bourdon tubes determines, through the pressure created, their outwards deformation. In the manner described, the deformation is converted, through a bar with spool and spring 12 and 12', in linear drive, and transmitted to other two mechanisms.

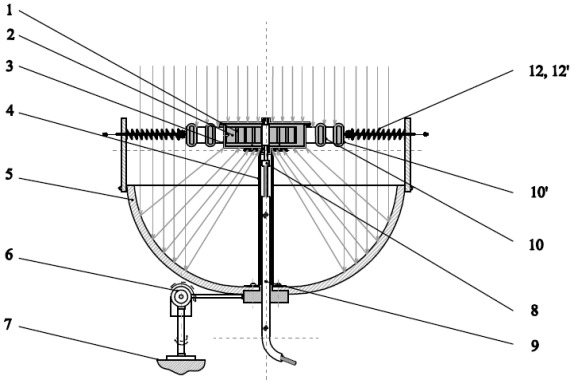

Fig. 2. *Longitudinal section through the heliothermic mixed actuator with parabolic concentrator* [1]

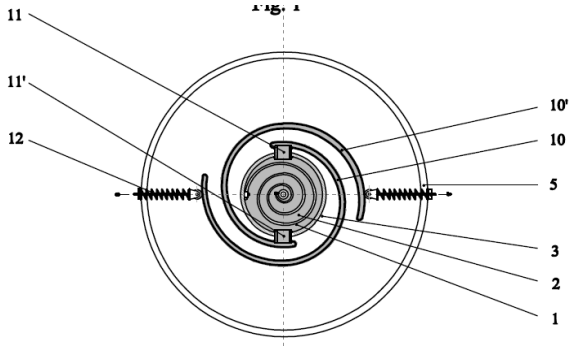

Fig. 3. *Transverse section through the heliothermic mixed actuator with parabolic concentrator* [1]

The advantages of the solution are:
- increased number of operable elements;
- reduced size;
- construction simplicity.

3. Heliothermic mixed actuator with a cylindrical – parabolic concentrator

Another solution is shown in Figure 4 and is made through a thermo-bimetallic converter associated with a thermo-mechanical converter with paraffin and piston together with a thermo-mechanical convertor with paraffin and Bourdon tube.

The heliothermic mixed actuator consists of a bimetallic band 1, shaped as a coiled layout and placed within a tubular container 2 made of brass and closed by a bonnet 2', sealed through an insertion 2". Inside the tubular container 2, a thermo-mechanical converter with paraffin and piston 3 is placed

coaxially with the bimetallic band 1, fixed to the mentioned bonnet and sealed with another insertion 3'. The container 2 is filled with a thermo-conductor agent 4 consisting of paraffin, which facilitates the heat transmission from the container metallic wall to the two converter elements represented by the thermo-bimetallic band and the thermo-mechanical convertor with paraffin and Bourdon tube. At the container free tip, it is placed another thermo-mechanical actuator, with bilateral action, that consists of two Bourdon tubes 5 and 5', connected to the container by means of the collecting canals 6 and 6'.

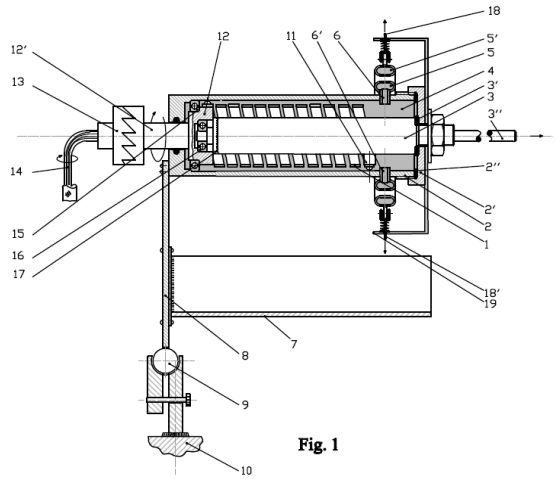

Fig. 4. *Longitudinal section through the heliothermic mixed actuator with cylindrical-parabolic concentrator* [2]

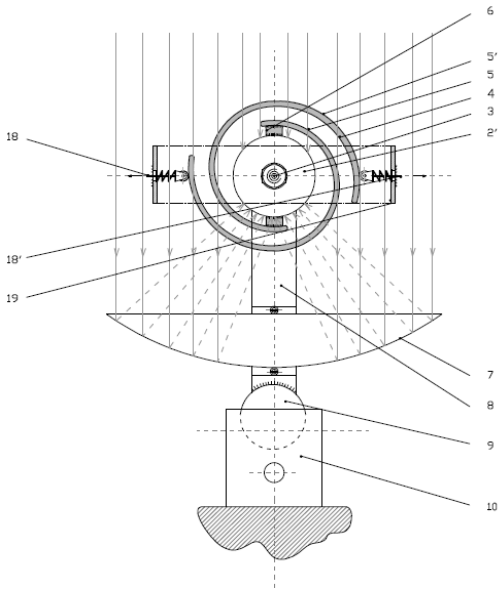

Fig. 5. *Transverse section through the heliothermic mixed actuator with cylindrical-parabolic concentrator* [2]

The cylindrical container is exposed to direct and reflected solar radiation through a cylindricalparabolic concentrator 7.

As previously mentioned, the thermo-bimetallic converter and the thermo-mechanical converter with paraffin and piston are placed within the container. One of the thermo-bimetallic band tips is fixed to the inner wall of the container 2 by means of a screw support 11. The other tip is fixed of a pap 12, which is integral with a rigid axle 12' provided in its extension with a flexible axle 14 which connects the thermo-bimetallic converter to the driven element, that is not represented in the figure.

The pap 12 is fixed in regard to the container 2 through a ball bearing 15, and in relation to the thermo-mechanical converter through the ball bearing 16 and the pap 17. The Bourdon tube deformation is transmitted to a bar with spool and spring 18 and 18' mounted in a support frame 19.

The system has the advantage of complete capitalization of the effects generated by changing the paraffin state of aggregation: using it as heat-transfer agent to a complete and fast excitation of the thermo-bimetallic converter and the thermo-mechanical converter placed coaxially within the first; the agent volume compensation and production of power and drive through the thermo-mechanical converter with Bourdon tubes.

4. Conclusions

1. The paper presents the authors' contributions to the development of solar actuators with bimetallic band and Bourdon tube in the EMAD Research Centre of "Ștefan cel Mare" University of Suceava.

2. One of the solutions achieved in the EMAD Research Center is the heliothermic mixed actuator made of a mechanical converter with thermo-bimetallic band associated with a thermo-mechanical converter with paraffin, both placed in a solar concentrator focusing point.

3. Another solution is the heliothermic mixed actuator with cylindrical parabolic concentrator that is made of a thermo-bimetallic converter associated with a thermo-mechanical converter with paraffin and piston together with a thermo-mechanical convertor with paraffin and Bourdon tube.

4. The solutions present a series of advantages, such as: an increased number of operable elements, construction simplicity, reduced gauge.

References

[1]. Cernomazu D., Poienar M., Romanescu A. N., Ţanţa O. M., Prodan C., Georgescu D. Ş., Niţan I., Olariu E. D., Ungureanu C., Raţă M., *Actuator heliotermic mixt*, Cerere de brevet de invenție nr A/00619 din 13.08.2014.

[2]. Cernomazu D., Poienar M., Romanescu A. N., Ţanţa O. M., Prodan C., Georgescu D. Ş., Niţan I., Olariu E. D., Ungureanu C., Raţă M., *Actuator heliotermic mixt cu concentrator parabolic*, Cerere de brevet de invenție nr A/00620 din 13.08.2014.

[3]. Romanescu A. N, Ţanţa O. M, Poienar M., Niţan I., Ungureanu C., Mandici L., Cernomazu D., *Current state of research at the EMAD Research Center from „Ştefan cel Mare" University in connection with actuators and solar motors with solid heating medium*, In: Analele Universității „Eftimie Murgu" Reşiţa, Fascicula de Inginerie, anul XXI, nr. 2, 2014, p. 123 – 134, ISSN: 1453-7397.

THE ANNALS OF "DUNAREA DE JOS" UNIVERSITY OF GALATI
FASCICLE IX. METALLURGY AND MATERIALS SCIENCE
Nº. 2 - 2015, ISSN 1453 – 083X

DUAL PRIORITY SCHEDULING ALGORITHM USED IN THE nMPRA MICROCONTROLLERS – DYNAMIC SCHEDULER

Lucian ANDRIEȘ, Vasile Gheorghiță GĂITAN
Faculty of Electrical Engineering and Computer Science
"Ștefan cel Mare" University of Suceava
Suceava, Romania
e-mail: andries.lucian2002ro@gmail.com, gaitan@eed.usv.ro

ABSTRACT

This paper is a follow up of an already published paper that described the static scheduler. It deals with a true dynamic scheduling algorithm that is meant to maximize the CPU utilization. The dual priority algorithm is composed of two different scheduling algorithms, earliest deadline first (EDF) and round robin (RR). We have chosen EDF, because it is a dynamic scheduling algorithm, used in real time operating systems, which can be easily implemented in hardware, by improving the nHSE architecture. The new dynamic scheduler algorithm provides a much better CPU utilization, very good switching time for tasks and events within 5 to 8 machine cycles and guarantees that no task will suffer from starvation.

KEYWORDS: real time system, dynamic hardware scheduler, microcontroller, pipeline processor

1. Introduction

In article [1], the author provides a review of the fundamental results of two important scheduling algorithms:

- *Fixed priority (FP - Fixed priority scheduling assumes that the processor will execute the highest priority task among others*).
- *Earliest deadline first* (EDF - Earliest deadline first scheduler is a real time operating system that places processes in a priority queue in order to be scheduled for execution).

The FP algorithm will be assigned a fixed priority that cannot be modified at run time or in the normal operations to each task, while the EDF algorithm is the opposite. Each priority of a task is continuously computed based on the earliest absolute deadline.

Other scheduling algorithms such as *Shortest Remaining Processing timer First* (SRPT) [2] and *Least Laxity first* (LLF) [3] are very powerful and efficient in software, but are difficult to implement in hardware because of the logical ports cost. For this reason we are going to explain in detail only the *EDF* algorithm.

The scheduling algorithms based on FP and EDF, to a certain extent, are good algorithms that can be used in real time operating systems. But in the majority of the commercial real time operating systems, the FP algorithm is implemented due to the simplicity and lower overhead of resources.

The overheads are more visible in software, because EDF can be implemented in different ways that can deal with more or less resources. Each software implementation can lead to more or less CPU utilization.

The hardware resources that are going to be used are not going to increase drastically by EDF, because the Scheduler described in [4] will not be changed at all and the nHSE architecture, described in [6-9], will undergo minor improvements.

The nHSE architecture, described in [8], can support two types of schedulers, namely static or dynamic. So far only the static scheduler has been described and implemented in paper [4], while the dynamic scheduler has been postponed for future implementations.

This paper will present only the theoretical part behind the actual hardware implementation [4]. Based on our experience with the static scheduler, we are convinced that the scheduler will work as intended and the resource utilization will not be much higher.

This paper is organized as follows. The improvements of the nHSE architecture is presented in Section III, the proposed dynamic dual priority algorithm is presented in Section III, followed by the results in Section IV. In the end, in Section V, some conclusions are listed.

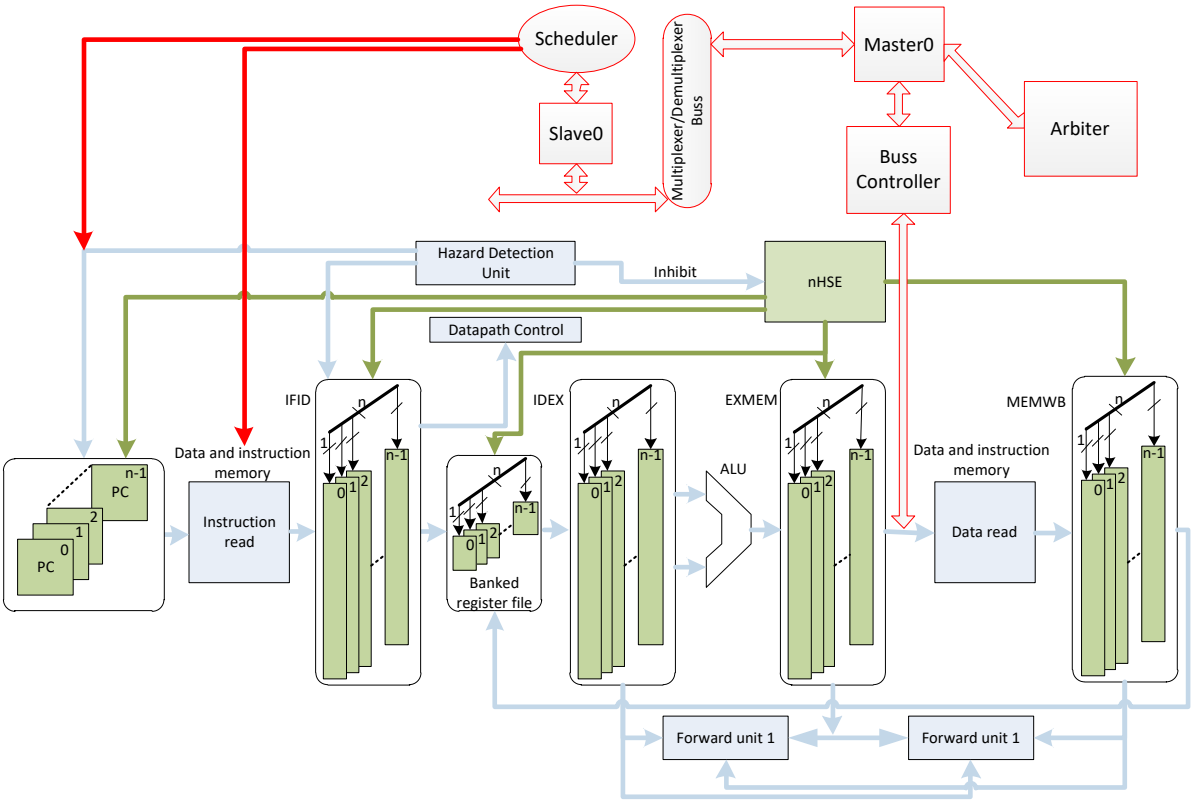

Fig. 1. *The nMPRA architecture*

2. nMPRA architecture overview

This paper starts with an overview of the nMPRA architecture. In Figure 1, the initial nMRPA architecture [8] is described, while the representations colored in red are the improvements described in [4].

To the current nMPRA architecture [8], was added a slow bus with a *Buss Controller* and a peripheral (Scheduler) which contained the scheduling algorithm (Figure 1).

This new approach optimizes the switching of the hardware tasks in terms of silicon costs and system complexity. During this process, we encounter some synchronization issues, caused by the current architecture of the processor, MIPS with 5 pipeline stages. In order to stop a working task, the Program Counter (PC) must be stopped. The switch process of a task is really simple and is done in two steps.

- Stop the PC from its current task.
- Select the appropriate task to share the resources.

From this description, we can think that the switching of a task can be done in 1 machine cycle, because the stopping of the PC and the selection of the appropriate input / output of the multiplexer / demultiplexer can be done simultaneously.

It could be true if there were no dependencies with the RAM and ALU that were shared. So when the *SelectTask[2..0]* bus (Figure 2) will have a different value, in order to select the new task, the ROM, ALU and ALU will no longer be available for the current task.

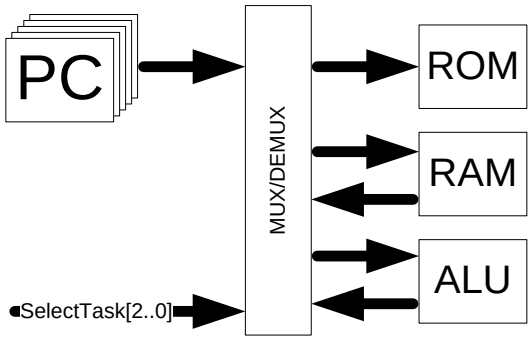

Fig. 2. *Simplified nMPRA architecture*

We have chosen to wait during 3 machine cycles to solve the synchronization issue. The other 2 machine cycles are used to synchronize the next task program counter address with the ROM memory and the instruction fetch pipeline register because the Scheduler and the program counter use 3 quadrature clock signals.

The whole architecture was designed using VHDL hardware description language (VHDL 93).

Altium Designer 2014 was used, only as a text editor, to include the individual VHDL module and to create the architecture. The design created was simulated using ModelSim Altera Started Edition 10.1d. The only stimuli applied to the microcontroller was 3 quadrature clock signals, while the ROM memory was already initialized with the machine code for all 5 tasks.

The following results were observed, in normal operation, at key points. In the following lines we are going to detail the steps required to do a task switch:

a) *var_process0ready* ((1) in Figure 3) signal represents the event occurring after the activation of the first task. Because no jump instruction is performed, all of the active tasks will be stopped with the help of *processXstall* (X will have values from 0 to 4) signal. The *process1ready* will remain active as a sign that the task is still active. At this moment task1 will be in the ITQ.

b) Wait one clock cycle.

c) *Processactiv* signal selects thread 0 as the active one (3) in Figure 3).

Process0resetstall and *process0startagain* signals are activated ((4) in Figure 3).

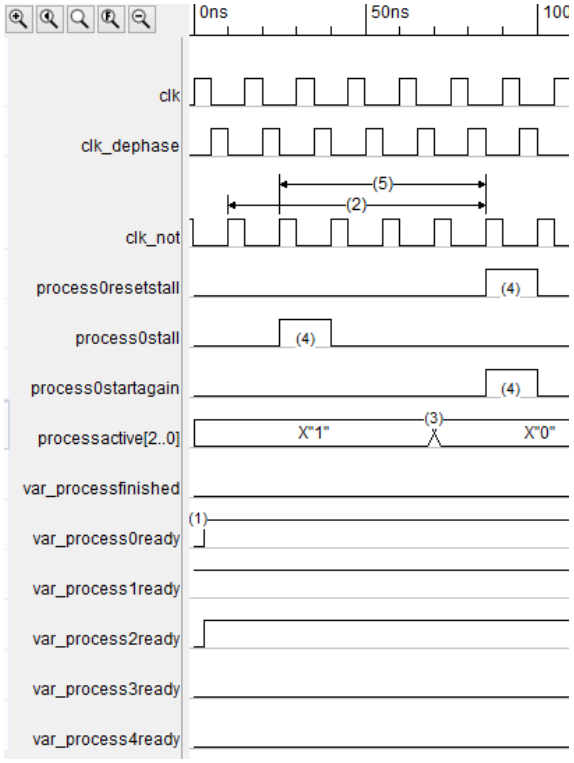

Fig. 3. *Time for a task switch*

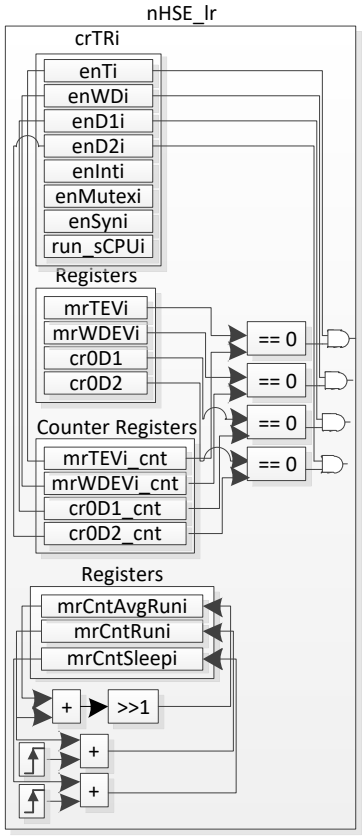

Fig. 4. *Local nHSE registers*

As we can see in Figure 3 the response time of the scheduler is one machine cycle (between (2) and (5)), the time spent after the task with higher priority becomes active and the starting of the executing code (between (2) and (5) in Figure 3) is done in 5 machine cycles in an interval of 75 ns, where the period of the clock is 15 ns.

3. nHSE Arhitecture Improvements

The architecture of the microcontroller that includes the nMPRA and nHSE architecture firstly described in [8] and then improved in [4] will be improved again in order for the nHSE architecture to make use of the dynamic scheduler.

nMRA architecture stands for n Multi Pipeline Register architecture which means that the most important resources, ROM, RAM, ALU, were shared between multiple hardware tasks.

nHSE architecture stands for "n Hardware Scheduler Engine" and can be used for real time preemptive capabilities of the static and of the dynamic scheduler. It also provides support for:

- Logic events:
  - Interruptions.
  - Events generated by watchdog timers.
  - Events generated by the timer.

- Events generated by the deadline1 timer.
- Events generated by the deadline2 timer.
- Events generated by mutexes.
- Events generated by synchronization events.

- Static Scheduler: The priorities of n tasks cannot be changed during execution.
- Dynamic Scheduler: The priorities of n tasks can be changed during execution.
- Global and local nHSE registers.

In order to support dynamic scheduling, the nHSE architecture was updated with a new register mrCntAvgRuni, added to the local nHSE registers (Figure 4) for all hardware tasks. The registers will always be equal to the average of the current task execution time. The register mrCntRuni will start to count each machine cycle only after the task has started again. At the end of the task execution the nHSE_lr will add the current value from mrCntRuni to mrCntAvgRun register and shift to the right result, in order to achieve a division by two. The final result will be stored in mrCntAvgRun.

In the following example, we are going to detail the operation performed by nHSE_lr in Table 1:

Table 1. *Average task computation for EDF algorithm*

Step	mrCntRuni	Operation	mrCntAvgRuni
1		mrCntAvgRuni = (mrCntRuni + rCntAvgRuni); mrCntAvgRuni =>> 1;	0
2	500	(500 + 0) >>1	250
3	700	(700 + 250) >>1	475
4	450	(450 + 475) >>1	462
5	900	(900 + 462) >>1	681
6	1000	(1000 + 681) >>1	840
7	1200	(1200 + 840) >>1	1020
8	300	(300 + 1020) >>1	660

As it can be easily seen, the average algorithm has started with the value of the register mrCntAvgRuni equal to 0. If we compute again the same task execution, but this time with floating point, the result will be approximately the same: an arithmetic average will be performed on the number of the processor cycles of the register mrCntAvgRuni from Table 1. The result is (500 + 700 + 450 + 900 + 1000 + 1200 + 200) / 7 = 721.4285714285714 machine cycles.

The difference between the unsigned average and the floating point average is just 61 machine cycles, which can be equal to 12 R type assembler instructions if we consider that an R type instruction is executed in 5 machine cycles.

From the examples above, we can say that the computation error for the unsigned average algorithm is 8.46% which is deducted with the following equation: 100% - (660 * 100) / 721 = 100% - 91.539% = 8.46%

The result 8.46 % indicates the maximum percentage that the unsigned average algorithm can have. The value of the error will decrease as the number of task recurrence increases.

The costs of hardware resources, per hardware task, for a true dynamic dual priority algorithm, are:

- One register of 32 bits.
- An add module;
- A shift to the right by one module.

4. The proposed dynamic dual priority algorithm

This paper is a follow up of the article [4], whose overview is presented in chapter II, where the presented dual priority scheduling algorithm was not a true dynamic scheduler because the dynamic execution of the algorithm was that the priority of the tasks was changed only when one or several tasks did not meet the Round Robin timer (RRB) time constraints.

The algorithm will behave like a true static scheduler only when the following requirements are met:

- The RRB time constrains are met.
- The sum of all concrete task executions is less than the lowest task recurrence.
- No task is going to be promoted to extend the execution tasks class (LTQ).

The main difference between the scheduling algorithm described in article [4] and the algorithm presented in this paper is the use of a true dynamic scheduling algorithm, namely earliest deadline first scheduling (EDF).

In this paper the switching time has not been improved since the last article [4], because we are presenting the other half of the Scheduler. In order to have a better understanding of the algorithm, we are

going to reuse and detail some of the information from [4].

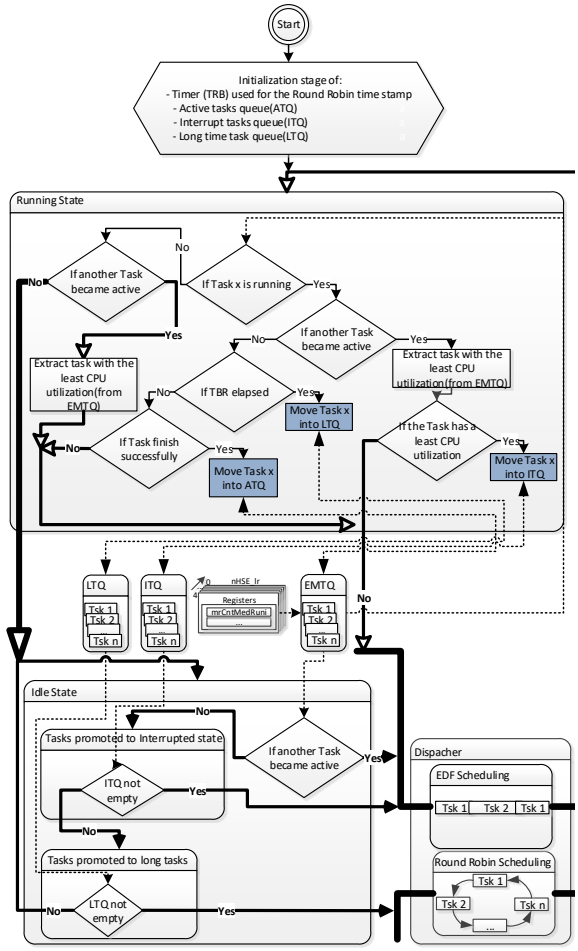

Fig. 5. *The flowchart of a scheduler with a dynamic dual priority algorithm (Figure 3 from [4])*

In the following lines, the classes that each task can belong to are presented:

- The class of execution medium time queue, which has the highest priority (the tasks will be inserted by the medium execution time (EMTQ)), will schedule the tasks, based on medium execution time, only in the Running State (RS) of the Scheduler.
- The class of interrupted tasks, which has the second priority (the tasks will be inserted only in the interrupted task queue (ITQ)), will schedule the tasks, based on priorities, only in the Idle State (IS) of the Scheduler.
- The long execution tasks class (these tasks significantly exceed the base period T corresponding to the priority task), which has the least priorities (the tasks will be inserted only in the long task queue (LTQ)), will schedule the tasks, based on ROUND ROBIN (RR) algorithm, only in the Idle State (IS) of the Scheduler.

A global timer, Round Robin timer (TRB), is used to verify if the active time of the current task is not taking too long. If the TRB expires, the current task will be promoted to LTQ and will be scheduled based on RR algorithm.

The TRB must be initialized with the occurrence of the slowest task from the system or less. In Figure 5 is presented the operational flowchart of the dynamic Scheduler (event driven), which is driven by the main clock signal of the processor.

The operation of the Scheduler is exactly the same as in paper [4] whose overview is presented in chapter II, with the main difference that the EDF algorithm will guarantee a better control process unit (CPU) utilization.

5. Conclusions

The current paper presented the true dynamic dual priority algorithm which is the other part of the nHSE architecture, which uses the EDF algorithm for better CPU utilization.

The EDF algorithm will not be efficient in the following cases:

- The execution time of each task is greater than the TRB. In this particular case, only the RR algorithm will be used.
- The execution time of all tasks is less than the time recurrence of the fastest task. This precondition must be achieved in a system where the CPU load is normal.

The EDF algorithm will be efficient by scheduling the tasks whose execution is more likely to be over before another task becomes active, only when the CPU load rises above normal utilization.

The algorithm, shown in Figure 5, will ensure a constant of 5 machine cycles for each switch task and the guaranties that the tasks will be scheduled no matter how difficult the requirements of the system have been.

Acknowledgement

This paper was supported by the project "Sustainable performance in doctoral and post-doctoral research PERFORM - Contract no. POSDRU/159/1.5/S/138963", project co-funded from European Social Fund through Sectorial Operational Program Human Resources 2007-2013.

References

[1]. Robert I. Davis, *A review of fixed priority and EDF scheduling for hard real-time uniprocessor systems*, Real-Time

Systems Research Group, Department of Compuyter Science, University of York, York, UK.

[2]. Davis R. I., Burns A., Walker W., *Guaranteeing Timing Constraints Under Shortest Remaining Processing Time Scheduling*. In proceedings of the Euromicro Workshop on Real - Time Systems, p. 88-93, 1997.

[3]. Shaohua Teng, Wei Zhang, Haibin Zhu, Xiufen Fu, Jiangyi Su, Baoliang Cui, *A Least-Laxity-First Scheduling Algorithm of Variable Time Slice for Periodic Tasks*, International Journal of Software Science and Computational Intelligence, Vol. 2, Issue 2, April 2010.

[4]. Lucian Andries, Vasile Gheorghita Gaitan, *Dual Priority Scheduling algorithm used in the nMPRA Microcontrollers*, 18th International Conference on System Theory, Control and Computing, Sinaia, Romania, October 17-19, 2015.

[5]. Lucian Andries, Vasile Gheorghita Gaitan, *Detailed Microcontroller Architecture based on a Hardware Scheduler Engine and Independent Pipeline Registers*, 19th International Conference on System Theory, Control and Computing, Sinaia, Romania, October 17-19, 2014, ISBN 978-1-4799-4602-0, 2014.

[6]. Dodiu E., Gaitan V. G., *Custom designed CPU architecture based on a hardware scheduler and independent pipeline registers – concept and theory of operation*, IEEE EIT International Conference on Electro-Information Technology, Indianapolis, IN, USA, 6-8 May 2012.

[7]. Dodiu E., Gaitan V. G., Graur A., *Custom designed CPU architecture based on a hardware scheduler and independent pipeline registers – architecture description*, IEEE 35th Jubilee International Convention on Information and Communication Technology, Electronics and Microelectronics, Croatia, May 2012.

[8]. Gaitan V. G., Gaitan N. C., Ungurean I., *CPU Arhitecture based on a Hardware Scheduler and Independent Pipeline Registers*, IEEE Transactions on VLSI System, 2014, ISSN :1063-8210.

[9]. Gaitan N., Lucian A., *Using Dual Priority Scheduling to Improve the Resource Utilization in the nMPRA Microcontrollers*, IEEE 12th International Conference on Development and Application Systems, Suceava, Romania, May 15-17, 2014.

THE ANNALS OF "DUNAREA DE JOS" UNIVERSITY OF GALATI
FASCICLE IX. METALLURGY AND MATERIALS SCIENCE
Nº. 2 - 2015, ISSN 1453 – 083X

WATER-IN-DIESEL EMULSIONS AS AN ALTERNATIVE FUEL FOR DIESEL ENGINES. PART II: PERFORMANCE OF DIESEL ENGINES FUELED WITH WATER-IN-DIESEL EMULSIONS. A LITERATURE REVIEW

Vlad VRABIE*, Dan SCARPETE, Bianca Elena CHIOSA
„Dunarea de Jos" University of Galati, Faculty of Engineering, 47 Domnească Street, RO-800008, Galati, Romania
* Corresponding author
e-mail: vlad.vrabie@ugal.ro

ABSTRACT

This paper presents the recent advances of water-in-diesel emulsion fuel studies, especially the impact of using this emulsion fuel to the performance and emissions of diesel engine. Studies revealed that the onset and the strength of micro-explosion process give strong effect with regard to the combustion efficiency inside the combustion chamber.

Most of the researchers tested emulsions with water content of 5-40% in diesel fuel. Some studies concluded that 20% water in the emulsion fuel gives the optimum engine performance. Many researchers and experts agree that the reason why there is a slight drop in brake power and torque is the fact that water-in-diesel emulsion fuel has a lower heating value than a neat diesel fuel, thus less energy is released during combustion.

In general, the results suggest that the water emulsification has a potential to slightly improve the brake efficiency and to significantly reduce the formation of NO_x, soot, hydrocarbons and PM in the diesel engine.

Some factors may affect the experimental results that need to be considered, such as the effect of volatility of the base fuel, the water content of the emulsion, emulsion stability, ambient temperature, pressure, type of surfactant and engine test conditions: engine load, speed, injection timing and compression ratio.

KEYWORDS: water-in-diesel emulsion, performance, emissions, diesel engine, combustion

1. Introduction

Diesel engines have been used in heavy duty applications for a long time [1] and, nowadays, more and more attention is paid to diesel engines in transportation, industrial and agricultural applications due to their high efficiency and reliability [2].

A good fuel for diesel engine should bear characteristic features such as short ignition lag, sufficiently high cetane rating in order to avoid knocking, suitably volatile in the operating range temperatures for good mixing and combustion, easy startup characteristics, limited smoke and odor, suitable viscosity for the fueling system, free from corrosion and wear, and ease of handling [3].

Higher fuel efficiency in the diesel engine is achieved due to the high compression ratios along with relatively high oxygen concentration in the combustion chamber [4].

The introduction of water prolongs the ignition delay, increases the amount of fuel burned and the rate of heat released in the kinetic burning period. In the diffusive burning period, the temperature is generally lower in the cylinder when water is added. The change in the maximum cylinder pressure is insignificant [5].

Primary pollutants emitted from diesel engines are particulate matters (PM), black smoke, nitrogen oxides (NO_x), sulphur oxides (SO_x), unburned hydrocarbon (HC), carbonmonoxide (CO), and carbon dioxide (CO_2) [6].

Water-in-diesel emulsions are fuels for regular diesel engines. The advantages of an emulsion fuel are the reductions in the emissions of nitrogen oxides

and particulate matters, which are both health hazardous, and the reduction in fuel consumption due to better burning efficiency. An important aspect is that diesel emulsions can be used without engine modifications [7].

Most emulsions are not thermodynamically stable, but as a practical matter, quite stable emulsions can occur that resist demulsification treatments and may be stable for weeks / months / years. Most meta-stable emulsions that will be encountered in practice contain oil, water and an emulsifying agent (or stabilizer) which is usually a surfactant, a macro-molecule, or finely divided solids [8].

This review presents the influence of water-in-diesel emulsion on the diesel engine performance and the effects of water-in-diesel emulsion fuel on combustion process and emissions.

2. Combustion process

The combustion process is generally characterized by factors such as injection characteristics, spray penetration, evaporation, chemical and physical atomization and mixture ignition, engine cylinder pressure and temperature, and heat release characteristics. Figure 2 presents the primary and secondary atomization in spray flame of an emulsified fuel [6].

The interest in water-in-diesel emulsions derives from the fact that water in the form of micrometer-sized droplets exerts some positive effects on the combustion of fuels. When an emulsion fuel is heated, the water droplets are vaporized first because water is more volatile than diesel under superheat conditions. The vaporization of water will cause the „explosion" of the continuous hydrocarbon phase.

This phenomenon, known as micro-explosion, helps in the atomization of fuel, accelerating fuel evaporation rate and enhancing fuel-air mixing process, thereby improving the process [1].

Micro-explosion is an important phenomenon in the secondary atomization process of water-in-diesel emulsion fuels. Generally, this phenomenon is affected by volatility of base fuel, type of emulsion, water content, diameter of the dispersed liquid, location of the dispersed liquid and ambient conditions like pressure and temperature [6].

Sheng, Zhang and Wu [9] observed that the water dots of 0.001 mm in emulsion droplets can be recognized and a no-water layer is found near the surface of the droplet (Figure 1). The micro-explosion can hardly be observed below 733 K. At 823 K, the explosion takes place early and is slightly weaker. In lower gas pressure cases, the velocity of torn fragments of droplets after explosion is much higher than that in higher gas pressure, due to lower gas density.

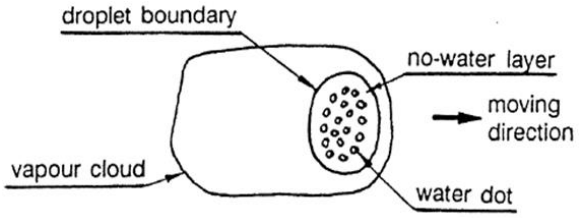

Fig. 1. *Micro-structure of the vaporing emulsion droplet* [9]

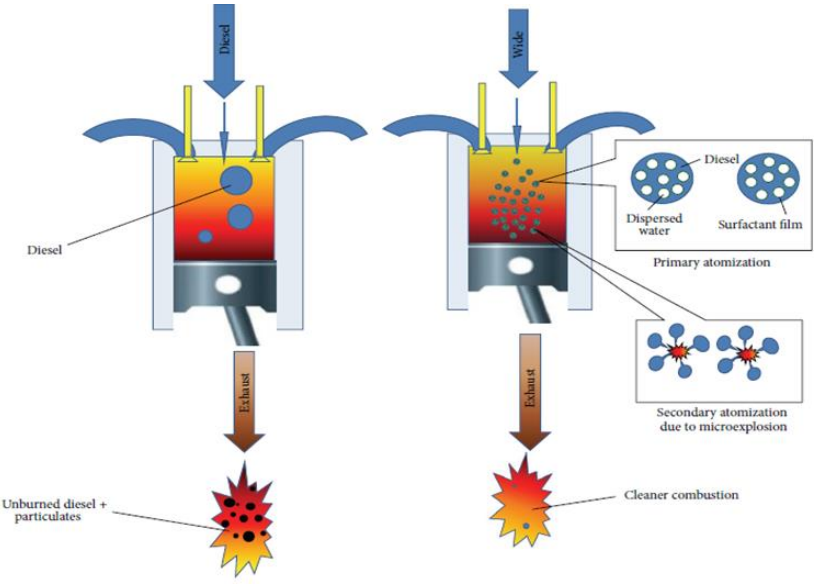

Fig. 2. *Primary and secondary atomization in spray flame of emulsified fuel* [6]

The study of the combustion process was difficult to perform since there has not been any optical access to the combustion chamber. As a result, more focus was given to the cylinder and thermocouple readings for the engine wall and inlet and exhaust temperatures to study the performance of combustion [6].

The temperature in the combustion chamber is the key factor for the utilization of emulsion. Micro-emulsion will take place in a certain temperature range and becomes stronger at a proper temperature. Higher pressure in the combustion chamber has little effect on the occurrence of the explosion, but the penetration of fragments of torn droplets will be much lower due to the denser gas in the combustion chamber. This gas may weaken the effect of micro-explosion on the improvement of air-fuel mixing. The explosion will take place more easily for larger initial droplet diameters. The energy of explosion is strong enough to emit fragments of torn droplets to a distance several millimeters away from the spray boundary, if the gas temperature is suitable [9].

3. Performance of diesel engine fueled with water-in-diesel emulsions

Fahd *et al.* [10] investigated the effect of 10% water emulsion diesel (ED10) on the engine performance and emission characteristics and the results were compared to the base diesel fuel (Euro 4). The experiments were performed in a four-cylinder 2.5 L DI turbocharged Toyota diesel engine at four different engine loading conditions (25%, 50%, 75% and 100% load) in order to analyze the effect of emulsion diesel over the entire engine load condition. For each load, the engine speed was varied from 800 rpm to 3600 rpm in steps of 400 rpm. The water-in-diesel emulsion (ED10) produces less output power and engine efficiency as compared to neat diesel fuel (Figure 3). Besides these, W/D E10% shows higher brake specific fuel consumption (BSFC) for all engine operating conditions (Figure 4).

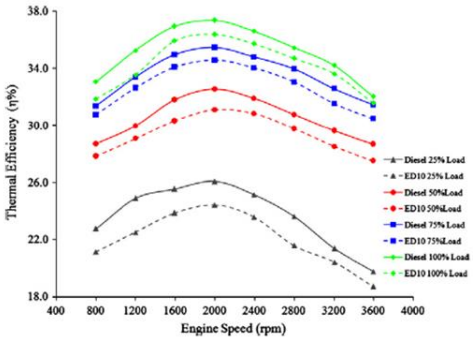

Fig. 3. *Thermal efficiencies for diesel and ED10 fuel vs engine speed and load* [10]

Reduction in exhaust gas temperature is observed for ED10 fuel and at higher engine load conditions. In addition, ED10 demonstrates lower NO emission at all load conditions and higher CO emission at low load and low speed condition which eventually gets significantly reduced at higher engine speed.

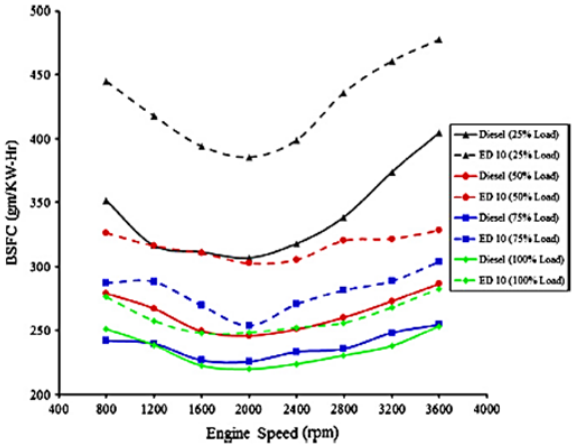

Fig. 4. *Brake specific fuel consumption for diesel and ED10 fuels vs engine speed and load* [10]

Armas *et al.* [11] investigated the effect of water–oil emulsions on the engine performance and on the main pollutant emissions, NO_x, total hydrocarbons (THC), soot, particulate matter (PM) and its composition. Renault F8Q turbocharged intercooler IDI Diesel engine was tested under five different steady state operating conditions, selected from the transient cycle for light duty vehicles established in the European Emission Directive 70/220. Tests were performed using a commercial fuel as a reference and an emulsified fuel (water-in-diesel emulsion with 10% water percentage and with the surfactants recommended by Repsol-YPF company – polyethylene glycolemonoleate and sorbitol-esesquioleate) for each operating condition.

The results reported here suggest that the water emulsification has the potential to slightly improve the fuel consumption, the brake efficiency and to significantly reduce the formation of thermal NO, soot, hydrocarbons and PM in the diesel engine [11].

Suresh et al. [12] investigated the emissions and performance characteristics of a four-stroke diesel engine operating on water in diesel emulsified fuels and its CFD (Computational Fluid Dynamics) analysis of NO_x emission. Emulsion fuels with varying contents of water in diesel (5%, 10%, 15% and 20%) are prepared and stabilized by sorbitan-monooleate surfactant. The experimental results reveal that 20% water-in-diesel reduces 45% of NO_x emission. Figure 5 presents the brake power versus

NO_x and it is observed that water-in-diesel fuel with 20% water registers the lowest values of NO_x.

The exhaust gas temperature and smoke emissions are drastically reduced for the emulsion fuels compared to the pure diesel. When water is added to diesel fuel, brake thermal efficiency is slightly reduced. It is acceptable if we are to consider the NO_x emissions characteristics.

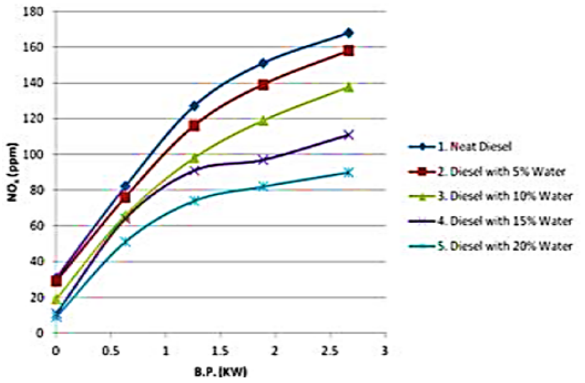

Fig. 5. *NO_x emission vs brake power* [12]

According to a report by Sadler [13], an application of 13% water content (not mentioned whether by volume or mass percentage) in the emulsified fuel in UK has brought 13% and 25% reduction of NO_x and PM, respectively.

Ahmad et al. [14] investigated the effect of water-in-diesel emulsion fuel (W/D) originating from low-grade diesel fuel (D2) on the combustion performance and emission characteristics of a direct injection diesel engine under varying engine loads (25–100%) and constant engine speed (3000 rpm). Four types of W/D are tested, which consist of different water percentages (5%, 10%, 15% and 20%), with a constant concentration of 2% of surfactant and labeled as E5, E10, E15 and E20, respectively. It is observed that NO_x (Figure 6) and PM (Figure 7) are found to be reduced for all types of W/D.

The carbon monoxide (CO) and carbon dioxide (CO_2) emissions increase compared to D2 at low load and high load, respectively. E20 is reported to be the best in reducing NO_x and PM with an average reduction of 41% and 35%, respectively, in every load condition.

Attia and Kulchitskiy [15] studied the effect of the structure of water-in-diesel fuel emulsion (WFE) on a three-cylinder diesel engine performance. Based on membrane emulsification, two different membranes of pore sizes of 0.2 µm and 0.45 µm have been individually used to change the emulsion structure while keeping the same WFE volumetric content (at 17% water volumetric content and 0.5% mixing emulsifier content). The results showed that emulsions with large size of water droplets resulted in greater reduction of NO_x emissions up to 25%, while emulsions with finer droplets not only gave reductions in engine smoke and unburned hydrocarbons of values greater than 80% and 35% respectively, but also resulted in an increase of the engine effective efficiency up to 20%.

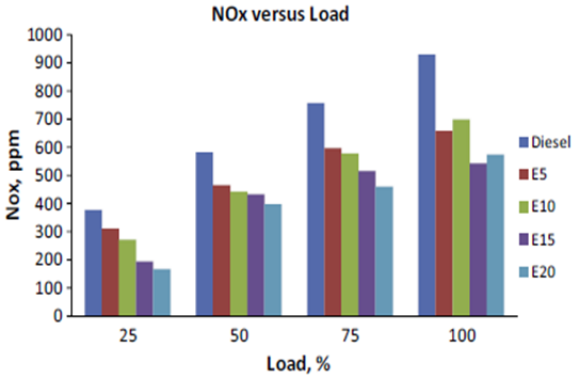

Fig. 6. *Formation of PM for D2 and W/D (E5, E10, E15 and E 20) under varied loads (25%, 50%, 75% and 100%)* [14]

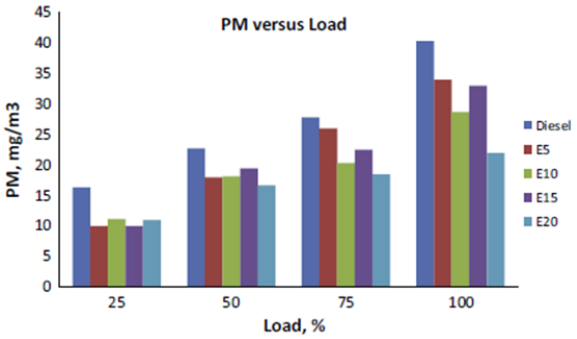

Fig. 7. *Formation of NO_x for D2 and W/D (E5, E10, E15 and E 20) under varied loads (25%, 50%, 75% and 100%)* [14]

Alahmer [16] investigated the effect of emulsified diesel fuel on the engine performance and on the main pollutant emissions for a water-cooled, four-stroke, four cylinders, and direct injection diesel engine. Emulsified diesel fuels with water content in the of range 0-30% by volume were used. The experiments were conducted in the speed range from 1000 to 3000 rpm. While the brake specific fuel consumption (BSFC) has a minimum value at 5% water content and 2000 rpm, the torque, the break mean effective pressure and thermal efficiency (Figure 8) are found to have maximum values under these conditions. The emission of CO_2 was found to increase with engine speed and to decrease with water content. NO_x produced from emulsified fuel is significantly less than NOx produced from pure diesel

under the same conditions (Figure 9), and as the percentage of water content in the emulsion increases, the emitted amount of oxygen also increases.

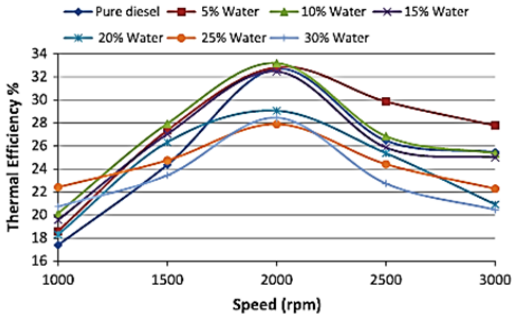

Fig.8. *Thermal efficiencies for pure diesel, 5%, 10%, 15%, 20%, 25% and 30% water addition* [16]

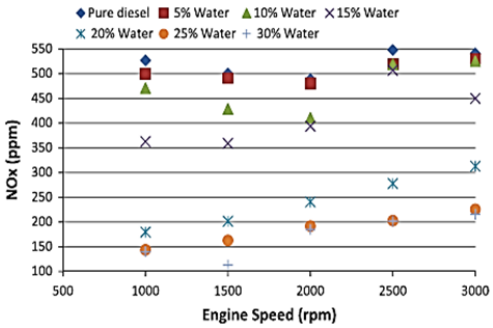

Fig. 9. *NO_x emission for pure diesel, 5%, 10%, 15%, 20%, 25% and 30% water addition* [16]

It was found that, in general, the use of emulsified fuel improves the engine performance and reduces emissions [16].

Canfield [17] examined the effects of combusting a mixture of diesel fuel, water, and surfactant on the nitrogen oxides (NO_x) emissions from a compression ignition diesel engine. The data shows significant NO_x emission reduction with up to 45% water, by volume, in the fuel. These results are correlated with the first thermodynamic law and equilibrium combustion products analyses to estimate the adiabatic flame temperature of the standard fuel and fuel-water emulsion cases. Results indicate that thermal NO_x is indeed reduced by quenching and flame temperature suppression, confirming the reports in the literature. Recommendations are given for further studies, including improving the fuel-water emulsion and considerations for long-term testing.

Ghojel and coworkers [18] reported 29-37% reduction of NO_x emissions when operating on diesel oil emulsion of 13% water content by volume.

Samec *et al.* reported a reduction of 20% and 18% NO_x emission compared to pure diesel fuel with 10% and 15% water content in the emulsion, respectively [19, 20].

Barnes *et al.* [21] investigated the effect of water blended fuel on the performance and emissions of a city bus engine considering 10% water content by volume. They showed a decrease of NO_x with 9% in comparison with the use of neat diesel fuel.

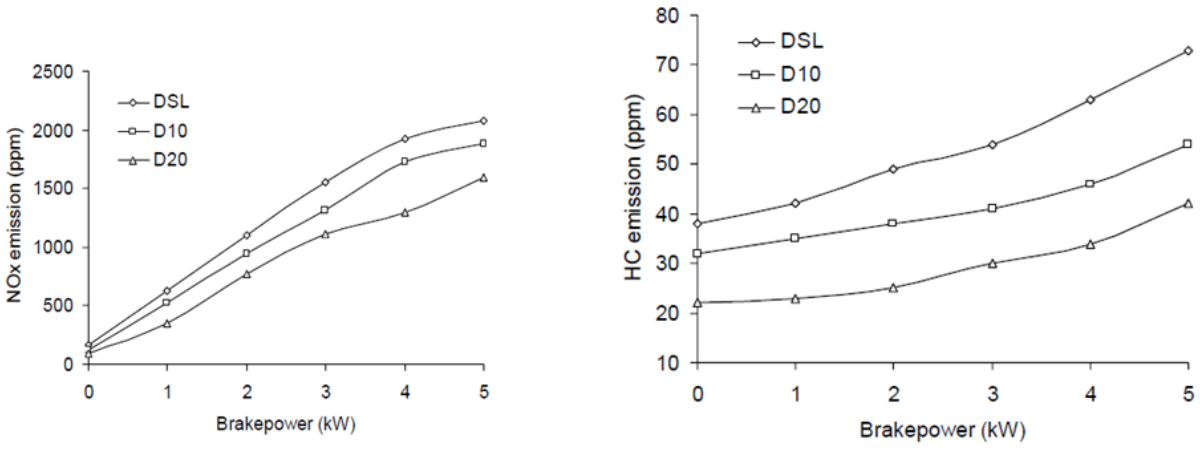

Fig. 10. *NO_x emission (left) and HC emission (right) vs brake power* [22]

Kanaan and Udayakumar [22] studied the effect of water emulsified diesel fuel combustion on brake thermal efficiency, brake specific fuel consumption and NO_x and hydrocarbon emissions in a diesel engine. The experiments were conducted on a single cylinder Kirloskar with direct injection and four-stroke cycle diesel engine at constant speed of 1500 rpm with a fuel injection pressure of 200 bars. The aim of the experimental study was to investigate the effect of diesel (DSL), diesel with 10% water (D10)

and diesel with 20% water (D20) on performance and emission in a light duty single cylinder diesel engine.

The water emulsified diesel fuel was prepared by mixing 10% and 20% of distilled water with 90% and 80% of diesel by volume, respectively. Sodium lauryl sulphate was used as surfactant to prepare the emulsion. Sodium lauryl sulphate (0.1%) is added with 100 ml and 200 ml distilled water and mixed with 900 ml and 800 ml diesel to prepare D10 and D20 emulsified diesel fuels, respectively. The mixer was stirred for 2-3 minutes in an electrically operated agitator. As the amount of water in the emulsion increases, the brake thermal efficiency increases. The presence of water in the emulsion increases the expansion work and reduces the compression work resulting in increased net work done during the cycle [22].

The NO_x (Figure 12, left) and hydrocarbon (Figure 12, right) emissions were found to decrease with the increase in water percentage (until 20%) in the emulsified diesel [22].

Nadeem *et al.* [23] studied water-in-diesel emulsion with conventional (sorbitanmonooleate) and gemini surfactants for main pollutant emissions by fuelling it in a four-stroke and four-cylinder engine test bed and concluded that, for 15% water content, there is 71% reduction in PM emission with Gemini surfactant water in diesel emulsion fuel. Emulsified fuels containing 5-15% water contents were prepared using conventional and gemini surfactants and studied in an engine bed XLD 418 (Ford, four strokes, four cylinders, water-cooled, compression ratio: 21.50, total displacement volume: 1753 cc and a maximum output brake horsepower: 60.0 at 4800 rpm) to clarify the changes in the main pollutant emissions (NO_x, CO and PM). The emission of NO_x, CO and PM was reduced using the emulsified fuels instead of neat diesel. The emulsified fuels containing gemini surfactant were the most prominent in the reduction of PM.

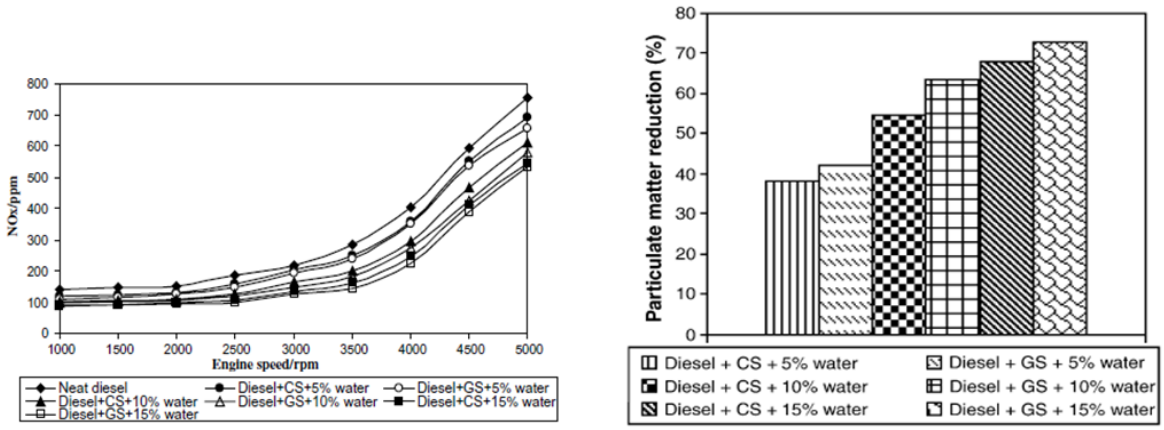

Fig. 11. *NO_x emission (left) and articulate matter emission (right) from neat diesel and emulsified fuels* [23]

In addition, emulsion fuels have higher specific fuel consumption and produce less torque, power and brake mean effective pressure but the difference is insignificant. Water emulsification has a potential to significantly reduce the formation of thermal NO_x (Figure 11, left), CO, SO_x, soot, hydrocarbons and PM (Figure 11, right) in diesel engines [23].

4. Conclusion

Diesel engines have been used in heavy duty applications for a long time and, nowadays, diesel engines are getting more and more attention in transportation, industrial and agricultural applications due to their high efficiency and reliability.

Primary pollutants emitted from diesel engines are particulate matters (PM), black smoke, nitrogen oxides (NO_x), sulphur oxides (SO_x), unburned hydrocarbon (HC), carbon monoxide (CO), and carbon dioxide (CO_2).

The combustion process is generally characterized by factors such as injection characteristics, spray penetration, evaporation, chemical and physical atomization and mixture ignition, engine cylinder pressure and temperature, and heat release characteristics.

Water-in-diesel emulsions are fuels for regular diesel engines.

The research studies were mainly focused on specific engine operation variables and, because of these results, it has become very difficult to draw a general conclusion. The results reported by different researchers are often conflicting, sometimes

generating results that are even worse than pure diesel.

Many researchers have concluded that a W/D emulsion fuel with water content of up to 20% can reduce:

- NO_x emissions by up to 45% (in Suresh's experiment), and in most cases up to 20%, compared to standard diesel fuel;

- Emissions of PM, HC and soot with significant percentages compared to standard diesel.

Some characteristics, such as the water percentage, dispersed droplet size and viscosity depending on the engine working conditions, such as engine load and speed, would be an interesting research area that can be explored fundamentally and practically in the near future.

The proven benefit of the water emulsified diesel is that the heat absorption by water vaporization causes a decrease of local adiabatic flame temperature and therefore reduces the chemical reaction in gas phase to produce thermal NO. The fuel with a larger emulsion ratio results in a longer ignition delay and a longer premixed combustion phase. A higher content of water weakens luminous flames and reduces the peak temperature in the diffusion controlled combustion phase and leads to a lower peak pressure and a lower level of NO_x emission.

With the advantage of the energy saving and less environmental pollution for W/D emulsion, together with the newly developed emulsion fuel making device, it will provide a great contribution to the industries, and, at the same time, will reduce the consumption of energy and ensure less pollution to the environment.

Furthermore, it requires a lot of studies and experimental work on the optimization of water content in the emulsion for best engine performance and low emissions so that the best recommendations could be given for the commercialization of water- in-diesel emulsion as an alternative source of energy for future diesel engines.

Acknowledgement

The authors would like to acknowledge the Project POSDRU/159/1.5/S/132397 for the financial support in carrying out the research work and in publishing this paper.

References

[1]. Yang W. M. *et al.*, *Impact of emulsion fuel with nano-organic additives on the performance of diesel engine*, Applied Energy, 112, 2013, p. 1206-1212.

[2]. Heywood J. B., *Internal combustion engine fundamentals*, McGraw-Hill, 1988.

[3]. Ganesan V., *Internal Combustion Engines*, Tata McGraw-Hill, NewDelhi, India, 1994.

[4]. Kannan K., Udayakumar M., *NOx and HC emission control using water emulsified diesel in single cylinder diesel engine*, ARPN Journal of Engineering and Applied Sciences, Vol. 4, No. 8, October 2009, ISSN 1819-6608.

[5]. Hsu B. D., *Combustion of water-in-diesel emulsion in an experiment medium speed diesel engine*, SAE, 860300. p. 2285-2295.

[6]. Khan M. Y. *et al.*, *Current trends in water-in-diesel emulsion as a fuel*, Hindawi Publishing Corporation The Scientific World Journal, Volume 2014, Article ID 527472, 15 pages.

[7]. Lif A., Holmberg K., *Water-in-diesel emulsions and related systems*, Advances in Colloid and Interface Science, 123-126, 2006, p. 231-239.

[8]. Laurier L., Schramm L., *Emulsions, Foams and Suspensions: Fundamentals and Applications*, Copyright@2005 Wiley-vch Verlag GmbH & Co, KGaA, Weinheim, ISBN: 3-527-30743.

[9]. Sheng H.-Z., Zhang Z.-P., Wu C.-K., *Study of atomization and micro-explosion of water-in-diesel fuel emulsion droplets in spray within a high temperature, high pressure bomb*, International Symposium COMODIA 90, p. 275-280, 1990.

[10]. Ebna M., Fahd A., *Experimental investigation of the performance and emission characteristics of direct injection diesel engine by water emulsion diesel under varying engine load condition*, Applied Energy, 102, 2013, p. 1042-1049.

[11]. Armas O. *et al.*, *Characterization of light duty Diesel engine pollutant emissions using water-emulsified fuel*, Fuel, 84, 2005, p. 1011-1018.

[12]. Suresh V. *et al.*, *Emission Characteristics of Diesel Engine using Water-in-Diesel Emulsified Fuel and its CFD Analysis*, International Journal of Applied Environmental Sciences, ISSN 0973-6077, Vol. 9, Number 5, 2014, p. 2739-2749.

[13]. Sadler L., *The airquality impact of water-diesel emulsion fuel (WDE) and selective catalytic reduction (SCR) technologies*, Mayor of London, London, UK, 2003.

[14]. Ithnin A. M. *et al.*, *Combustion performance and emission analysis of diesel engine fuelled with water-in-diesel emulsion fuel made from low-grade diesel fuel*, Energy Conversion and Management, 90, 2015, p. 375-382.

[15]. Attia A. M. A., Kulchitskiy A. R., *Influence of the structure of water-in-fuel emulsion on diesel engine performance*, Fuel, 116, 2014, p. 703-708.

[16]. Alahmer A., *Influence of using emulsified diesel fuel on the performance and pollutants emitted from diesel engine*, Energy Conversion and Management, 73, 2013, p. 361-369.

[17]. Canfield C. A., *Effects of diesel-water emulsion combustion on diesel engine NOx emissions [M.S. thesis]*, Mechanical Engineering, University of Florida, Gainesville, Fla, USA, 1999.

[18]. Ghojel J., Honnery D., Al-Khaleefi K., *Performance, emissions and heat release characteristics of direct injection diesel engine operating on diesel oil emulsion*, Applied Thermal Engineering, vol. 26, no. 17-18, p. 2132-2141, 2006.

[19]. Samec N., Kegl B., R. Dibble W., *Numerical and experiment-tal study of water/oil emulsified fuel combustion in a diesel engine*, Fuel, vol. 81, no. 16, p. 2035-2044, 2002.

[20]. Samec N., Dobovisek Z., Hribernik A., *The effect of water emulsified in diesel fuel on diesel fuel on exhaust emission*, Goriva i Maziva, vol. 39, p. 377-392, 2000.

[21]. Barnes A. *et al.*, *Evaluation of water-blend fuels in a city bus and an assessment of performance with emission control devices*, Proceedings of the Better air Quality Motor Vehicle Control &Technology, Workshop 2000.

[22]. Ithnin A. M. *et al.*, *An overview of utilizing water-in-diesel emulsion fuel in diesel engine and its potential research study*, Journal of the Energy Institute, 87, 2014, p. 273-288.

[23]. Nadeem M. *et al.*, *Diesel engine performance and emission evaluation using emulsified fuels stabilized by conventional and gemini surfactants*, Fuel, 85, 2006, p. 2111-2119.

THE ANNALS OF "DUNAREA DE JOS" UNIVERSITY OF GALATI
FASCICLE IX. METALLURGY AND MATERIALS SCIENCE
Nº. 2 - 2015, ISSN 1453 – 083X

STRENGTH ANALYSIS OF A COMPOSITE JOINT USED IN SHIP STRUCTURE

Florentina ROTARU*, Ionel CHIRICA, Elena Felicia BEZNEA
"Dunarea de Jos" University of Galati, Romania
e-mail: Florentina.Rotaru@ugal.ro, Ionel.Chirica@ugal.ro, Elena.Beznea@ugal.ro

ABSTRACT

Low weight and high strength panels are always taken into account when designing materials for sandwich panel technology, which offers an efficient solution for different problems. Different types of sandwich panels are currently being used depending on the applications. Honeycomb sandwich panels are a better solution in structural design problem. The work presented in the paper is focused on the study of the behaviour of a composite joint used in ship structure, loaded by transversal force. The components of the joint are sandwich plates, made out of core polypropylene honeycomb and extruded polystyrene and face sheets of the resin polymer. A typical sandwich panel is made of three layers, in which two thin sheets (faces) of a stiff and strong material are separated by a thick core of low-density materials (Allen, 1961). Considering the various uses of these materials in numerous fields, it is essential to know their mechanical properties so as to predict and calculate their behaviour in specific and diverse environments.

KEYWORDS: joint ship, sandwich composite, Ansys FEM, modeling

1. Introduction

The interest in using composites in various building structures has gradually increased. Nowadays, the idea of using sandwich construction has become more and more popular due to the new materials such as cellular materials which can be used as core for the sandwich. The idea of separation of the skins from the core is derived from the beam theory (sectional moment of inertia) [10].

The maritime and aerospace industries have used composite materials in order to reduce the total weight and for low fuel consumption. In the maritime field, the use of composites started in 1950 due to the low costs of GFRP **(**Glass fiber reinforced plastic) structures. The first applications include lifeboats, pleasure crafts and small yachts [11].

The merits of the sandwich composite structures are the high strength/weight ratio, heat resistance, sound / vibration insulation and easy assembly. In the last decades sandwich structures have been widely used in various fields: aerospace, automotive, ship building and construction industries (Yu and Cleghorn, 2005; Wang and Yang, 2000; Kim and Hwang, 2000). In maritime industry, sandwich composites are ideally suited for special structures [1, 2]. Foam cores meet the critical requirements of strength, buoyancy and low water absorption. Most applications include the construction of bulkheads, hulls, decks, transoms and furniture, but also, which is the most important, the strength structural elements. Considering the multiple uses of these materials in many fields, it is very important to know their mechanical properties in order to predict and calculate the structural behavior in specific and various environments.

One of the most used core materials is honeycomb because it has good properties such as: very high strength to weight ratio, electrically and thermally insulating material, chemically stable, good non-flammable (being self-extinguishing) and non-corrosion properties, shock and fatigue resistant. In nearly all sandwich constructions, certain types of joints have to be used for assembly, but little is known about their failure behavior. This paper deals with the investigation of joints used in shipbuilding and beyond.

2. Literature review

Peter Huson [7] (2012) analysed a joint similar to the combination described in this work but the materials used to sandwich the core were balsa wood and foam (General Plastics FR3707 structural foam core), skins used sheets CRFP (Carbon Fibre

Reinforced Plastic (polymer)) and for the carrier (triangle) balsa wood was used.

FR-3707 foams are chosen for applications in nuclear and hazardous waste extreme transportation. When used as a liner for IMPACT- as fire insulation in transport containers, FR-3707 can be designed to provide the ultimate protection against fire and collision for dangerous, surpassing wood and other polymeric materials. 3707-FR formulation is specifically designed to enable predictable impact-absorption performance under dynamic loading. At the same time, it provides intumescent char layer that insulates and protects hazardous materials, even when exposed to fire conditions. In Peter Huson's work were made more complex experimental tests and simulations using LS-Dyna program. Since impact tests were performed on these composites, quasi-static, dynamic strain and composite delamination were pursued.

Ch. Naresh [8] compared the response of Square and Hexagonal honeycomb sandwich panels in his paper entitled "Numerical Investigation into Effect of Cell Shape on the Behavior of Honeycomb Sandwich Panel". Numerical simulations using FE techniques are used for simulating the behavior of the sandwich panels under uniformly distributed loads. During simulation, two different combinations of materials (face material – core material) are considered. Based on the response, it is found that, although Al-Al sandwich panel with square honeycomb structure has lower stress values, it showed greater deflection than SS-Cu panel. Modal analysis is also executed to extract the natural frequencies. It is found that the square honeycomb panel has higher natural frequencies than those of the hexagonal honeycomb panel. This paper analyzes the natural frequency and the displacement for these sandwiches.

3. Problem definition

The purpose of this paper is to make a comparison between two materials that were used in the heart core of polypropylene honeycomb sandwich and extruded polystyrene, following the mechanical behaviour of the sandwich. The main steps in this study are:

1. Calculations using classical and finite elements methods for simple constructions with FEM package Ansys [9];
2. Understanding of properties of various face and core materials;
3. This is an analysis of the stiffness during the static test of sandwich panels and their components;
4. Analysis of the joint deflection behaviour;
5. Studying the behaviour of more cases with on joint application of different forces.

The materials used for sandwich are: for two skins Epoxy E Glass-Wet; for the core we used polypropylene honeycomb and extruded polystyrene. The geometry of these structures can be seen below in Figure 1.

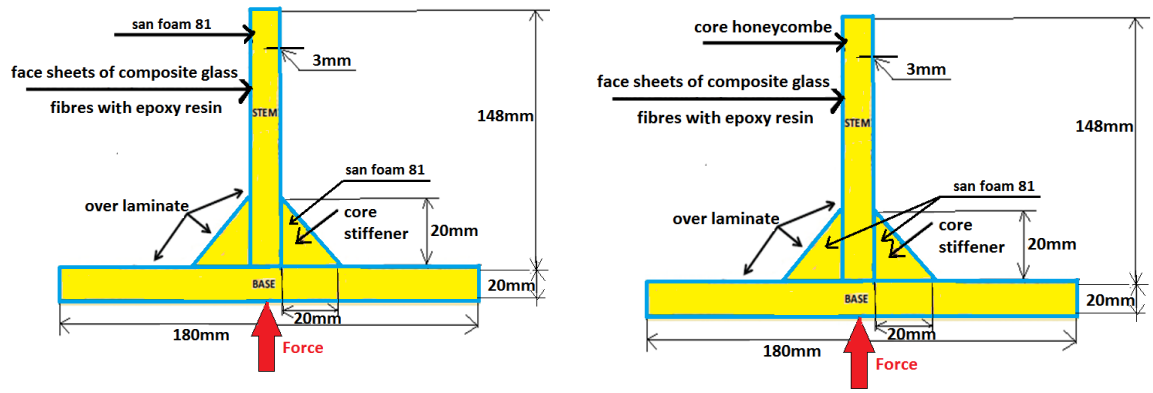

a) Composite joint with polypropylene honeycomb core b) Joint Composite San Foam core 81

***Fig. 1** Geometry Composite Joints and blunts are considered for review*

4. Meshing and boundary conditions

Geometric nonlinear static analysis has been done for the panels' models using ANSYS Workbench to determine the effect of the previouslymentioned parameters on the deflection as well as on stresses. The skins were modeled using SHELL with orthotropic properties, while SHELL was used for modeling the cores with isotropic properties. This model was able to accommodate both isotropic and orthotropic material properties, but isotropic material properties were initially applied to the model as reported in the present section. The loading and boundary conditions were adapted.

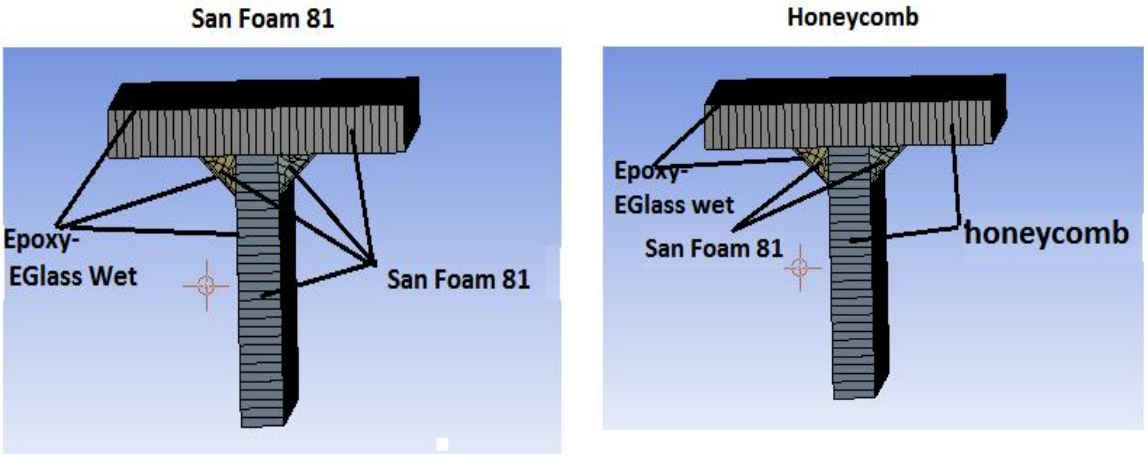

a) Case1, Joint with core Honeycomb b) Case 2, Joint with San Foam 81

Fig. 2. *Meshed models*

The materials used for the analysis of the two cases are presented in the tables below:

Table 1. *Honeycomb polypropylene* [Source: From ANSYS library]

Honeycomb properties	**Value**	**Unit**
Density	80	Kg/m^3
Orthotropic elasticity		
Young's Modulus Ex	1	MPa
Young's Modulus Ey	1	MPa
Young's Modulus Ez	255	MPa
Poisson's Ratio υ_{xy}	0.49	
Poisson's Ratio υ_{yz}	0.001	
Poisson's Ratio υ_{xz}	0.001	
Shear Modulus Gxy	10^{-6}	MPa
Shear Modulus Gyz	37	MPa
Shear Modulus Gxz	70	MPa

For skin using Mechanical Properties of the Epoxy-E Glass-Wet [Source: From ANSYS library]
Density =1850 Kgm^3
Young's Modulus x = 3500 Mpa
Young's Modulus y = 9000 Mpa
Young's Modulus y = 9000 Mpa
Poisson's Ratio xy= 0.28
Poisson's Ratio xy= 0.4
Poisson's Ratio xz= 0.2

Table 2. *SAN_Foam_81* [Source: From ANSYS library]

SAN_Foam_81kgm^3 Isotropic Elasticity		
Young's Modulus	60	MPa
Poisson's Ratio	0.3	
Bulk Modulus	50	MPa
Shear Modulus	22.077	MPa
Density	81	Kg/m^3

5. Results and discussions

As mentioned earlier, for the static analysis with uniformly distributed load from 2 KN – 27 KN, the panels used are executed on models of the two structures.

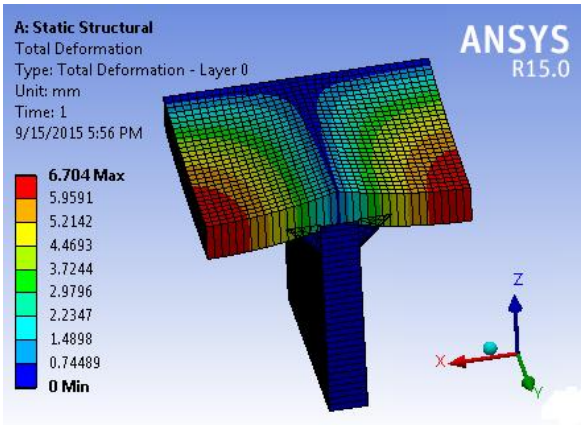

Fig. 3. *Total Deformation of the structure*

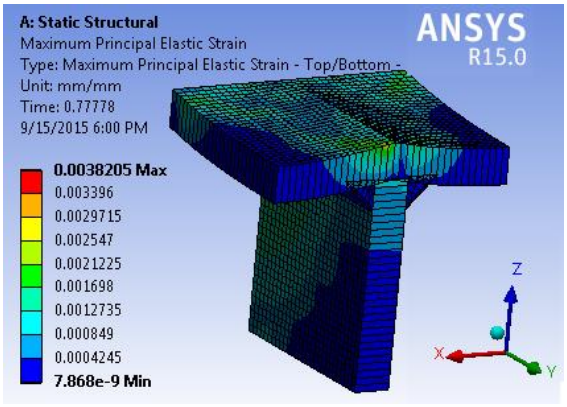

Fig. 4. *Maximum Principal Elastic Strain*

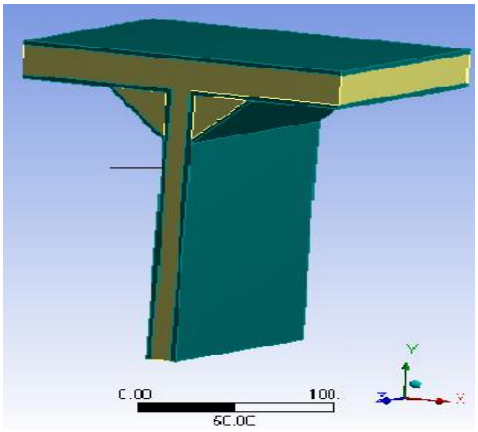

Fig. 5. *The geometry of three layers*

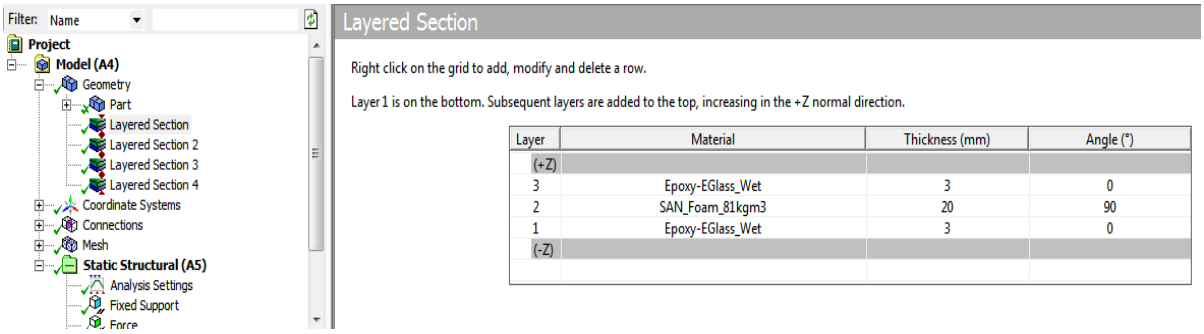

Fig. 6. *The arrangement of layers*

Table 3. *Analysis of several strengths in terms of deflection for honeycomb core*

Honeycomb		
Nr. crt.	**KN**	**Displacement [mm]**
1	2	0.26244
2	4	0.52488
3	6	0.78731
4	8	1.0498
5	10	1.3122
6	12	1.5746
7	14	1.8371
8	15	1.9683
9	16	2.0995
10	17	2.2307
11	18	2.3619
12	19	2.4932
13	20	2.6244
14	21	2.7556
15	22	2.8868
16	23	3.018
17	24	3.1493
18	25	3.2805
19	26	3.4117
20	27	3.5429

Table 4. *Analysis of several strengths of deflection for SANFoam 81*

SanFoam81		
Nr. crt.	**KN**	**Displacement [mm]**
1	2	0.49659
2	4	0.99318
3	6	1.4898
4	8	1.9864
5	10	2.483
6	12	2.9796
7	14	3.4761
8	15	3.7244
9	16	3.9727
10	17	4.221
11	18	4.4693
12	19	4.7176
13	20	4.9659
14	21	5.2142
15	22	5.4625
16	23	5.7108
17	24	5.9591
18	25	6.2074
19	26	6.4557
20	27	6.704

Forty cases were analysed in Ansys Workbench, but these cases were divided for two different cores: honeycomb polypropylene and extruded polystyrene (San Foam 81). Each case has a different force, each starting from 2 kN to 27 kN. The paper dealt with the displacement of the biggest forces application and then a comparison was made between the two cores. In Figures 3 and 4 are shown some images of the forty cases to reveal the total displacement and maximum principal strain. Figure 5 and 6 showed how layers were built to model the structure.

The results of local modelling are presented in more detail, because they can help explain specific phenomena related to the experimental investigation.

In Figure 7 are compared the two cases of important chart displacements to different cores; It should be noticed that the displacement for polypropylene honeycomb was smaller than for San Foam 81.

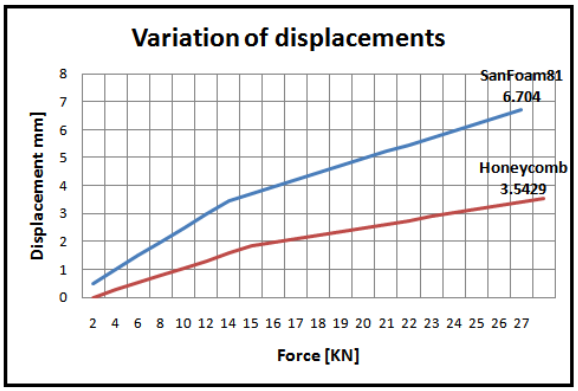

Fig. 7. *Comparing the results of two different cores of joints and blunts*

6. Conclusions

Static analysis was performed to study the response of honeycomb core and expanded polystyrene sandwich for different strengths. Static analysis was performed with the back edge encased T's. Static analysis was performed to check whether the node can support or not some typical naval forces. Based on the results, it is found that the typical naval node with honeycomb core had a smaller displacement than polystyrene. Core figure (Honeycomb) provides better rigidity than the core of extruded polystyrene (foam breast 81). For better results in typical node naval reinforcement core, it is advisable to use all extruded polystyrene (san foam 81) because honeycomb boards cannot be tight, but there should remain a free space when using the foam that will fill the air gap.

Acknowledgement

The work has been funded by the Sectoral Operational Program Human Resources Development 2007-2013 of the Ministry of European Funds through the Financial Agreement POSDRU/159/1.5/S/132397.

References

[1]. Araboui J., Schmitt Y., Pierrot J. L., Royer F. X., *Numerical Simulation and experimental bending behaviour of multi-layer sandwich structures*, Laboratory de Physique des Milieux Denses, France 2014.

[2]. Akour S., Maatah H., *Finite element Analysis of Loading Area Effect on Sandwich Panel Behaviour Beyond theyeld Limit*, Chapter 16.

[3]. Craig A. Steeves, Norman A. Fleck, *Collapse mechanisms of sandwich beams with composite faces and a foam core, loaded in three-point bending. Part II: experimental investigation and numerical modelling*, Cambridge University Engineering Department, 26 November 2003.

[4]. Kantha K. R., Jayathirtha K. R., Sarwade A. G., Chandra S. M., *Strength Analysis on Honeycomb Sandwich Panels of different Materials*, Hyderabad May-Jun 2012.

[5]. ***, *Ansys theory*, http://www.ansys.com/staticassets/ANSYS /staticassets/resourcelibrary/presentation/2014-sd-mechanical-contact-best-practices.pdf.

[6]. ***, http://www.ansys.com/staticassets/ANSYS%20UK/ staticassets/Presentations/2014%20Convergence%20Presentations/ CONF2014_John_Lin_MechanicalContactBestPractices.pdf.

[7]. Huson P. N., *Experimental and numerical simulations of explosive loading on structural components: composite sandwich connections*, UC San Diego, 2012.

[8]. Naresh Ch., *Numerical Investigation into Effect of Cell Shape on the Behavior of Honeycomb Sandwich Panel*, International Journal of Innovative Research in Science, Engineering and TechnologyDecember 2013.

[9]. ANSYS Inc., *ANSYS 12.0 reference manual*, 2009.

[10]. Bianchi G., *Thesis Structural Performance of Spacecraft Honeycomb Panels*, University of Southampton, April 2011.

[11]. Taylor E. M., *Thesis Two-Way Behavior and Fatigue Performance of 3-D GFRP Sandwich Panels*, Faculty of North Carolina State University, 2009.

THE ANNALS OF "DUNAREA DE JOS" UNIVERSITY OF GALATI
FASCICLE IX. METALLURGY AND MATERIALS SCIENCE
Nº. 2 - 2015, ISSN 1453 – 083X

COMPRESSIVE BEHAVIOUR OF ULTRA-SONICATED STARCH / CARBON BLACK / EPOXY COMPOSITES

Iulia Graur[a,b], Georgel Mihu[c], Vasile Bria[a], Adrian Cîrciumaru[a,b*], Iulian-Gabriel Bîrsan[a]

[a]"Dunărea de Jos" University of Galati, Cross Border Faculty of Humanities, Economics and Engineering Sciences
[b] Diagnose and Measurement Group, Galați
[c]"Dunărea de Jos" University of Galati, Engineering Faculty
e-mail: adrian.circiumaru@ugal.ro

ABSTRACT

Fillers are generally used in order to change some basic properties of polymer matrix but the filler particles often tend to aggregate with consequences in terms of the mechanical properties of the final composite. In order to avoid aggregation, many solutions have been proposed and one of them is to use ultra-sounds in various stages of composites formation. In this study, the compressive behaviour of filled epoxy was analysed. As filler, at a 10% volume ratio, a mixture of three parts of starch and one part carbon black was used. The aim of the analysis was to identify the effect of ultra-sonication at different frequencies and for different periods of time on the compressive properties of composites.

KEYWORDS: compressive behaviour, polymer, ultra-sonic treatment, epoxy resin

1. Introduction

Among the thermoset materials, epoxy resins show special chemical characteristics such as: absence of secondary products or volatiles during curing reactions, low shrinkage up on curing, curing over a wide temperature range and the control of degree of cross-linking. Depending on the chemical structure of the curing agents and curing conditions, the properties of cured epoxy resins will vary [1]. Ultra-sonication during polymerization is a very efficient method to increase the dispersion of filler particles in the pre-polymer mixture, in the case of thermoset polymers. The effect of ultra-sonication is also observable through some changes which occur in homogeneity, viscosity, relaxation time and hardening of pre-polymer gels [2]. To get superior properties of a polymer, one usual way is to modify it by placing another phase, for instance a nano-sized one, into the polymer volume [3]. Such materials should provide unique mechanical and thermal properties combined with low specific weight and high wear resistance in order to ensure safety and economic efficiency [4]. Carbon nanotubes, carbon black [5, 6], nano-metals, talc, clays, starch [7, 8] and nano-ceramics are among the most commonly used fillers. Carbon black [9] and starch are used to enhance the properties of epoxy composites compared to the unfilled ones – especially regarding tribological [10] and electrical behaviour [11]. The technique of modifying the polymer by adding certain powders is not new at all but is challenged by some difficulties when the used particles are getting smaller and smaller [12]. The properties of such a modified polymer do not depend only on powders properties, but also on the dispersion of particles into the polymer volume. The main goal is to obtain uniform dispersion avoiding clusters formation as clusters represent structural defects from the polymer network point of view [13]. The use of ultra-sounds, exposure of pre-polymer mixture might solve the uniform distribution problem. Under the action of ultra-sounds there is a change in homogenization, viscosity, relaxation time of pre-polymer mixture and it is noticed a strengthening effect on the formed polymer [14]. Ultra-sound has found numerous uses in widely different fields of application. Recently, attention has turned to multiphase systems where attempts have been made to relate the ultra-sonic velocity with the concentration and the degree of dispersion of two-phase systems [15]. In this paper the effect of ultra-sonication on the compressive properties of carbon black and starch filled epoxy resin composites was

investigated, as starch is meant to avoid the aggregation of carbon-black particles.

2. Experimental method

For this study, compressive tests were performed on modified epoxy composites. The matrix consisted of EPIPHEN RE4020 – DE4020 epoxy system that was modified with a mixture of three parts of starch and one part of carbon black. A composite material is generally composed of two or more materials with distinct properties but through their bond they can provide a single composite material with unique properties [16]. This is true, however, if both constituents are present in a reasonable proportion of at least 5% and various properties [17]. The powder mixture was used to obtain a 10% volume ratio of modifying agent in the epoxy matrix - based on other studies [18]. The powder was mechanically dispersed into the required quantity of resin and the mixture was exposed from one to five minutes to the ultra-sonic flux generated by an air-generator at different frequencies. After this step, the required quantity of hardener was added and the mixture was mechanically mixed at 45 ºC for 15 minutes - in order to maintain the low viscosity of the mixture during the gel phase and afterwards poured into moulds. The 15-minute time of mixing was established after trial and error tests that confirmed the fact that during this step the viscosity of the mixture remained low so that it could be easily poured into the moulds and could allow for the elimination of gaseous products. After this step, all the samples were exposed to ultra-sonic influence at a distance of 1 m from the ultra-sound air-generator. Samples extraction was performed after 24 hours and was followed by a recommended thermal treatment. Compressive tests were carried out at room temperature with M350-5AT testing machine from Testometric (Fig. 1). The compression tests were performed at a speed of 5 mm/min. The compressive specimens were 5 mm in height and 10 mm in diameter. Five specimens of each material were tested. The testing method, the sample dimensions and the test parameters were set according to ASTM-D-3410-87 [19, 20].

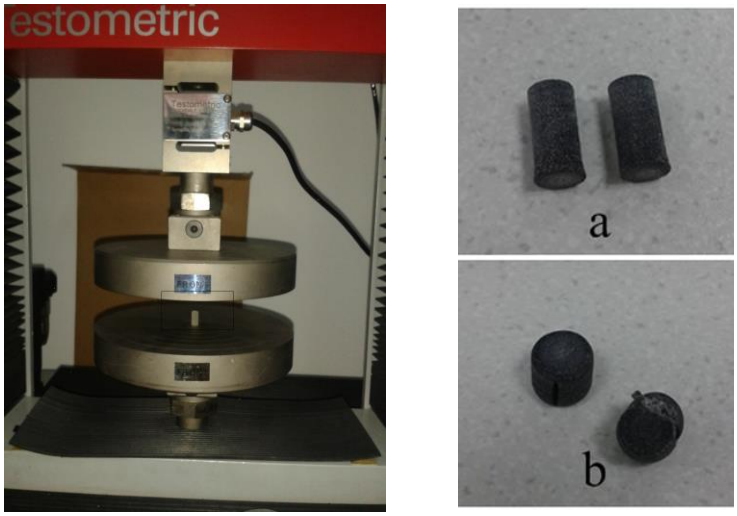

I. II.

Fig. 1. *I - M350-5AT compressive testing machine from Testometric; II - compressive specimens for testing: a) before the compression test; b) after the compression test*

3. Results

The compression Young Modulus and the Strain at Yield of epoxy resin are plotted as a function of ultra-sonic exposure time (0 to 5 minutes).

Regarding the compression Young modulus, it seems (Fig. 2-5) – but this assumption has to be verified – that the exposure at 24 kHz and 42 kHz leads to an improvement in compression elasticity of the polymer – on the x-axis during the epoxy resin ultra-sound exposure. The results are strongly influenced by the local conditions at the time of forming and by ultra-sonication. However, the results in the case of the 26 kHz frequency point out that ultra-sonic exposure has no effect on the compressive elastic modulus, excepting the use of the four-minute ultra-sound exposure whose effect is destructive.

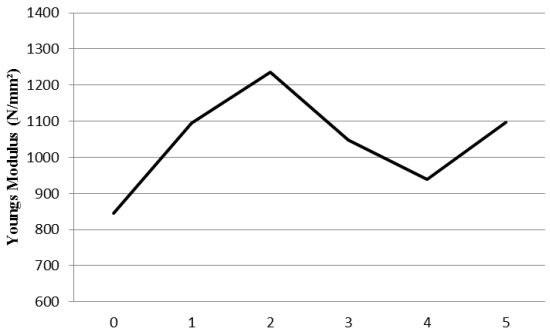

Fig. 2. *Compression Young Modulus of 24 kHz ultra-sonicated epoxy*

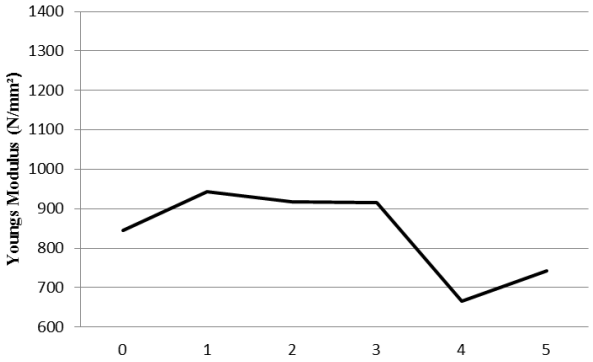

Fig. 3. *Compression Young Modulus of 26 kHz ultra-sonicated epoxy*

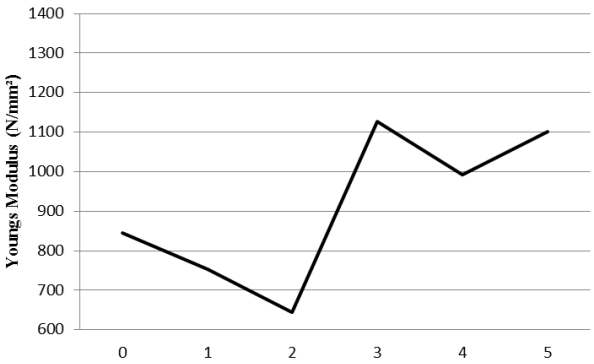

Fig. 4. *Compression Young Modulus of 30 kHz ultra-sonicated epoxy*

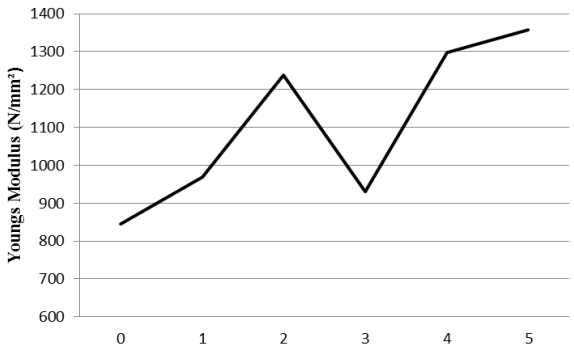

Fig. 5. *Compression Young Modulus of 42 kHz ultra-sonicated epoxy*

At the two higher frequencies, it seems that the ultra-sound exposure time is important since the three-minute ultra-sound exposure time (30 kHz) and, respectively, the two-minute ultra-sound exposure time (42 kHz) lead to better results regarding the materials elasticity.

Marking a change in the polymer mechanical response (from elastic to plastic), the strain at yield is an important parameter used to describe polymers behaviour. The values of this parameter do not show dramatic changes excepting the cases of the one minute ultra-sound exposure time at 30 kHz and the three-minute ultra-sound exposure time at 42 kHz but, once again, these results might be influenced by the environmental conditions.

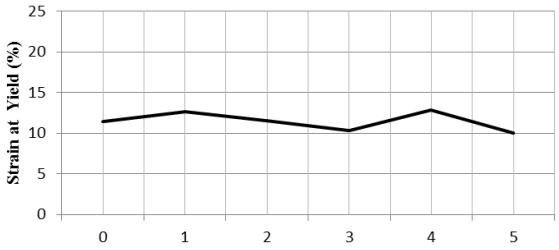

Fig. 6. *Strain at Yield of 24 kHz ultra-sonicated epoxy*

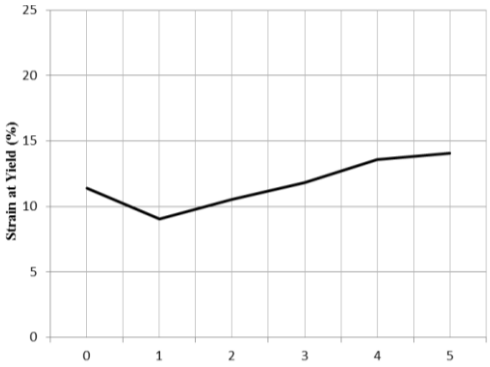

Fig. 7. *Strain at Yield of 26 kHz ultra-sonicated epoxy*

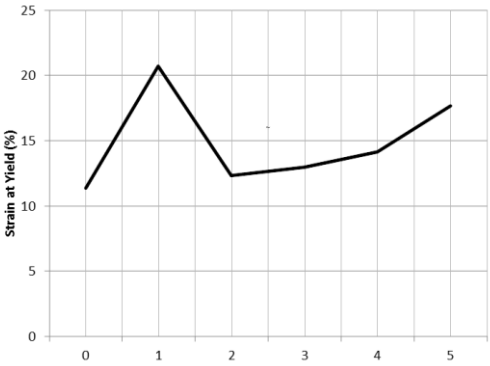

Fig. 8. *Strain at Yield of 30 kHz ultra-sonicated epoxy*

Because of the interaction between ultra-sounds and polymer matrix, it was expected a decrease of compressive parameters values but, analysing the graphs above, the behaviour is far from expectations. The strain at yield (Fig. 6-9) is practically unchanged compared to the standard probe (the sample of epoxy resin without any ultra-sound exposure) taking into account the unavoidable gaseous intrusions inside the samples. The strain at yield is independent both from the ultra-sound frequency and from the ultra-sound energy. It is a fact that the use of ultra-sound exposure leads to better dispersions of powders than the dispersion that had been used to modify the basic properties of the epoxy resin.

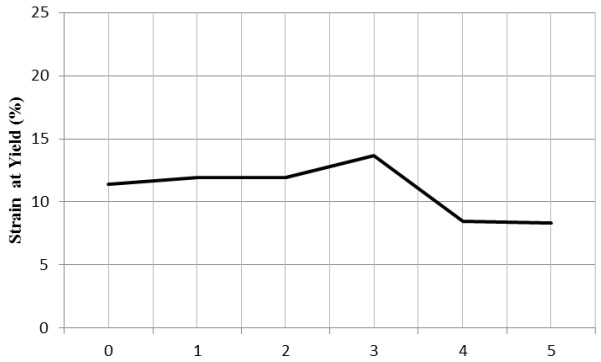

Fig. 9. *Strain at Yield of 42 kHz ultra-sonicated epoxy*

4. Conclusions

These experimental results provided a database on the compressive behaviour of ultra-sonicated starch / carbon black / epoxy composites. A comprehensive and reproducible set of data has been obtained to characterise the mechanical behaviour of the ultra-sonicated starch/carbon black / epoxy composites. These results are particularly significant from the compression point of view, because it seems that ultra-sonication does not induce severe modifications. However tensile and bending tests are necessary in order to complete the picture of the influence of this type of treatment on the mechanical properties of the epoxy resin. One issue that has to be dealt with during further studies is the identification of a method to avoid the gaseous intrusions taking into account the fact that they are responsible for non-linear responses at external loadings.

Acknowledgement

The work of Vasile Bria was supported by Contract nr. 138963/2014, Project code: POSDRU/159/1.5/S/138963.

The work of Georgel Mihu has been funded by the Sectorial Operational Programme Human Resources Development 2007-2013 of the Ministry of European Funds through the Financial Agreement POSDRU/159/1.5/S/132397.

The work of Iulia Graur and Adrian Cîrciumaru had been supported by the Project 12 P01 024 21 (C11) /31.08.2012 (code SMIS 50414).

References

[1]. Asif Abdul Azeez, Kyong Yop Rhee, Soo Jin Park, David Hui, *Epoxy clay nanocomposites – processing, properties and applications: A review*, Composites Part B: Engineering, Vol. 45, Issue 1, 2013.

[2]. Horun S., *Aditivi pentru prelucrarea polimerilor*, Ed.Tehnică, București, 1978.

[3]. Bart J. C. J., *Additives in Polymers.Industrial Analysis and Applications*, John Wiley & Sons, ISBN 0-470-85062-0, 2005.

[4]. Amit C., Muhammad S. I., *Fabrication and characterization of TiO_2 – epoxy nanocomposite*, Materials Science and Engineering A 487, p.574 – 585, 2008.

[5]. Balberg I., *A comprehensive picture of the electrical phenomena in carbon black–polymer composites*, Carbon 40, p. 139 – 143, 2002.

[6]. Gubbels F., Blacher S., Vanlathem E., Jerome R., Deltour R., Brouers F., *Design of Electrical Conductive Composites: Key Role of the Morphology on the Electrical Properties of Carbon Black Filled Polymer Blends*, Macromolecules, 28, p. 1559 – 1566, 1996.

[7]. Vargha Viktoria, Truter Patricia, *Biodegradable polymers by reactive blending trans-esterification of thermoplastic starch with poly(vinyl acetate) and poly(vinyl acetate-co-butyl acrylate)*, European Polymer Journal, 41, p. 715 – 726, 2005.

[8]. Rodriguez-Gonzalez F. J., Ramsay B., Favis B. D., *Rheological and thermal properties of thermoplastic starch with high glycerol content*, Carbohydrate Polymers, 58, p. 139 – 147, 2004.

[9]. Fiedler B., Gojny F. H., Wichmann M. H. G., Nolte M. C. M., Schulte K., *Fundamental Aspects of Nano-Reinforced Composites*, Composites Science and Technology, Vol. 66, Issue 16, p. 3115 – 3125, ISSN 0266-3538, 2006.

[10]. Birsan I. G., Andrei G., Bria V., Postolache I., Circiumaru A., *Tribological Behavior of Clay/Epoxy Composites*, Proceedings of the 5th International Scientific Conference BALTRIB'2009, Kaunas, Lithuania, Vol. 5, p. 164 – 169, ISSN 1822-8801.

[11]. Claudia Ungureanu, Marius Bodor, Iulia Graur, Adrian Cîrciumaru, Vasile Bria, *Carbon filled polymers*, UGAL INVENT, Research and Innovation Exhibition, "Dunarea de Jos" University of Galati, Romania, 7 – 9 October 2015.

[12]. Colbert D. T., *Single-wall nanotubes: a new option for conductive plastics and engineering polymers*, Plastics Additives Compd, p. 18 – 25, 2003.

[13]. Rocco A. M., Pereora R. P., Felisberti M. I., *Polymer*, Vol. 42, p. 199 – 205, 2007.

[14]. Kolosov A. E., Sakharov A. S., Sivetskii V. I., Sidorov D. E., Sokolskii A. L., *Substantiation of the efficiency of using ultrasonic modification as a basis of a production cycle for preparing reinforced objects of epoxy polymer composition*, Chemical and Petroleum Engineering, Vol. 48, Nos. 5 – 6, Sept., 2012 (Russian Original Nos. 5 – 6, May – June, 2012).

[15]. R. Gendron, J. Tatibouet, J. Guevremont, M. M. Dumouliu, L. Piche, *Ultrasonic behavior of polymer blends*, Polymer Engineering and Science, Vol. 35, no. 1, 1995.

[16]. Calienciug A., *Cercetări privind bara parașoc pentru autovehicule, confecționată din materiale compozite noi*, (PhD thesis), 2012.

[17]. Matthews F. L., Rawlings R. D., *Composite Materials: Engineering and Science*, Woodhead Publishing Limited, ISBN 978-1-85573-473-9, 2008.

[18]. Roman I., Ungureanu V., Bria V., Circiumaru A., Birsan I. G., *Strach Epoxy Composites a Study of Starch Amount Influence*, Proceedings of the 12th International Conference on Tribology – SERBIATRIB'11, Kragujevac, Serbia, p. 181 – 184, ISBN 978-86-86663-74-0.

[19]. Cîrciumaru A., *Caracterizarea și testarea materialelor composite cu matrice polimerice*, Ed. Europlus, Galati, 2013.

[20]. Cîrciumaru A., *Caracterizarea și testarea materialelor polimerice*, Ed. Europlus, Galati, 2013.

THE ANNALS OF "DUNAREA DE JOS" UNIVERSITY OF GALATI
FASCICLE IX. METALLURGY AND MATERIALS SCIENCE
Nº. 2 - 2015, ISSN 1453 – 083X

THE UNUSUAL ELECTROMAGNETIC PROPRIETIES OF FABRIC REINFORCED EPOXY COMPOSITES

Marina Bunea[a], V. Bria[b], A. Cîrciumaru[b,*], I. G. Bîrsan[b]
[a] "Dunărea de Jos" University of Galati, Faculty of Mechanical Engineering, 47 Domnească Street, RO-800008, Galati, Romania
[b] "Dunărea de Jos" University of Galati, Border Faculty of Humanities, Economics and Engineering, 47 Domnească Street, RO-800008, Galati, Romania
e-mail: adrian.circiumaru@ugal.ro

ABSTRACT

In this research, the electromagnetic behavior of four composite materials was investigated as an important issue of composite researchers is to control the electrical properties of polymer matrix composites. The four materials are epoxy matrix fabric reinforced composites. Each of the reinforcements is accomplished from 17 layers of fibers fabric of each type, excepting the medial layer which is made of a hybrid fabric meant to solve two issues – the first issue refers to gathering information about the materials loading state while the latter is to increase the electromagnetic shielding properties of the formed materials. The four used fabrics are simple plain fabrics made of yarns of carbon fibers, aramid fibers and, respectively, two types of glass fibers. All the reinforcement layers, excepting the medial one, have the yarns of warp and fill, respectively parallel, while the medial layer has warp yarns perpendicular on the warp yarns of the other layers. The matrix of the wet lay-up technique formed materials is made of epoxy system Epiphen RE 4020 – DE 4020.

KEYWORDS: dielectric permittivity, electrical conductivity, magnetic permeability, epoxy matrix

1. Introduction

The composite materials with unusual electromagnetic properties, which exhibit negative value of electrical and magnetic properties, are of particular interest. The materials with negative values of dielectric permittivity and magnetic permeability are known as meta-materials. Meta-materials which exhibit simultaneously negative dielectric permittivity and negative magnetic permeability are called left-handed materials. They have the negative index of refraction, so that these materials have the similar function of a lens [1-5]. It means that phase and group velocity of an electromagnetic wave can propagate in opposite direction [6, 7], leading to the disappearance of the object in the radar field. When these parameters have different signs, these materials are called right-handed materials [8]. In this case, the electromagnetic wave cannot spread [9].

For a negative ε, the force between two electrons will be attractive, leading to electron-pairing if other electron instabilities can be arrested. Electron-pairing has been demonstrated to be responsible for superconductivity in the conventional low temperature superconductors as well as in the newly discovered high temperature superconductors [10].

In spacecraft construction, meta-materials are important due to their electromagnetic shielding, which can protect the spacecraft against radiation and overheating.

The constitutive elements of a meta-material are meta-atoms or meta-molecules. Among the meta-atoms, we can identify wire meshes, splitter ring resonators, conical Swiss rolls, Swiss rolls, further development of this fascinating domain allowing for other types of constitutive elements [11].

Other structures were also suggested to instigate meta-material behavior, including multi-layers composed of alternately overlapped negative permittivity and negative permeability layers. In the exploration of meta-materials, polymers have been applied only as an insulating host, but the specific contributions of the polymer layer were rarely mentioned, which may be due to the weak electromagnetic responses to outer electric or / and

magnetic field with respect to ferromagnetic materials [4].

Moreover, the composite materials with special electromagnetic properties are studied for the manufacturing of smart composites, whose important characteristic is the auto-repairing of damage area. By measuring the electrical conductivity of the object, it can be determined the mechanical damage area and then a strong electric pulse can be applied for partially melting the polymer matrix in the area of damage, which would eliminate the defect [12, 13]. Carbon fiber reinforced polymer composites are multifunctional materials in which the damage is coupled with the material electrical resistance, providing the possibility of real-time information about the damage state through the monitoring of the resistance [14]. The heterogeneous smart materials might exhibit new properties not existing in any of the constituents due to the coupling of different fields [15].

2. Materials

Four fabric reinforced epoxy matrix composites were formed for this study. They were named HCH – carbon fiber fabric reinforced epoxy composite, HKH aramid fiber fabric reinforced epoxy composite, H1SH and H2SH glass fiber fabric reinforced epoxy composites. The fabrics were simple plain fabrics: 4×4 plain weave carbon fabric with 160 g/m^2 density designated as C, 6.7×6.7 plain weave aramid fabric with 173 g/m^2 density designated as K, 12×12 plain weave glass fabric with 163 g/m^2 density designated as 1S and 6×6 plain weave glass fabric with 390 g/m^2 density designated as 2S. All the materials had 17 of layers reinforcements symmetrically distributed relatively to the medial layer. The medial layer only was made of a special hybrid fabric that had been obtained by replacing each second yarn of aramid fibers in the fill by a mixed carbon-aramid fabric.

The mixed fabric had the structure of 2:1 carbon: aramid yarns on warp and 1:2 carbon: aramid yarns on the fill. Each second yarn of aramid fibers in the fill was manually replaced with a glass fibers yarn of 200 tex in which a tinned cooper wire 0.2 mm diameter was inserted. (Fig. 1).

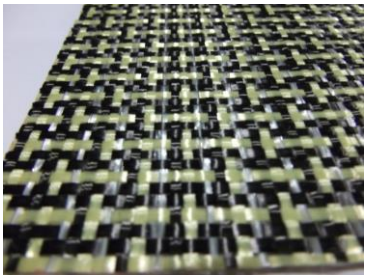

Fig. 1. *The special modified fabric M*

Each material had 16 layers of reinforcement of the same fabric while the medial layer consisted of the above described fabric. For all the 16 identical layers the directions of warp yarns and fill yarns were respectively parallel, while the fill yarns of medial layer were perpendicular on the other layers fill yarns.

The materials were formed using the wet lay-up method placing each pre-polymer imbued sheet of fabric into a glass mold. After polymerization, all the materials were thermally cured according to the epoxy system producer in order to reach the best properties of the polymer.

3. Experimental method

The measurement of electromagnetic parameters of composite materials was performed with a LCR-meter Protek 9216A at five frequencies (100 Hz, 120 Hz, 1 kHz, 10 kHz and 100 kHz) in the four modes that the LCR meter is build: R+Q (resistance and quality factor), L+Q (inductance and quality factor), C+D (capacitance and dielectric loss and C+R (capacitance and resistance). 1V driver voltage was used for measurements. The dimensions of the tested specimens were 281×194 mm. For each sample, five complete sets of measurements were made – with the measuring cell in different points on the surface of the sample – according to the standard electric characterization of plates used in electric and electronic applications.

4. Results and discussion

The evaluations of dielectric permittivity, electrical conductivity and magnetic permeability were made based on the 200 measured values of each C, R and L parameters and were calculated by the formulas given in [16]. In Fig. 2-5 are plotted the values of surface and bulk dielectric permittivity of the composite materials. The higher values of dielectric constants were determined at 100 Hz frequency and then these values were decreased with the increasing of frequency, with the exception of aramid fabric reinforced epoxy composite. As it can be seen in Fig. 3 and 5, the carbon fabric reinforced epoxy composite exhibits negative values of surface and bulk dielectric permittivity in 0.1-10 kHz. The dielectric values were calculated based on the recorded values of the electrical capacitance.

The negative capacitance was observed in solid state device structures and explained by reference to impact ionization, injection of minority carriers, or an imaginary component in the carrier mobility [17]. The dielectric constant of conducting polymer composites becomes negative after the forming of a continuous conducting pathway because of the charge delocalized at a macroscopic scale [6].

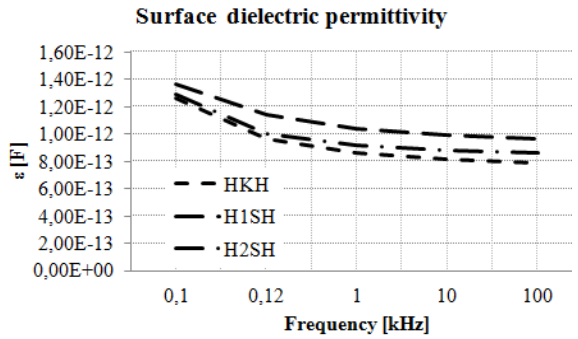

Fig. 2. *The surface dielectric permittivity of the fabric reinforced epoxy composite materials*

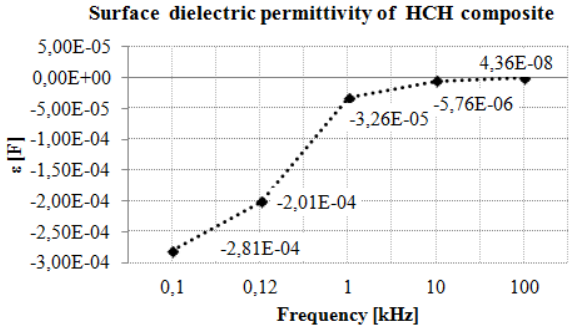

Fig. 3. *The surface dielectric permittivity of carbon fabric reinforced epoxy composite material*

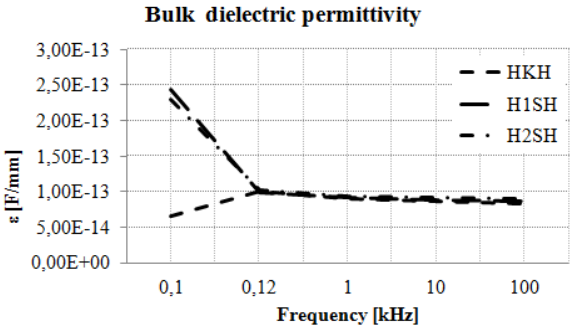

Fig. 4. *The bulk dielectric permittivity of the fabric reinforced epoxy composite materials*

As expected, the carbon fabric reinforced epoxy composite exhibited higher surface electrical conductivity in comparison with other studied composites (Fig. 6). The lower electrical conductivity of aramid and glass fabric reinforced epoxy materials was determined at 0.1 kHz and then the electrical conductivity of these composites decreased with the increasing of frequency, while the electrical conductivity of HCH composite remained unchanged. Similar values of electrical conductivity of the composites were determined for bulk measurements (Fig. 7), with the exception of H1SH composite which exhibited the negative electrical conductivity at 0.1 kHz frequency, but from 0.12 kHz frequency upwards the electrical conductivity of this composite was similar to that of HKH and H2SH composites (Fig. 8).

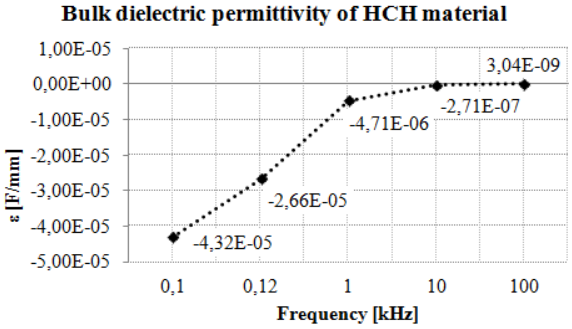

Fig. 5. *The bulk dielectric permittivity of carbon fabric reinforced epoxy composite material*

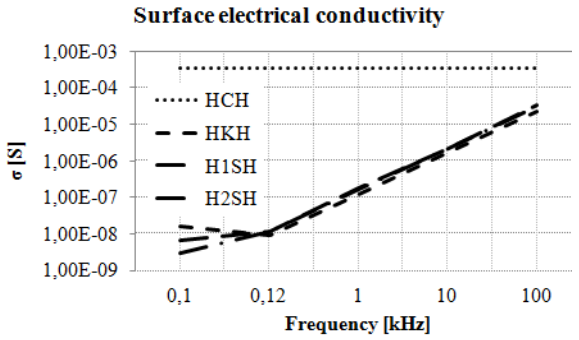

Fig. 6. *The surface electrical conductivity of fabric reinforced epoxy composite materials*

It is possible that negative conductivity appearance occurs in a non-equilibrium electron system, i.e., a situation in which the current flows opposite to the electric field [18]. The values of electrical conductivity of composites were calculated on the recorded electrical resistance by LCR-meter. Negative resistance means that the more positive the voltage is, the more negative the current is, i. e. the current–voltage characteristic is a straight line of negative slope through the origin. Although the negative resistance is apparent, its mechanism resembles that of true negative resistance, i.e. the electrons traveling in the unexpected direction relative to the applied voltage gradient [19].

In Fig. 9-12 are plotted the unusual values of the magnetic permeability of the composites.

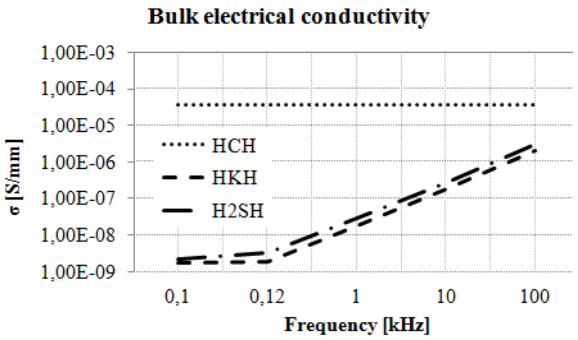

Fig. 7. *The bulk electrical conductivity of fabric reinforced epoxy composite materials*

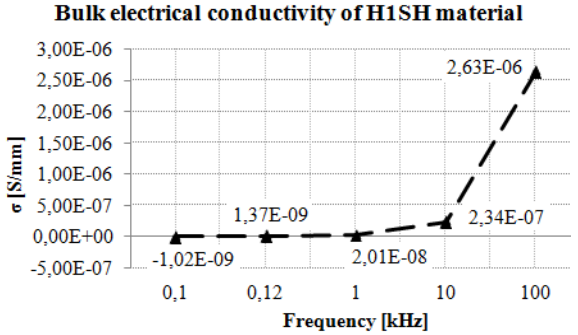

Fig. 8. *The bulk electrical conductivity of 1S glass fabric reinforced epoxy composite material*

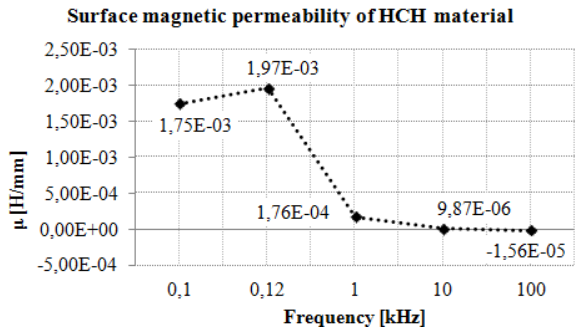

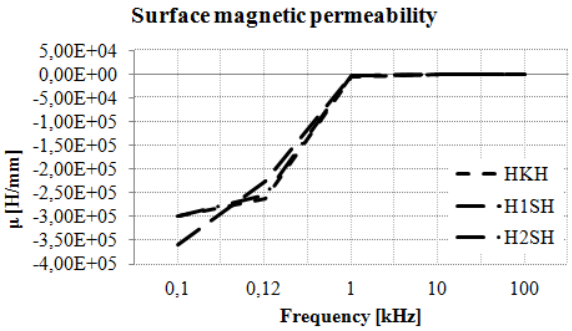

Fig. 9. *The surface magnetic permeability of fabric reinforced epoxy composite materials*

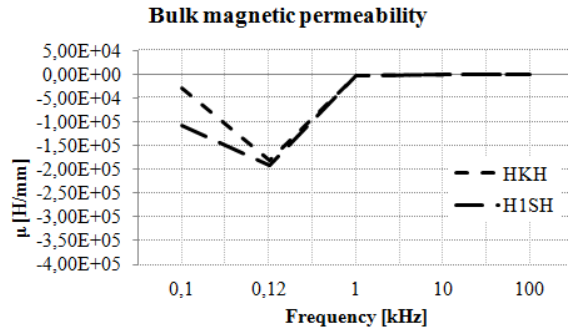

Fig. 10. *The bulk magnetic permeability of fabric reinforced epoxy composite material*

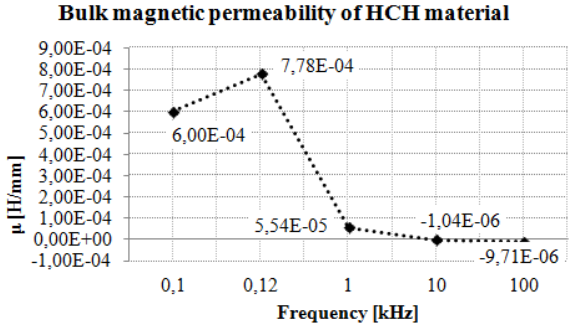

Fig. 11. *The magnetic permeability of carbon fabric reinforced epoxy composite material*

It can be observed that the HKH and H1SH composites exhibit negative values of both surface and bulk magnetic permeability constants at all frequencies in decreasing mode. The composite H2SH exhibits negative magnetic permeability at all frequencies, with the exception of 0.1 kHz where the bulk magnetic constant is positive. Regarding the magnetic behavior of HCH composite, this material exhibits positive values of surface magnetic permeability in 0.1 – 10 kHz frequency range and at 100 kHz the value of the magnetic constant is negative. But the bulk magnetic constants exhibited by HCH composite are positive in 0.1 – 1 kHz frequency range and negative at 10 and 100 kHz frequencies.

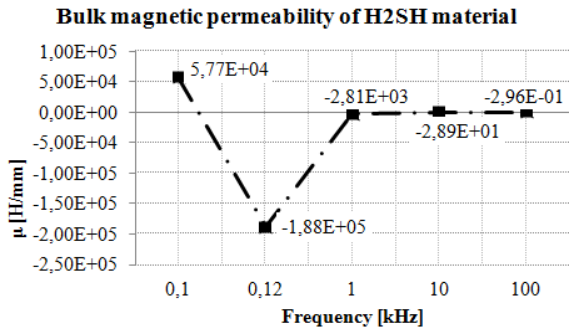

Fig. 12. *The bulk magnetic permeability of 2S glass fabric reinforced epoxy composite materials*

5. Conclusions

The measurements of electrical and magnetic parameters of fabric reinforced epoxy composites were performed. The electric, dielectric and magnetic constants were evaluated and the electromagnetic behaviour of materials was investigated. The conclusions are as follows:

- The carbon fabric reinforced epoxy composite exhibits negative values of dielectric permittivity within 0.1-10 kHz frequency range. The electric conductivity of this material is higher in comparison with other composites and is invariable. It exhibits negative surface magnetic permeability value at 100 kHz and negative bulk magnetic permeability values at 10 and 100 kHz.
- HCH composite exhibits simultaneously negative bulk dielectric permittivity and negative bulk magnetic permeability at the same 10 kHz measurement frequency.
- The magnetic permeability of HKH, H1SH and H2SH composites show negative values on the entire range of frequencies, but only the bulk magnetic constant H2SH of these materials show positive value.
- The bulk electrical conductivity and resistivity of H1SH composite show negative values at 0.1 kHz.

References

[1]. Veselago V. G., *The electrodynamics of substances with simultaneously negative values of ε and μ*, Sov. Phys. Uspekhi, Vol. 10, No. 4, p. 509-514, Jan-Feb. 1966.
[2]. Ramakrishna S. A., *Physics of negative refractive index materials*, IOP Publishing Ltd, Rep. Prog. Phys., 68, p. 449-521, 2005.
[3]. Bayindir M., Aydin K., Ozbay I., Marcos P., Soukoulis C. M., *Transmission properties of composite metamaterials in free space*, Applied Physics Letters, Vol. 81, No. 1, 2002.
[4]. Caglayan H., Ozbay E., *Observation of cavity structures in composite metamaterials*, Journal of Nanophotonics, Vol. 4, 29 July 2010.
[5]. Li M., Yang H., Wen D., *Transmission and reflection of composite metamaterials in free space: experiments and simulations*, Microwave and Optical Technology Letters, Vol. 51, No. 8, August 2009.
[6]. Sui G., Li B., Bratzel Gr., Baker L., Zhong W. H., Yang X. P., *Carbon nanofiber/polyetherimide composite membranes with special dielectric properties*, Soft Matter, 5, p. 3593-3598, 2009.
[7]. Solymar L., Shamonina E., *Waves in Metamaterials*, Oxford University Press, ISBN 978-0-19-921533-1, 2009.
[8]. Si L. M., Jiang T., Chang K., Chen T. Ch., Lv X., Ran L., Xin H., *Active Microwaves Metamaterials Incorporating Ideal Gain Devices*, Materials, 4, p. 73-83, 2011.
[9]. Liu Y., Zhang X., *Metamaterials: a new frontier of science and technology*, Chem. Soc. Rev., 40, p. 2494-2507, 2011.
[10]. Chu C. W., Chen F., Shulman J., Tsui S., Xue Y. Y., Wen W., Sheng P., *A negative dielectric constant in nano-particle materials under an electric field at very low frequencies*, Strongly Correlated Electron Materials: Physics and Nanoengineering, Vol. 5932, 2005.
[11]. Grimberg R., *Electromagnetic metamaterials*, Materials Science and Engineering, B, 178, p. 1285-1295, 2013.
[12]. Makunin A. V., Chechenin N. G., *Nanocarbon-polymer composites for space technologies, Part 1: Synthesis and properties of nano-carbon structures*, "University Book", ISBN 978-5-91304-249-1, 2011.
[13]. ***, *Intelligent air construction materials and microsystem technology*, Moscow Institute of Physics and Technology (State University), Conference Series "The Future of the Industry», Sky Shell, Russia, 2012.
[14]. Wen J., Xia Zh., Choy Fr., *Damage detection of carbon fiber reinforced polymer composites via electrical resistance measurement*, Composites: Part B 42, p. 77-86, 2011.
[15]. Qilin M., Jihui W., Fuling W., Zhixiong H., Xiaolin Y., Tao W., *Conductive Behaviors of Carbon Nanofibers Reinforced Epoxy Composites*, Journal of Wuhan University of Technology-Mater. Sci. Ed., Vol. 23, No.1, p. 139-142, 2008.
[16]. Cîrciumaru A., *Proiectarea, formarea și caracterizarea materialelor compozite cu matrice polimerică*, Editura Europlus, Galați, ISBN 978-606-628-060-0, 2013.
[17]. Bakueva L., Konstantatos G., Musikhin S., Ruda H. E., Shik A., *Negative capacitance in polymer-nanocrystal composites*, Applied Physics Letters, Vol. 85, No. 16, 2004.
[18]. Belonenko M. B., Lebedev N. G., Yanyushkina N. N., Sharkizyanov M. M., *Absolute Negative Conductivity of Graphene with Impurities in Magnetic Field*, Semiconductors, Vol. 45, No. 5, p. 628-632, 2011.
[19]. Wang Sh., Chung D. D. L., *Apparent negative electrical resistance in carbon fiber composites*, Composites: Part B 30, p. 579-590, 1999.

MANUSCRISELE, CĂRŢILE ŞI REVISTELE PENTRU SCHIMB, PRECUM ŞI ORICE CORESPONDENŢE SE VOR TRIMITE PE ADRESA:

MANUSCRIPTS, REVIEWS AND BOOKS FOR EXCHANGE COOPERATION, AS WELL AS ANY CORRESPONDANCE WILL BE MAILED TO:

LES MANUSCRIPTS, LES REVUES ET LES LIVRES POUR L'ECHANGE, TOUT AUSSI QUE LA CORRESPONDANCE SERONT ENVOYES A L'ADRESSE:

MANUSCKRIPTEN, ZIETSCHRITFTEN UND BUCHER FUR AUSTAUCH SOWIE DIE KORRESPONDENZ SID AN FOLGENDE ANSCHRIFT ZU SEDEN:

After the latest evaluation of the journals achieved by National Center for the Science and Scientometry Politics (**CENAPOSS**), as recognition of its quality and impact at national level, the journal is included in B^+ category, 215 code (http://cncsis.gov.ro/userfiles/file/CENAPOSS/Bplus_2011.pdf).

The journal is indexed in:

EBSCO: http://www.ebscohost.com/titleLists/a9h-journals.pdf

Copernicus: http://journals.indexcopernicus.com/karta.php

The papers published in this journal can be visualized on the "Dunarea de Jos" University of Galati site, the Faculty of Engineering, pages: http://www.sim.ugal.ro/Annals.htm, http://www.imsi.ugal.ro/Annals.html.

Publisher's Name and Address:
Contact person: Antoaneta CĂPRARU
Galati University Press - GUP
47 Domneasca St., 800008 - Galati, Romania
Phone: +40 336 130139, Fax: +40 236 461353
Email: gup@ugal.ro

Editor's Name and Address:
Prof. Dr. Eng. Marian BORDEI
Dunarea de Jos University of Galati, Faculty of Engineering

111 Domneasca St., 800201 - Galati, Romania
Phone: +40 336 130208
Phone/Fax: +40 336 130283
Email: mbordei@ugal.ro

AFFILIATED WITH:

- **ROMANIAN SOCIETY FOR METALLURGY**
- **ROMANIAN SOCIETY FOR CHEMISTRY**
- **ROMANIAN SOCIETY FOR BIOMATERIALS**
- **ROMANIAN TECHNICAL FOUNDRY SOCIETY**
- **THE MATERIALS INFORMATION SOCIETY (ASM INTERNATIONAL)**

Edited under the care of
FACULTY OF ENGINEERING

Annual subscription (4 issues per year)

Edited date: 15.06.2015
Issue number: 200
Printed by Galati University Press
accredited CNCSIS
47 Domneasca Street, 800008, Galati
Romania